# Simulation of Controlled Bluff Body Flow with a Viscous Vortex Method

Thesis by

**Doug Shiels**

In Partial Fulfillment of the Requirements

for the Degree of Doctor of Philosophy

California Institute of Technology

Pasadena, California

1998

(Submitted May 15, 1998)

*Dedicated to my parents, Angelo and Beverly,*
*and to my wife, Marnie*

# Acknowledgements

Thanks first and foremost to my research advisor and mentor Prof. Anthony Leonard. Not only did he supply his unique brand of advising rather than supervising which can make all the difference in the world to a fledgling scientist, but he sparked my initial interest in the field of Fluid Mechanics many years ago during his ME19 course. Thanks also to my the rest of my Examining Committee (Prof. Colonius, Prof. Gharib, Prof. Meiron, and Prof. Pullin) for their support as well as to Prof. Roshko for helping to inspire some of the work in this thesis.

There are many collaborators I've been involved with during my thesis work whom I am also indebted to. Thanks to Prof. Petros Koumoutsakos for helping to guide me along in my early years and for all of his encouragement along the way. I've also appreciated formal collaboration with Dr. Alan Stagg, Mohammed Gharib, Dr. Flavio Noca and David Jeon and more informal collaboration with Prof. Gregoire Winckelmans, Mark Brady, Prof. Amy Warncke, Won Bang, and Michael Feger.

Thanks, of course, also, to my many other friends at GALCIT for all their support, who'd I'd attempt to name if not for fear of accidentally leaving some out.

And last, but not least, thanks to my parents Angelo and Beverly for so much that its impossible to put into words and to my wife Marnie for being my light at the end of the tunnel.

# Abstract

Bluff body flows controlled in various manners are simulated with a high-resolution, gridless vortex method. Two-dimensional, unsteady, viscous simulations are utilized to illuminate the physical phenomenon underpinning certain flows of this class. Flows past a rotationally oscillating circular cylinder and flows past an elastically mounted circular cylinder are studied, providing a variety of new insights about these systems. A computational method facilitating long-time, high-resolution vortex simulations is developed whose grid-free nature enables future extension to complex geometries.

The significant fluid forces experienced by bluff bodies are of much practical concern and are induced by flowfields that are often complex. The studies in this thesis aim to contribute to the understanding of the relation between wake development and forces and how to exploit this relationship to achieve flow control. A circular cylinder undergoing rotational oscillation is known to experience a significant deviation in forces from unforced flow. Computations from Re=150-15000 verify past experimental observation of significant drag reduction for certain forcing parameters. These simulations also illuminate the mechanism which renders this control effective - a forced boundary layer instability triggering premature shedding of multipole vortex structures.

New insights were also provided by studies of flow over a model of an elastically mounted cylinder. A two-dimensional cylinder modeled as a damped oscillator can serve as an approximation to three-dimensional situations such as a cable under tension. Simulations clarified the behavior of such a two-dimensional system and, contrary to a line of classical thinking, revealed an unexpected adaptivity in wake evolution. New scaling is also suggested which better classifies these systems under certain conditions.

Vortex methods are well-suited for incompressible bluff body flow in many ways. However, the handling of viscous diffusion causes complications for such simulations. A relatively unexplored approach, the core expansion method, is studied, extended, and implemented in this work in order to balance accuracy with preservation of the gridless foundation of vortex methods. This viscous technique is found to enable long-time calculations that are prohibitive with other techniques while preserving a high level of accuracy.

# Table of Contents

# List of Figures

# List of Tables

# 1 Introduction

A body is considered bluff when the flow over it will experience large-scale separation under typical circumstances. It stands in opposition to a streamlined body, with the classification obviously based on the orientation of the body within a flow as well as the body's geometry (e.g., an airfoil is streamlined at low angles of attack but bluff otherwise). Large-scale separation results in typically larger forces on the body than are characteristic of a streamlined flow, as well as a great deal of unsteadiness. These features of bluff body flow have significant ramifications for practical systems ranging from offshore platforms to industrial cables (e.g., suspension bridges, power lines). The complexity of separated flow, though, makes these systems resistant to analysis and necessitates the use of experiment or simulation to further understanding of the phenomena bluff bodies experience.

Vortex methods are a distinct alternative to established computational techniques (e.g., finite difference, spectral element) for incompressible flow over bluff bodies. They are founded upon the simplicity of a vorticity description for inviscid, incompressible flow. The simulation of such flow reduces to tracking the convection of packets of vorticity. For this reason, vortex methods can be implemented grid-free and thus hold much promise as a technique which is easily adaptable to flow over general (and even time-dependent) bodies. Furthermore, the vorticity field is often quite compact compared to the domain that must be simulated for accurate computations based on primitive variables. In addition, vortex methods exactly satisfy the boundary conditions for external flows (i.e., those with internal boundaries only; unbounded at infinity), removing an issue that is a source of much consternation for grid-based techniques. Fine reviews of inviscid vortex methods are available for both two-dimensional (Leonard [1980], Sarpkaya [1989], Spalart [1988]) and three-dimensional (Leonard [1985]) flow. The foundations of two-dimensional vortex methods are also sketched in Chapter 2 of this work.

Studies in this thesis are limited to two-dimensional flows as high-resolution vortex methods are in a state of relative infancy in their development. Complications exist in the three-dimensional vortex method formulation that hinder techniques which

are well-suited to two-dimensional formulations. As accurate studies of bluff body flow including time-dependent forces are desired, high-resolution is necessary.

Much of the historical work on vortex methods strives to develop so-called 'modeling' techniques in which accuracy at finer scales is sacrificed in order to achieve stable, extremely fast, computational methods. As a result, vortex methods have come to be identified as the 'back-of-the-envelope' version of computational techniques. Although vortex methods are well-suited for this niche, more recently attention in the vortex methods community has shifted to development of high-resolution techniques. To fully resolve bluff body flows, however, vortex methods must be modified to properly account for viscous effects and thus be able to accurately simulate unsteady boundary layers.

Prior to the past decade, viscous effects were generally added to vortex methods using the random walk technique proposed by Chorin [1973]. From a practical standpoint, random walk is a low-resolution approach that is computationally efficient and thus a good complement to classical vortex methods. However, there has been a good deal of investigation over the past decade into alternative means of adding viscous effects to facilitate the development of high-resolution vortex methods. This has proven a difficult endeavor as the particle representation of vorticity in vortex methods is Lagrangian in nature and yet the viscous effects come more simply from Eulerian aspects of the formulation. Efforts in this area are reviewed in Chapter 2. Viscous techniques were discovered which yielded high-resolution but introduced the use of grids into otherwise grid-free vortex methods in order to achieve accuracy. One of these, the particle strength exchange technique, is the basis for a method extensively developed at Caltech (Winckelmans [1989], Pepin [1990], Koumoutsakos [1993]) which is used for many simulations in this thesis and is reviewed in Chapter 2.

More recently, work has begun on viscous vortex methods which achieve a high level of accuracy, yet preserve the desired grid-free feature. This is again an area of study in its infancy and, as discussed in Chapter 2, none of the techniques are clearly suitable at this point in their development. One such approach is based upon the core expansion technique for diffusion. This method was proposed relatively long ago (Leonard [1980]) but its development stalled due to mathematical objections (Greengard

[1985]). Recent work by Rossi [1996][1997] alleviated these objections. The core expansion approach requires a localized re-gridding of the field by splitting and merging neighboring computational particles. There is a good deal of focus in Chapter 2 on the determination of how to accurately extend the core expansion concept into a practical implementation, dealing with issues such as: proper constraints for the splitting and merging of particles, adaptations to accurately include a viscous boundary, and necessary levels of resolution.

Two primary studies of flow over a circular cylinder are presented in Chapter 3 and Chapter 4 of this thesis. The first concerns a cylinder in a freestream free to respond to lift forces under the constraint of a damped elastic support but held rigid in the flow direction. Such a system is a basic, two-dimensional model of the behavior of a three-dimensional flexible structure such as a cable under tension. As there is much practical interest in predicting the response of such structures, this flow has been extensively studied in an attempt to define the fundamental behavior of the system. However, models for the response have proven elusive as many parameters impact the response and complex phenomena are observed. Motivated by a recent experimental study (Gharib et al. [1997]) suggesting that the complete response characteristics of the system are not properly accounted for by the widely-accepted lock-in behavior, computations are presented in Chapter 3 exploring limiting configurations of the system that are difficult to study experimentally. The results of these computations suggest a new view of the behavior of the elastically supported cylinder. The complex issue of synchronization between the wake and mechanical system appears to define response rather than simply a lock-in to the natural mechanical frequency.

In Chapter 4, a more active means of flow control is explored. Many mechanisms have been studied to alter bluff body flows in order to achieve a desired response. The goals of flow control can be enhanced mixing or improved lift-to-drag ratio but typically focus on minimizing the large, unsteady forces impinging on a body. Thorough reviews that outline the routes to such flow control have been given by Zradkovich [1981] and Gad-el-Hak et al. [1991]. In general, these methods involve adding extra structures such as a shroud to redirect flow or localized control over the boundary layer such as

suction/blowing at the surface. Although highly effective for many applications, they can be unsuitable in some situations.

A potentially simpler route to drag reduction was observed in experiments by Tokumaru et al. [1991] to be the rotary oscillation of a circular cylinder. As discussed in Chapter 4, his findings reveal peculiar qualitative behavior. Simulations are undertaken at Reynolds numbers up to 15000 in Chapter 4 in an attempt to verify and better understand Tokumaru's observations. Computation at Re=15000 proves very challenging and necessitated use of the core expansion technique developed in Chapter 2. The results, though, make a strong case that an intriguing boundary layer instability, which is generated by the rotary oscillation, forces a delay of separation. The separation delay results in a significant drag reduction which can prove quite efficient from a power savings perspective.

# 2 Vortex Methods

## 2.1 Inviscid Foundation

### 2.1.1 Evolution Equation

Consider fluid flows in which density is a constant (i.e., incompressible) and there is no variation in at least one of the three Cartesian spatial dimensions (i.e., two-dimensional flow). The fluid is also required to be single-phase, homogeneous, and marked by a high heat capacity such that for all flows considered temperature variation has a negligible impact on the flowfield. The evolution of such a fluid is governed by the following relations for conservation of mass and momentum respectively.

$$\nabla \cdot \underline{u} = 0 \tag{2.1}$$

$$\frac{\partial \underline{u}}{\partial t} + (\underline{u} \cdot \nabla)\underline{u} = -\frac{1}{\rho}\nabla p + \nu \nabla^2 \underline{u} + \underline{f} - \underline{a}_{rel} \tag{2.2}$$

where: $\underline{u}$ = velocity, $p$ = pressure, $\rho$ = density, $\nu$ = viscosity,
$\underline{f}$ = body force, $\underline{a}_{rel}$ = reference frame acceleration

In this formulation, it is necessary to solve for both the pressure and two velocity components in order to evolve such a flow, which can complicate computational approaches. Thus, consider instead the evolution equation for the curl of the velocity field, known as the vorticity,

$$\underline{\omega} = \nabla \times \underline{u}$$

For two-dimensional flow, the vorticity vector has only one component and thus can be expressed as a scalar field $\omega(x,y)$ such that

$$\omega \hat{z} = \nabla \times \underline{u} \qquad \underline{u} = u\hat{x} + v\hat{y} + 0\hat{z}$$

Taking the curl of (2.2) and applying (2.1) and the two-dimensionality constraint yields

$$\frac{\partial \omega}{\partial t} + (\underline{u} \cdot \nabla)\omega = \nu \nabla^2 \omega + \nabla \times (\underline{f} - \underline{a}_{rel}) \tag{2.3}$$

Note that (2.3) is simply the evolution of the scalar vorticity field rather than the three variables involved in the primitive variable formulation. As is seen below, the vector velocity field can be explicitly extracted from knowledge of the vorticity field.

### 2.1.2 Vorticity Inversion Formula

In order to determine a flow from the vorticity equation, (2.3), it is necessary to find a velocity field in terms of the vorticity field. To do so, consider decomposing the velocity vector into two fields

$$\underline{u} = \nabla \times \underline{\psi} + \nabla\phi \tag{2.4}$$

where $\underline{\psi}$ is the vector streamfunction and $\phi$ is the velocity potential. Now consider the curl of (2.4).

$$\underline{\omega} = \nabla \times \nabla\phi + \nabla \times \nabla \times \underline{\psi} = -\nabla^2 \underline{\psi} + \nabla(\nabla \cdot \underline{\psi}) \tag{2.5}$$

Note that the velocity potential serves to include components of the velocity field which cannot be represented in the vorticity field. For two-dimensional flow, (2.5) simplifies to

$$\omega = -\nabla^2 \psi \tag{2.6}$$

The Green's function for the two-dimensional Laplacian can now be convolved with the streamfunction to give a vorticity-based representation of the streamfunction.

$$\psi(\underline{x}) = -\tfrac{1}{2\pi} \iint \ln|\underline{x} - \underline{x}'|\omega(\underline{x}')d\underline{x}' \tag{2.7}$$

Now (2.7) can be used in (2.4) to yield the relation commonly known as the Biot Savart law

$$\underline{u}(\underline{x}) = -\tfrac{1}{2\pi} \iint \frac{(\underline{x} - \underline{x}') \times \omega(\underline{x}')\hat{z}}{|\underline{x} - \underline{x}'|^2} d\underline{x}' \quad + \quad \nabla\phi \tag{2.8}$$

The foundation of vortex methods rests on use of (2.3) and (2.8) to track a fluid flow based on the evolution of its vorticity field.

Vortex methods take advantage of the fact that in Lagrangian form,

$$\frac{D\omega}{Dt} = \nu\nabla^2\omega + \nabla \times (\underline{f} - \underline{a}_{rel}), \tag{2.9}$$

the vorticity equation is free of the computational instabilities associated with the convective term. In the inviscid case without body forces and frame of reference acceleration,

$$\frac{D\omega}{Dt} = 0, \tag{2.10}$$

the evolution equation is dramatically simplified, making possible the use of a 'gridless' approach only requiring the tracking of vorticity with (2.8). From these fundamental techniques, modifications can be added to model viscous and three-dimensional effects, and the former will be explored in some detail further below. Only irrotational body forces and frame of reference accelerations are considered in this thesis.

The above discussion has assumed the fluid is unbounded. The means of integrating an internal boundary is dealt with in section 2.1.5.

### 2.1.3 Lagrangian Discretization

Computational simulation requires the discretization in space and time of (2.3) and (2.8). At this point, consider only the issue of spatial discretization. Vortex methods utilize a particle discretization of (2.10), namely points which convect with the flow and carry information about the vorticity field,

$$\omega(\underline{x},t) = \sum_{i=1}^{N} \Gamma_i(t)\eta(|\underline{x}-\underline{x}_i|,t)\,, \tag{2.11}$$

rather than tracking the vorticity field at sampled grid points. Although non-axisymmetric choices for $\eta$ are possible, they are generally avoided as they complicate discretization of (2.8). The 'amount' of vorticity carried by a given particle, known as its circulation, is represented by $\Gamma$ and the spatial distribution assumed for this circulation is given by $\eta$. The core distribution $\eta$ is normalized

$$\iint \eta(\underline{x})d\underline{x} = 1 \tag{2.12}$$

so that (2.11) gives

$$\sum_{i=1}^{N} \Gamma_i = \iint \omega d\underline{x} \tag{2.13}$$

Using (2.11) in conjunction with (2.10) and (2.8), particle centers $\underline{x}_i$ are convected with fluid velocity $\underline{u}(\underline{x}_i)$, assuming the particle to be a solid body of fixed geometry (i.e., $\eta(|\underline{x}-\underline{x}_i|,t) = \eta(|\underline{x}-\underline{x}_i|)$ ). Particle strengths $\Gamma_i$ remain constant in an attempt to satisfy (2.10). In other words,

$$\frac{d\underline{x}_i}{dt} = \underline{u}(\underline{x}_i) \tag{2.14}$$

$$\frac{d\Gamma_i}{dt} = 0 \tag{2.15}$$

Although the discretization (2.11) permits (2.8) to be integrated exactly, error is created due to the assumption that the particles convect as solid bodies. The error induced is dependent on the choice of distribution function $\eta$ and identified in Leonard [1980].

The simplest choice for $\eta$ is a delta function, which also alleviates the convection error discussed above due to its pointwise nature.

$$\omega_\delta(\underline{x},t) = \sum_{i=1}^{N} \Gamma_i(t)\delta(|\underline{x} - \underline{x}_i|) \tag{2.16}$$

This is referred to as a 'point vortex representation'. Of course, the use of a delta function introduces difficulty with singularities in the field, thus providing a poor representation of continuous vorticity fields. However, it can be used effectively where low resolution is tolerable. In fact, it has been shown that the point vortex method converges to solutions of the Euler equations in Goodman et al. [1990] and Hou et al. [1990].

Various choices for $\eta$ for both 2D and 3D vortex methods are reviewed by Winckelmans et al. [1993]. The procedure for discretizing (2.8) involves discretizing (2.7) and subsequently applying (2.4). Consider the kernel in (2.7)

$$K_\psi(\underline{x}', \underline{x}) = -\tfrac{1}{2\pi}\ln|\underline{x} - \underline{x}'| \tag{2.17}$$

If one chooses point vortices (2.16) for discretization, (2.7) yields

$$\psi_\delta(\underline{x}) = K_\psi * \omega_\delta = -\tfrac{1}{2\pi}\sum_{i=1}^{N} \Gamma_i \ln|\underline{x} - \underline{x}_i| \tag{2.18}$$

where (*) refers to a convolution. For other choices of $\eta$, construct instead a regularized kernel

$$K_{\psi\eta} = K_\psi * \eta \tag{2.19}$$

so that

$$\psi = K_\psi * \omega = K_\psi * \eta * \omega_\delta = K_{\psi\eta} * \omega_\delta \tag{2.20}$$

which can be easily discretized as in (2.18) as long as (2.19) can be represented analytically.

In this thesis, a Gaussian distribution for the vortex particle

$$\eta(\underline{x}) = \frac{1}{2\pi\sigma^2} e^{-\frac{|\underline{x}|^2}{2\sigma^2}} \tag{2.21}$$

is used exclusively. The parameter $\sigma$ provides control over the size of a vortex particle. Winckelmans [private communication] found the Gaussian distribution to perform more robustly than others considered in Winckelmans et al. [1993]. Using the Gaussian for $\eta$ results in

$$K_{\psi\eta}(\underline{x}', \underline{x}) = -\frac{1}{4\pi\sigma}\left(\ln\left(\frac{|\underline{x}-\underline{x}'|^2}{2\sigma^2}\right) + E_1\left(\frac{|\underline{x}-\underline{x}'|^2}{2\sigma^2}\right)\right) \tag{2.22}$$

where $E_1$ is an exponential integral (cf. Bender, et al. [1978]). A discretization for the velocity field based on a vorticity field represented by particles of Gaussian distribution is thus given by

$$\underline{u}(\underline{x}) = \frac{1}{2\pi}\sum_{i=1}^{N} \Gamma_i \frac{((\underline{x}_i - \underline{x}) \times \hat{z})(1 - e^{-\frac{|\underline{x}-\underline{x}'|^2}{2\sigma^2}})}{|\underline{x} - \underline{x}_i|^2} \tag{2.23}$$

which can be seen to converge to the point vortex representation far from the particle centers.

The accuracy with which a continuous vorticity field is captured by (2.11) and (2.21) depends on the inter-particle spacing and its relation to the core size $\sigma$. It was shown in Beale et al. [1985] that the error in this discretization of the vorticity field is $O((\frac{h}{\sigma})^2)$ where h is the spacing between particle centers.

### 2.1.4 Fast Methods

One quality which distinguishes vortex methods from grid-based techniques is the requirement to integrate over the entire vorticity field in (2.8). As a result, each timestep of the vortex method outlined above would incur a heavy computational cost of $O(N^2)$ to advance N computational particles in accordance with (2.23). However, noting from (2.8) that the velocity induced by a vortex element drops off as the inverse of distance in the far field motivates methods to approximate (2.8) by grouping the influence of distant vortex elements to reduce computational cost to O(N). These approximations are crucial in making vortex method computations of challenging problems practically feasible.

An approach by Barnes et al. [1986] reduces the computational cost of a vortex method to $O(N\log_2 N)$ by grouping the influence of distant computational elements and utilizing a Laurent expansion in (2.23). In this analysis the point vortex representation is assumed for the core distribution $\eta$. This is a reasonable assumption since the effects of core distribution become negligible for distant elements. Consider a complex variable representation of (2.23) for a group of point vortices given by

$$V(z) = \frac{i}{2\pi}\sum_{n=1}^{M}\frac{\Gamma_n}{z - z_n} \tag{2.24}$$

Introduce a new location $z_m$ that will serve as a point about which to expand the influence of groups of far field particles

$$V(z) = \frac{i}{2\pi}\frac{1}{z - z_m}\sum_{n=1}^{M}\frac{\Gamma_n}{1+\frac{z_m - z_n}{z - z_m}} = \frac{i}{2\pi}\frac{1}{z - z_m}\sum_{k=0}^{P}\frac{\alpha_k}{(z - z_m)^k} + O\left(\left|\frac{z_m - z_n}{z - z_m}\right|^{P+1}\right) \tag{2.25}$$

$$\text{where} \quad \alpha_k = \sum_{n=1}^{M}\Gamma_n (z_m - z_n)^k$$

The summation over M particles can thus be reduced to a summation over P+1 terms involving coefficients $\alpha_k$ that can be precomputed and reused for each summation over the group of particles. The error term defines the need for the particle group to reside in the far field of the point z.

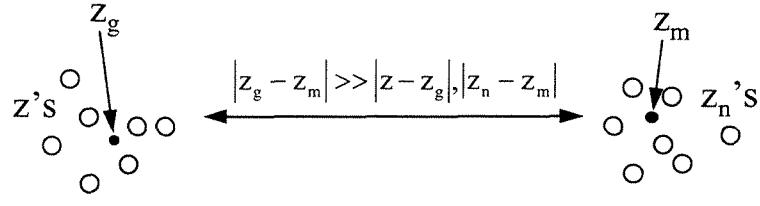


**Figure 1: Schematic for fast summation methods.**

The summation can be further accelerated to O(N) following an approach by Greengard et al. [1987]. The Barnes approach can be termed 'particle-box' as it dictates how to have a single vortex element interact with a group (or box) of far field particles. The O(N) approach instead defines how groups of far field particles can efficiently interact with each other, termed 'box-box', using a Taylor expansion.

Consider introducing a new point $z_g$ to (2.25) which lies close to the point z but is in the far field of $z_m$. This point will serve as the center of the Taylor expansion.

$$\sum_{k=0}^{P}\frac{\alpha_k}{(z-z_m)^{k+1}}=\sum_{k=0}^{P}\frac{\alpha_k}{(z_g-z_m)^{k+1}\left(1+\frac{z-z_g}{z_g-z_m}\right)^{k+1}}$$

$$=\sum_{k=0}^{P}\frac{\alpha_k}{(z_g-z_m)^{k+1}}\left[\sum_{h=0}^{Q}(-1)^h\binom{h+k}{k}\left(\frac{z-z_g}{z_g-z_m}\right)^h\right]+O\left(\left|\frac{z-z_g}{z_g-z_m}\right|^{Q+1}\right)$$

$$=\sum_{h=0}^{Q}\left(\frac{z-z_g}{z_g-z_m}\right)^h\left[\sum_{k=0}^{Q}\binom{h+k}{k}\frac{\alpha_k}{(z_g-z_m)^{k+1}}\right]+O\left(\left|\frac{z-z_g}{z_g-z_m}\right|^{Q+1}\right) \qquad (2.26)$$

Coefficients of this expansion can now be precomputed as well, though unlike the $\alpha_k$, this will require a determination of which groups will interact.

$$V(z)=\frac{i}{2\pi}\sum_{h=0}^{Q}\delta_h(z-z_g)^h+O\left(\left|\frac{z-z_g}{z_g-z_m}\right|^{Q+1}\right)+O\left(\left|\frac{z_m-z_n}{z-z_m}\right|^{P+1}\right) \qquad (2.27)$$

$$\delta_h=\frac{1}{(z_m-z_g)^h}\sum_{k=0}^{P}\binom{h+k}{k}\frac{\alpha_k}{(z_g-z_m)^{k+1}}$$

Thus velocities are computed at the points $z_g$ with (2.25) and then transferred to the particle locations themselves with (2.27).

An entire hierarchy of groupings may be developed with a quad-tree structure to allow for maximal use of the above approximations. An example is provided in Figure 2. Any particle within the shaded box z could interact with all particles in a box A as a single group, utilizing (2.25) with the $z_n$ being all the particles in box A. Similarly, groups can be formed within the boxes B. Particles in the unlabeled adjacent boxes are too close to points in the shaded box to use the fast approximations and must interact via (2.23). Such a hierarchy can be extended for as many levels as desired and similarly govern the application of (2.27).

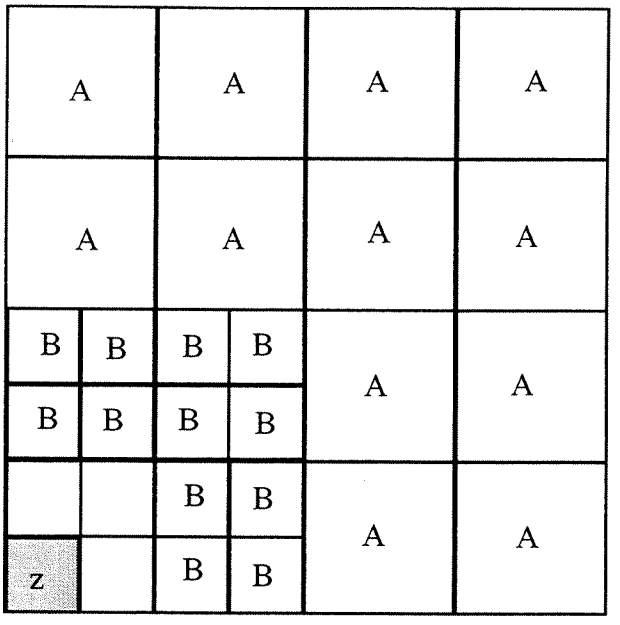


**Figure 2: Hierarchy of interaction levels.**

### 2.1.5 Boundary Conditions

The vortex method described above accommodates an unbounded fluid whose velocity drops off to zero in the infinite far field. Other boundary conditions can be satisfied by a vortex method if they can be included utilizing either the velocity potential $\phi$ in (2.4), a fixed distribution of vorticity to directly modify the vorticity field, or a source of generation of vorticity. For example, to simulate a freestream (u=k, v=0, k=constant) the potential $\phi(x,y)=kx$ can be used.

The boundary conditions dealt with in this work are a freestream and a surface on which the velocity is defined (e.g., a solid body). Of course, a tangential velocity boundary condition cannot be supported in an inviscid flow, but it is discussed here for completeness. A common approach in vortex methods is to utilize velocity potential sources and a vortex sheet along the bounding surface to satisfy the normal and tangential boundary conditions simultaneously. Continuous adjustment to the strength of these elements (which varies along the surface as well) in response to the evolution of the vorticity field satisfies the boundary condition. Thus, the new expression for the velocity field including velocity source strength $\kappa$ and vortex sheet strength $\gamma$ becomes

$$\underline{u}(\underline{x}) = -\frac{1}{2\pi}\iint \frac{(\underline{x}-\underline{x}')\times\underline{\omega}(\underline{x}')}{|\underline{x}-\underline{x}'|^2}d\underline{x}' \quad + \quad \nabla\phi$$
$$+ \quad \frac{1}{2\pi}\nabla\oint\kappa(s)\ln(r)ds \quad - \quad \frac{1}{2\pi}\nabla\times\oint\gamma(s)\ln(r)\hat{z}ds \tag{2.28}$$

where (2.28) replaces (2.8). For general boundaries, closed form solutions are not available for $\kappa$ and $\gamma$ and thus the boundary condition can only be satisfied at instances in time where (2.28) can be solved (for $\kappa$ and $\gamma$) with a panel method. In a panel method, an integral is numerically approximated as a discrete summation with an unknown weight for each variable in the summation. A system of equations can thus be established whose solution gives a discrete representation of the unknown function in the integrand. If it is only necessary to satisfy the inviscid, solid body constraint of zero normal velocity, image vortices can be used instead. However, image vortices are difficult to use with complex geometries and add a heavy load to the computational cost by doubling the number of vortex elements.

The solution to (2.28) is not unique and, in fact, a class of external flows with both a tangential and normal velocity boundary condition can be satisfied using $\kappa$=0, simplifying the solution process. It is shown in Spalart [1982] and Koumoutsakos [1993] for two-dimensional boundaries and Leonard [1994] for three-dimensional boundaries that adherence to the tangential velocity condition for an interior boundary (i.e., one which is enclosed by the fluid domain) implies that the normal velocity condition is also satisfied for bodies whose flow representation is irrotational. An important boundary of this type is a solid body (no-slip, no through-flow) in irrotational motion. This relation (though not the proof of it) has met with skepticism in the vortex methods community and thus is sketched below.

Consider a surface S bounding an area V, which represents a body whose velocity is given by $\underline{u}_V$. In a vortex method simulation, the body is treated as a region of fluid. Thus consider the streamfunction within the body

$$\psi = \frac{1}{2}\underline{u}_V \times \underline{x} + \psi' \tag{2.29}$$

yielding

$$\underline{u} = \nabla\times\psi = \underline{u}_V + \nabla\times\psi' \tag{2.30}$$

for the velocity within the body. It is desired to show that if the no-slip condition is satisfied

$$\underline{u}\cdot\hat{t} = \underline{u}_V\cdot\hat{t}, \tag{2.31}$$

then the normal velocity condition will be satisfied. This will follow if it can be shown that $\psi'$=constant so that $\underline{u}=\underline{u}_V$. Consider Green's identity

$$\iint_V\left[(\nabla a)\cdot(\nabla b)+a\nabla^2 b\right]dV+\oint_S a\frac{\partial b}{\partial n}ds=0 \tag{2.32}$$

Since there is no vorticity in the body and assuming the body can be represented by an irrotational flow,

$$\omega=-\nabla^2\psi=-\nabla^2\psi'=0 \tag{2.33}$$

and, based on (2.31)

$$(\nabla\times\psi')\cdot\hat{t}=\frac{\partial\psi'}{\partial n}=0 \tag{2.34}$$

Substituting into (2.32) with $a=b=\psi'$

$$\iint_V|\nabla\psi'|^2dV=0 \tag{2.35}$$

which thus implies $\psi'=0$.

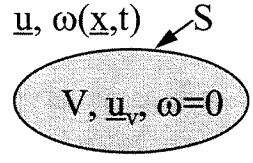


**Figure 3: Layout for the linked boundary conditions proof.**

Thus, for such a boundary, the vortex sheet is the only element necessary to satisfy both boundary conditions. Also, even if the body has a rotational component, this efficient procedure can still be utilized in certain instances by decomposing the flow into rotational and irrotational components. If the rotational portion can be represented with, for example, a known vortex sheet, the above method can be implemented on the irrotational component and the two solutions superposed. This allows for a rotating circular cylinder by solving for a non-rotating cylinder and adding a constant strength sheet to account for the rotation. Note that image vortices cannot be used in the above

approach as this would place vorticity inside the body. The vortex sheets, on the other hand, are considered to lie infinitesimally outside the boundary. The primary advantage in the modified approach to (2.28) using $\kappa=0$ is to reduce the matrix required for a panel method solution by half.

The circular cylinder flows considered in this work are all external flows in which the boundary condition is satisfied as described above using $\kappa=0$. Koumoutsakos [1993] showed that in the case of a circular cylinder, a vortex sheet of distribution

$$\gamma(\theta)= 2\underline{u}_{slip}(\theta) \tag{2.36}$$

creates a discontinuity of $\underline{u}_{slip}(\theta)$ across the sheet. This relation can be used to satisfy the tangential condition explicitly and thus also the normal condition $\underline{u}\cdot\hat{n}=0$. Thus, for a circular cylinder, the panel method can be solved directly rather than requiring a matrix solver. Koumoutsakos [1993] also showed that a family of such direct solutions exists for elliptical bodies.

If such an explicit relation is not achievable, one need instead solve the relation

$$\frac{1}{2\pi}\oint\frac{\partial}{\partial n}\left[\ln\left|\underline{x}(s)-\underline{x}'(s')\right|\right]\gamma(s')ds' = \underline{u}_{slip}(s) \tag{2.37}$$

which, upon removing the singularity and creating a principal value integral, becomes

$$\frac{1}{2\pi}\oint\frac{\partial}{\partial n}\left[\ln\left|\underline{x}(s)-\underline{x}'(s')\right|\right]\gamma(s')ds' - \frac{1}{2}\gamma(s) = \underline{u}_{slip}(s) \tag{2.38}$$

in order to create a tangential velocity discontinuity of $\underline{u}_{slip}$.

It is interesting to consider the alternate view of inviscid flow over bodies the above approach provides. For example, the flow over a circular cylinder reduces to a freestream represented by a potential $\phi(x,y)=kx$ and a vortex sheet $\gamma(\theta)$. In this form, there is in fact a no-slip condition on the cylinder surface even in inviscid flow, masked by the vortex sheet above the surface that in viscous flow diffuses to become a boundary layer.

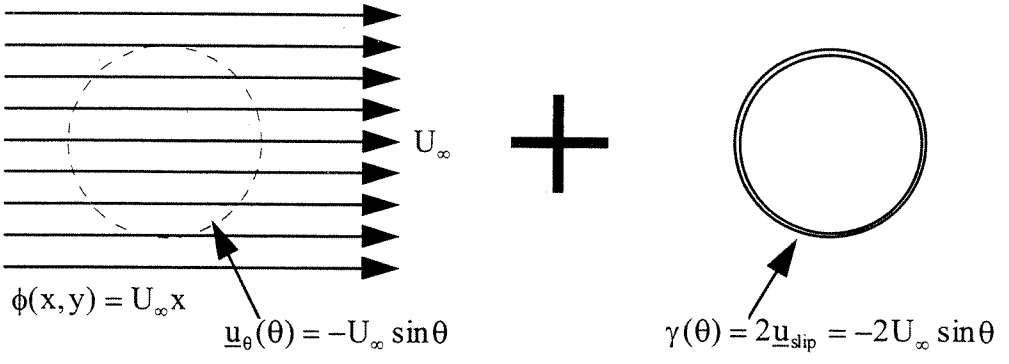


**Figure 4: Vortex method decomposition of inviscid flow over a circular cylinder.**

A bluff body flow that cannot be dealt with as above is the special case of an infinitely-thin plate, essentially a line segment for a two-dimensional domain. This boundary has no interior and thus satisfaction of the slip constraint does not necessarily imply that the normal velocity constraint has been met. However, the normal and tangential velocity constraints can still be satisfied while utilizing only a vortex sheet following the approach of Schmall et al. [1974] to exploit the unique geometry of the flat plate. A vortex sheet is established in the location of the plate to satisfy the normal velocity constraint and is considered to be divided between the two sides of the plate to satisfy the tangential velocity constraint. The method is clearly limited to situations where the tangential constraint is identical on opposing sides of the plate. As outlined in their work and in Koumoutsakos et al. [1996], the panel method can be avoided by using a series solution for the necessary distribution of vortex sheet strength.

## 2.2 Viscous Effects

### 2.2.1 Viscous Vorticity Equation

An inviscid representation of a flowfield provides a reasonable approximation in many situations. The importance of viscous effects will depend on the length and time scales of relevance in a flow, which can often be characterized by the Reynolds number. The Reynolds number Re relates the inertial and viscous effects in a flow and is defined as:

$$\mathrm{Re} = \frac{UL}{\nu} \tag{2.39}$$

where: U=characteristic velocity

L=characteristic length

ν=viscosity

In the flows studied in this paper, the inclusion of viscosity alters the vorticity equation to

$$\frac{D\omega}{Dt} = \nu\nabla^2\omega \tag{2.40}$$

Non-dimensionalization of this relation reveals the effects of Reynolds number

$$\frac{D\omega^*}{Dt^*} = \frac{1}{\mathrm{Re}}\nu\nabla^2\omega^* \tag{2.41}$$

$$\omega^* = \frac{\omega L}{U} \qquad t^* = \frac{tU}{L}$$

as well as the utility of Reynolds number as a single parameter defining the evolution of a system governed by (2.40).

Simulations presented in this paper include viscous effects because they are necessary to precisely compute bluff body flows and their related forces. Proper resolution of viscous effects is the hallmark of a high-resolution simulation. Viscous vortex methods utilize the particle-based approach introduced for the inviscid vorticity equation while including the effects of the viscous term in (2.40). The treatment of viscosity thus becomes an important, difficult issue as the method was constructed for inviscid convection and is not naturally suited for accurate evaluation of the Laplacian in the viscous vorticity equation.

### 2.2.2 Treatments of Viscosity

Vortex methods have been defined here as particle-based approaches to the simulation of the inviscid vorticity equation. Such a discretization of the vorticity field impedes accurate evaluation of the Laplacian viscous term due to scattered, unpredictable distributions of vortex particles. Application of a Laplacian finite difference stencil to the particle field requires sacrifices in both accuracy and computational efficiency due to the unstructured nature of the data. Thus, practitioners of vortex methods have studied a variety of novel approaches to evaluation of the Laplacian tailored to the data structure of vortex methods. The main contributions are touched upon below, and can be generally divided based on how much grid-dependence must be introduced for operation of the approach.

A common technique in most particle-based treatments of viscosity is the use of 'viscous splitting' to discretize (2.40). The splitting involves separating the convective and diffusive portions of the vorticity equation, using the traditional particle approach to convection and then utilizing one of the treatments of viscosity for diffusion. The convective step is solved as described above as it is simply inviscid field evolution

$$\frac{D\omega}{Dt} = 0 \tag{2.42}$$

which becomes

$$\frac{d\underline{x}_i}{dt} = \underline{u} \tag{2.43}$$

$$\underline{u}(\underline{x}) = \sum_i \underline{K}(\underline{x}_i, \underline{x})\omega(\underline{x}_i) \tag{2.44}$$

The diffusive step involves the solution of

$$\frac{\partial\omega}{\partial t} = \nu\nabla^2\omega \tag{2.45}$$

which can be seen to be simply the heat equation. One can apply the diffusive half of the splitting to the field pre-convection, post-convection or in a hybrid fashion such as measuring the Laplacian pre-convection but applying its effects post-convection.

The most straightforward viscous treatments simply use grid-based approaches from finite difference methods, facilitated by mapping data to and from the scattered particle locations. A structured grid is overlaid on the particle grid and data is

interpolated between the two grids in order to evaluate the Laplacian on the structured grid. Likewise, data can be mapped back from the grid to the particle locations or new particles can be created. There have been many implementations of this approach, such as in Chang et al. [1991]. This fundamental approach incurs both the penalty of needing to grid the flow domain and excessive numerical diffusion due to the interpolations between the Eulerian and Lagrangian grids.

On the opposite end of the spectrum are purely Lagrangian (i.e., grid-free) viscous methods. With the 'random walk' approach (cf. - Chorin [1973]), a pseudo-random component is added to the velocity of each particle. This 'random' component is set by a Gaussian distribution function whose variance is such that the walk simulates diffusion in the limit of infinite particles. The approach is ideal for particle methods in the sense that the vortex elements are independent of one another in the viscous substep and has probably been the most utilized method of diffusion in vortex methods literature. However, the random walk scheme has been shown to converge to the continuous solution at a slow rate (cf. - Milinazzo et al. [1977]) and in practice usually provides a stable but low-resolution simulation.

Other grid-free treatments are the 'core expansion' approach introduced by Leonard [1980] and the 'redistribution' scheme proposed by Subramaniam [1996]. The core expansion treatment uses a variable core size $\eta$ to solve the heat equation of the viscous step exactly. For a Gaussian vortex particle, the core size can be allowed to expand in time to thus simulate diffusion. It is preferable to the random walk method due to its stronger relationship to the physics of diffusion, thus yielding higher-resolution results. However, as in the Gaussian core case, the particle distribution can evolve such that localized remapping of the field becomes necessary. This does not require the introduction of a grid, though, as will be seen. The strengths and weaknesses of the core expansion approach are more extensively discussed below. The redistribution approach sets up systems of equations for local groups of particles to govern a redistribution of the particle strengths to simulate diffusion. This technique is also fully grid-free and can yield high-resolution in practice. However, it contains a fair share of 'tunable' parameters in a practical implementation and the need to solve systems of equations incurs

computational expense and reduces data structure flexibility (i.e., for concurrent implementation).

In between the fully gridded and purely Lagrangian treatments lie a variety of approaches that are formulated grid-free but require occasional remeshing of the particle field onto a well-ordered field for stability and accuracy. Although there are possible means to execute this remeshing without a grid, they have not been proven practical to date. In most instances, the techniques are not compatible with the distorted areas of the particle grid resulting from the large gradients of separated flow, thus necessitating remeshing onto a regular grid. The incompatibility is due to the fact that these remesh-dependent approaches involve approximating the Laplacian of the continuous vorticity field at a particle's location based on nearby particles, which is difficult when the particle field is unpredictably distributed. Random walk and core expansion address simply the diffusion of a single particle, exploiting the linearity of the heat equation governing diffusion, and thus avoid remeshing requirements. Although the redistribution method also categorized as grid-free is not such a pure particle approach, its reliance on systems of equations provides flexibility to deal with the unpredictable particle grid.

One remesh-dependent scheme, termed 'particle strength exchange' (PSE) (cf. - Degond et al. [1989]), uses a redistribution of the circulation (or strength) amongst the particles to approximate diffusion. Unlike the grid-free redistribution scheme, the PSE approach formulates a kernel which can be convolved with the vorticity field to approximate the Laplacian. The PSE method, also discussed in more detail below, yields high accuracy and can be implemented concurrently with the necessary field summation for determining velocities. Another scheme, termed the 'Fishelov' method, attempts to superpose the Laplacian of each particle's vorticity field to determine the Laplacian of the entire field (cf. - Fishelov [1990]), obviously encountering difficulties when the particle field gets distorted as derivatives of the distribution functions $\eta$ tend to be even more localized than the functions themselves. In Marshall et al. [1995], it can be observed on a test problem that the PSE approach handles particle disorder a bit more robustly than the sensitive Fishelov method, though both clearly break down as a field becomes strained.

| Grid Dependence | Treatment | Assessment |
|---|---|---|
| Grid free | Random Walk (Chorin [1973]) | Simple, straightforward, low-accuracy |
| | Core Expansion (Leonard [1980]) | Physically-based, good resolution control, needs particle splitting and merging |
| | Redistribution (Subramaniam [1997]) | Good resolution control and accuracy, not well suited to efficient computation |
| Partially Dependent - Require Remeshing | Strength Exchange (PSE) (Degond et al. [1989]) | High accuracy but poor resolution control |
| | Fishelov (Fishelov [1990]) | Demanding on uniformity of field |
| | Least-Squares (Marshall et al. [1995]) | Best of this class at dealing with particle field but not well-suited to efficient computation |
| | Diffusion Velocity (Strickland, et al. [1995]) | Conceptually appealing but implementation difficulties |
| Fully Dependent | Particle-to-grid (e.g., Chang, et al. [1991]) | Excessive error due to numerical diffusion |

**Table 1: Overview of treatments of viscosity**

A method proposed by Marshall et al. [1995] uses local systems of equations to compute least-squared fits to the vorticity field, which can be easily differentiated. They show this method exhibits superior stability to particle disorder than PSE and Fishelov, thus necessitating less frequent remeshing. However, it also incurs the drawbacks of the use of implicit techniques shared by the redistribution approach. A final approach of note is a variation on the random walk method where a velocity is added to the physical velocity to simulate diffusion (cf. - Strickland et al. [1995]). This treatment, termed 'diffusion velocity', has a stronger physical basis than random walk with the diffusion

velocity determined as a component which exactly replaces diffusion in the vorticity equation.

$$\frac{\partial \omega}{\partial t} + (\underline{u} \cdot \nabla)\omega = \nu \nabla^2 \omega = -(\underline{u}_D \cdot \nabla)\omega \qquad \underline{u}_D = \frac{\nu}{\omega} \nabla \omega \tag{2.46}$$

$$\frac{\partial \omega}{\partial t} + ((\underline{u} + \underline{u}_D) \cdot \nabla)\omega = 0 \tag{2.47}$$

Among the drawbacks to this approach is that it becomes very difficult to properly evaluate the diffusion velocity in various instances such as $\omega$=0.

### 2.2.3 Viscous Boundary

Implementation of inviscid boundary conditions was discussed above, including the use of a vortex sheet to meet both a tangential and normal velocity boundary condition. With the addition of viscosity and related slip boundary conditions, the utility of the inviscid method can now be realized. However, in a viscous flow, computation of the vortex sheet is only the first step in properly handling a boundary. It is well known that vorticity is in fact created at a viscous boundary, as epitomized by the vortex sheet. A constraint on the net circulation of the vortex sheet can be formulated based on the fact that an unbounded flow has constant circulation (absent of external forces). Thus, considering the known circulation of the vorticity field

$$\Gamma_\omega = \iint_{\text{flowfield}} \omega dA \tag{2.48}$$

and the circulation associated with the body motion $\underline{u}_B$

$$\Gamma_B = \iint_{\text{body}} (\nabla \times \underline{u}_B) dA\,, \tag{2.49}$$

the net circulation of the vortex sheet

$$\Gamma_\gamma = \oint \gamma(s) ds \tag{2.50}$$

is constrained by

$$\Gamma_\omega + \Gamma_B + \Gamma_\gamma = 0 \tag{2.51}$$

The vortex sheet is part of the vorticity field and thus physically spread by diffusion. Therefore, a further step is required in satisfying the boundary condition,

namely incorporating the vortex sheet into the particle field. As a simplification, classical vortex methods have neglected the process, claiming instead to simulate flow at an unknown high Reynolds number where the boundary layer is thin enough to resemble a vortex sheet. In order to deal with separated flow, either geometrical features or boundary layer theory are used to guide locations where the vortex sheet is transferred to vortex elements. Sarpkaya [1989] discusses various implementations of this approach. Use of such a 'disappearing viscosity' method facilitates both very fast computation and simulation of complex three-dimensional flow (e.g., study of flow over a reasonably detailed submarine by Strickland et al. [1993]) that would otherwise be inaccessible. However, the approach is not consistent with achieving high-resolution for bluff body flows due to the inherent complexities with the boundary layer and separation.

A popular approach to achieve higher resolution is to discretize the vortex sheet into a line of vortex elements, placing the elements a distance of $\delta$ off the body. This stand-off distance is a somewhat arbitrary parameter, although it can be related to the characteristic diffusion length or boundary layer thickness.

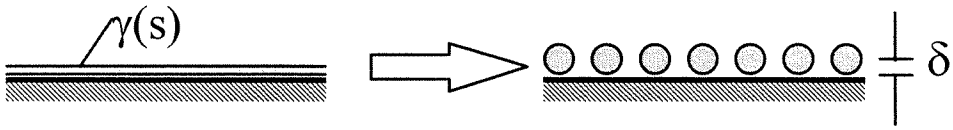


**Figure 5: Classical discretization of a surface vortex sheet.**

A far better link to the actual fluid dynamics is provided by a novel technique from Koumoutsakos et al. [1994] in which a solution is obtained for a physical problem closely related to the diffusion of the vortex sheet. This analytic solution can then be superposed onto the existing particle field.

The basis of Koumoutsakos' method is to segment the vortex sheets into panels, consider the diffusion of each panel on a semi-infinite domain, and superpose the solutions to all these problems. The problem one wishes to define on the semi-infinite domain (i.e., $0 \leq y$, $-\infty < x < \infty$) is an impulsive Neumann boundary condition for the heat equation.

$$\frac{\partial \omega}{\partial t} = \nu \nabla^2 \omega \tag{2.52}$$

$$\omega(\underline{x}, t = 0) = 0$$

$$\frac{\partial \omega}{\partial y}\left(|x| < \tfrac{dp}{2}, y = 0, t\right) = K$$

$$\frac{\partial \omega}{\partial y}\left(|x| > \tfrac{dp}{2}, y = 0, t\right) = 0$$

It will be seen that the vorticity flux term represents the existence of the vortex sheet to satisfy the boundary condition and its subsequent diffusion. Thus this model problem defines the vorticity field resulting from the diffusion of a non-curved vortex sheet segment of length dp.

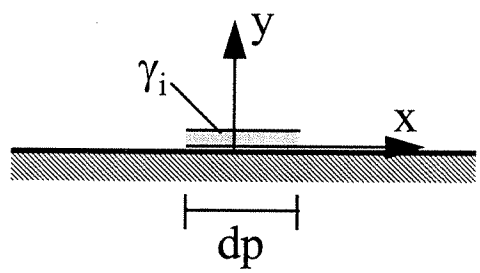


**Figure 6: Layout of model problem.**

The solution for this problem's vorticity field $\omega$ can be superposed onto the existing field, transferring the vortex sheet to the particle field in a physically-motivated manner. The segment dp represents a panel of the vortex sheet. As will be seen below, the constant K can be explicitly related to the value of the piecewise constant discretization $\gamma_i$ of the vortex sheet. Clearly the discretization, assumption of non-curved panels, and use of a semi-infinite domain deviate from the physical circumstances of a general body but provide a reasonable approximation which has a closed-form solution.

As outlined in Koumoutsakos [1993], the solution of the above semi-infinite domain heat problem is:

$$\omega(x,y,t=\delta t) = -\int_{t-\delta t}^{t} \frac{\nu K \exp\left(-\frac{y^2}{4\nu(t-t')}\right)}{\sqrt{\pi\nu(t-t')}}\left[\operatorname{erf}\left(\frac{\frac{dp}{2}-x}{\sqrt{4\nu(t-t')}}\right)+\operatorname{erf}\left(\frac{\frac{dp}{2}+x}{\sqrt{4\nu(t-t')}}\right)\right] dt' \quad (2.53)$$

Numerically integrating with a second order scheme yields

$$\omega(x,y,\delta t) = -\frac{\nu K \delta t \exp\left(-\frac{y^2}{4\nu\delta t}\right)}{2\sqrt{\pi\nu\delta t}}\left[\operatorname{erf}\left(\frac{\frac{dp}{2}-x}{\sqrt{4\nu\delta t}}\right)+\operatorname{erf}\left(\frac{\frac{dp}{2}+x}{\sqrt{4\nu\delta t}}\right)\right] \quad (2.54)$$

A method to relate K to $\gamma$ was proposed using a global argument

$$\frac{d\Gamma_\gamma}{dt} = \tfrac{1}{\delta t}\oint \gamma(s)ds = -\nu\oint \frac{\partial\omega}{\partial n}(s)ds = -\nu\oint K(s)ds \quad (2.55)$$

and assuming equality of the integrands. An alternative is presented here firming the derivation by localizing to the specific segment of the vortex sheet.

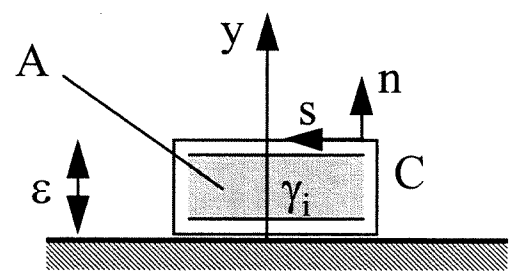


**Figure 7: Schematic of the surface flux/sheet strength proof.**

Consider a single segment of the discretized vortex sheet $\gamma_i$, lying inside an area A which is enclosed by a contour C. The circulation within this fixed contour C is:

$$\Gamma_{in} = \iint_A \omega dA \quad (2.56)$$

Taking the time derivative of this relation:

$$\frac{d\Gamma_{in}}{dt} = \iint_A \frac{\partial\omega}{\partial t} dA = \iint_A \nabla\cdot\left(\nu\nabla\omega - \underline{u}\omega\right)dA \quad (2.57)$$

for incompressible flow. Now applying Green's theorem yields

$$\frac{d\Gamma}{dt} = \oint_C \left(\nu\frac{\partial\omega}{\partial n} - \omega\underline{u}\cdot\hat{n}\right)ds \quad (2.58)$$

Now take $\varepsilon \to 0$ and designate (+) for $\hat{n} = \hat{y}$ and (-) for $\hat{n} = -\hat{y}$, assume quantities are piecewise constant on the panel, and use the fact that the normal velocity and vorticity are constant across the vortex sheet to yield

$$\frac{d\Gamma}{dt} = \nu\left(\frac{\partial\omega}{\partial n}(+) + \frac{\partial\omega}{\partial n}(-)\right)dp \tag{2.59}$$

Also,

$$\frac{\partial\omega}{\partial n}(-) = -\frac{\partial\omega}{\partial y}(y = 0) = -K \qquad \frac{\partial\omega}{\partial n}(+) = 0 \tag{2.60}$$

The flux is zero at (+) by definition of the model problem and fact that the solution yields this condition as well. Now using the fact that change in circulation sources from the vortex sheet

$$\frac{d\Gamma}{dt} = \frac{\gamma_i dp}{\delta t} \tag{2.61}$$

yields the desired relation

$$K = -\frac{\gamma_i}{\nu\delta t} \tag{2.62}$$

Thus (2.54) and (2.62) define the solution to the model boundary condition problem based on the strength of the local segment of the vortex sheet.

$$\omega(x,y,\delta t) = \frac{\gamma_i \exp\left(-\frac{y^2}{4\nu\delta t}\right)}{2\sqrt{\pi\nu\delta t}}\left[\operatorname{erf}\left(\frac{\frac{dp}{2} - x}{\sqrt{4\nu\delta t}}\right) + \operatorname{erf}\left(\frac{\frac{dp}{2} + x}{\sqrt{4\nu\delta t}}\right)\right] \tag{2.63}$$

The continuous field of this solution can then be discretized into multiple particles to accurately represent it or its effects can simply be mapped onto existing particles if the particle grid is well-ordered. This approach to discretizing the vortex sheet exhibits a much stronger physical basis than the classical approach pictured in Figure 5.

An interesting comparison can be made between the field (2.63), referred to as 'diffused sheet', and that of a point vortex placed at the center of a sheet segment with strength $\gamma_i dp$ and allowed to diffuse over a time step, resulting in the field

$$\omega(x,y,\delta t) = \frac{\gamma_i dp \exp\left(-\frac{y^2}{4\nu\delta t}\right)}{2\pi\nu\delta t}\exp\left(-\frac{x^2}{4\nu\delta t}\right) \tag{2.64}$$

on the half-plane. These two methods can be characterized against each other simply by their terms that differ:

$$\text{diffused sheet:} \quad \kappa(x) = \frac{1}{2\sqrt{\pi\nu\delta t}}\left[\operatorname{erf}\left(\frac{\frac{dp}{2} - x}{\sqrt{4\nu\delta t}}\right) + \operatorname{erf}\left(\frac{\frac{dp}{2} + x}{\sqrt{4\nu\delta t}}\right)\right] \tag{2.65}$$

$$\text{diffused point vortex:} \quad \kappa(x) = \frac{dp}{2\pi\nu\delta t}\exp\left(-\frac{x^2}{4\nu\delta t}\right) \tag{2.66}$$

These functions are plotted against each other below for various choices of parameters.

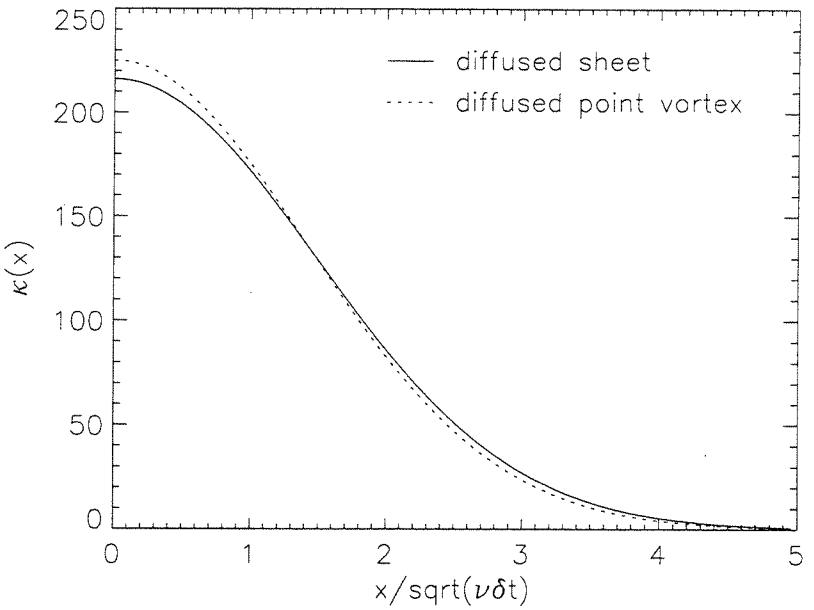


**Figure 8: $\nu$=0.0001, $\delta t$=0.01, dp=$\sqrt{2\nu\delta t}$ .**

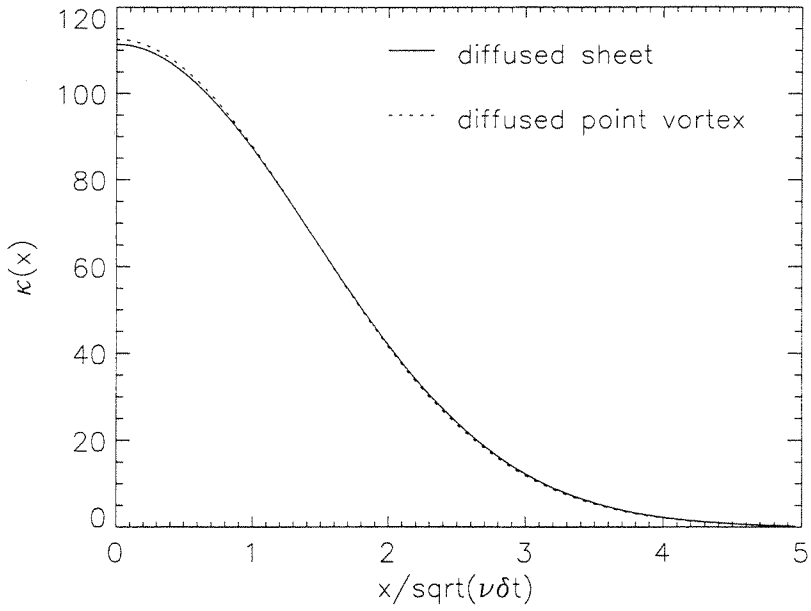


**Figure 9: ν=0.0001, δt=0.01, dp=$\sqrt{\frac{1}{2}\nu\delta t}$ .**

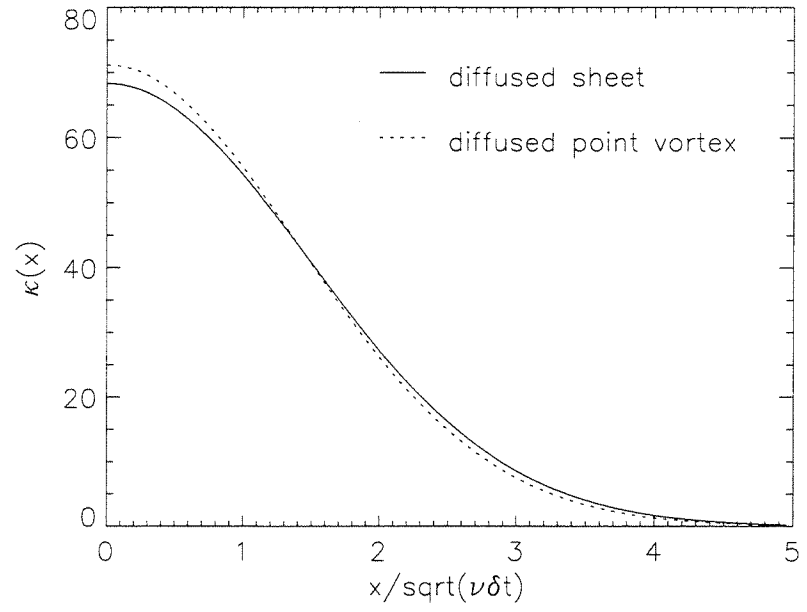


**Figure 10: ν=0.001, δt=0.01, dp=$\sqrt{2\nu\delta t}$ .**

As seen in the above tests, the diffused sheet representation is approximately the same as the pure diffusion of a source of circulation from the body surface. Note that the diffused sheet representation appears to converge to the diffused point vortex as $dp \to 0$. The effect of finite dp is a lesser peak vorticity for the diffused sheet, which is consistent with

expectations. The classical method where a vortex is placed slightly off the body to replace the vortex sheet will not usually coincide well with these physically-motivated results and doesn't have any great advantage in simplicity over (2.64), the diffused point vortex model.

Another noteworthy aspect of the behavior of (2.63) and (2.64) is the numerical boundary layer defined by their distributions. In order to properly discretize the flux, one must resolve to the length scales relevant to the functions $\kappa(x)$. Thus one must spatially resolve to scales of $O(\sqrt{\nu\delta t})$, as evidenced by the above study. This is uncoincidentally the well known characteristic length scale of diffusion.

### 2.2.4 Particle Strength Exchange

One of the two diffusion approaches used in simulations in this work is the Particle Strength Exchange (PSE) approach. As formulated by Degond et al. [1989] and co-workers, it is distinguished by high accuracy and algorithmic requirements that match those required for fast computation of convection. It can be viewed as an attempt to approximate the Laplacian by considering the Taylor expansion of the vorticity field and convolving the field with functions that remove low order derivatives other than those in the Laplacian. The goal is to utilize kernels $\kappa(r)$ such that

$$\nabla^2\omega(\underline{x}) \approx \iint \left(\omega(\underline{y}) - \omega(\underline{x})\right)\kappa(\underline{y},\underline{x})d\underline{y} \tag{2.67}$$

Considering the Taylor expansion of $\omega(\underline{y})$ about $\underline{x}$

$$\omega(\underline{y}) = \omega(\underline{x}) + \left((\underline{y}-\underline{x})\cdot\nabla\right)\omega(\underline{x}) + \tfrac{1}{2}\left[\left((\underline{y}-\underline{x})\cdot\nabla\right)\left((\underline{y}-\underline{x})\cdot\nabla\right)\omega(\underline{x})\right] + \cdots \tag{2.68}$$

it can be shown that if

$$\iint\left[\prod_{i=1}^{n}(\underline{y}-\underline{x})_i\right]\kappa(|\underline{y}-\underline{x}|)d\underline{y} = 0 \quad 1 \le n \le r+1 \tag{2.69}$$

$$\iint(\underline{y}-\underline{x})_i(\underline{y}-\underline{x})_j\kappa(|\underline{y}-\underline{x}|)d\underline{y} = \begin{matrix} 2 & i=j \\ 0 & i\neq j \end{matrix}, \tag{2.70}$$

then, where $\varepsilon$ is a length scale associated with the kernel $\kappa$,

$$\nabla^2\omega(\underline{x}) = \iint \left(\omega(\underline{y}) - \omega(\underline{x})\right)\kappa(\underline{y},\underline{x})d\underline{y} \quad + \quad O(\varepsilon^r) \tag{2.71}$$

The choice used for simulations in this work is the Gaussian

$$\kappa(\rho) = \tfrac{4}{\pi} e^{-\rho^2} \tag{2.72}$$

which yields second-order accuracy (r=2). This is a convenient choice as it is also used for the vortex particle distribution function. As a result, the exponential does not need to be computed a second time for the diffusion step.

In order to discretize (2.67) over the particle field, the approximation $\omega_i = \frac{\Gamma_i}{h_i^2}$ is used. Essentially, each particle is assumed to exclusively represent some fixed area of space $h^2$, and the vorticity is assumed to be constant over that region and defined by the strength of the particle. These assumptions lead to the severe stability requirements on the strength exchange method. A fairly uniformly ordered particle field is necessary to make these approximations behave accurately and the approach tends to go unstable once accuracy is reduced. For a field of Gaussian vortex particles with core size $\sigma$, stability requires one keep h as small as possible compared to $\sigma$ throughout the particle field. As h also represents the inter-particle spacing, this can become computationally expensive.

Naturally, the convection of vortex particles will lead to regions of the field where h becomes too large. In order to maintain stability and accuracy while using PSE, the particle field must be occasionally remeshed onto a new field defined by a structured grid. In this work, the remeshing is governed by conserving the first and second moments of the vorticity field except near grid boundaries. Bi-linear interpolation is utilized, with the interpolation kernel for a square grid with spacing d and distance x from the interpolation point given by

$$\Lambda\left(\tfrac{|x|}{d}\right) = \begin{cases} 1 - \left(\frac{|x|}{d}\right)^2 & 0 \le \frac{|x|}{d} \le \frac{1}{2} \\ \frac{1}{2}\left(1 - \frac{|x|}{d}\right)\left(2 - \frac{|x|}{d}\right) & \frac{1}{2} \le \frac{|x|}{d} \le \frac{3}{2} \\ 0 & \frac{|x|}{d} > \frac{1}{2} \end{cases} \tag{2.73}$$

The vortices are assumed to have point distribution while determining the remeshed field to provide the simplified remesh kernel above that conserves the first two moments of vorticity. As long as uniform core size is being used, the conservation properties are the same for particles with Gaussian distribution. However, if core size is variable, the

second moment of Gaussian particles will not be conserved with this approach. Although kernels can be constructed for the cells on the grid boundary, they introduce artificial oscillations in the vorticity field and thus nearest-grid point interpolation is instead used in these cases, conserving only the circulation. Obviously one would prefer to avoid remeshing both due to the need to define a grid and introduction of further error, but it is a necessity in this case due to the accuracy requirements of PSE.

The final details of the PSE implementation deal with the inclusion of a viscous boundary. The approximation to the Laplacian (2.67) is defined for an unbounded flowfield. As discussed earlier, in a vortex method regions outside the flowfield can be considered a part of the fluid that holds no vorticity. This makes it possible to utilize the unbounded Biot-Savart kernel, but cannot be used with the Laplacian approximation as that would dictate the creation of vorticity inside the body. Thus, the interior of the body is ignored in computation of the diffusive step. There have been no analyses to date on the error from this aspect of the PSE method, but as will be seen below, accurate computation is possible with this assumption.

A second boundary-related issue is transferring the diffused vortex sheet given by (2.63) or (2.64) to the particle field. One cannot simply introduce new particles as each particle must be associated with a region of space $h^2$ in order to discretize (2.67) as described above. Instead, the field of the diffused vortex sheet must be superimposed onto the existing particles. This is done by simply taking the value of the diffused sheet field, $\omega_{sheet}$ (as obtained in (2.63) or (2.64)), at the center of the existing particles $\underline{x}_i$ and inducing an adjustment to its circulation $\Delta\Gamma_i$ of

$$\Delta\Gamma_i = \omega(\underline{x}_i)h^2 \tag{2.74}$$

Particle strength exchange methods similar to that described above have been extensively tested by Koumoutsakos et al. [1993] [1995] and Pepin [1990], particularly on the flow over a circular cylinder - a canonical problem in the study of bluff body flows. Due to particular similarity with Koumoutsakos' work, extensive validations are not presented for the vortex method with PSE that will be utilized in later chapters. However, a few new validations serve as evidence of the high-resolution achievable with this approach.

In all PSE simulations in this thesis, uniform core size $\sigma$ and overlap ratio $\frac{h}{\sigma} \sim 1$ is used wherever strength exchange is applied. The choice for $\sigma$ is always in the range $\sqrt{2\nu\Delta t} \le \sigma \le 2\sqrt{\nu\Delta t}$, providing adequate boundary layer resolution. The field is also remeshed no less frequently than every five timesteps and the fast O(N) summation methods are used. Variables are all non-dimensionalized by cylinder radius or plate length and freestream velocity.

First consider validation of the vorticity field itself. In Figure 11 and Figure 12, the vorticity field resulting behind an impulsively started circular cylinder travelling in uniform linear motion (or in a constant freestream for a cylinder fixed frame) at Re=1000 is used to compare a simulation with the above particle strength exchange technique, a simulation with a spectral method, and experimental data obtained with Digital Particle Image Velocimetry (DPIV). Only half the domain is plotted as the flow is still symmetric at this time, though symmetry was not assumed in the simulations. Clearly, agreement with the high-resolution spectral method is excellent. The comparison with DPIV should be considered qualitative as the experimental method cannot achieve the level of resolution provided by the computations and involves three-dimensionality. In this regard, Figure 12 exhibits good agreement on qualitative features as well.

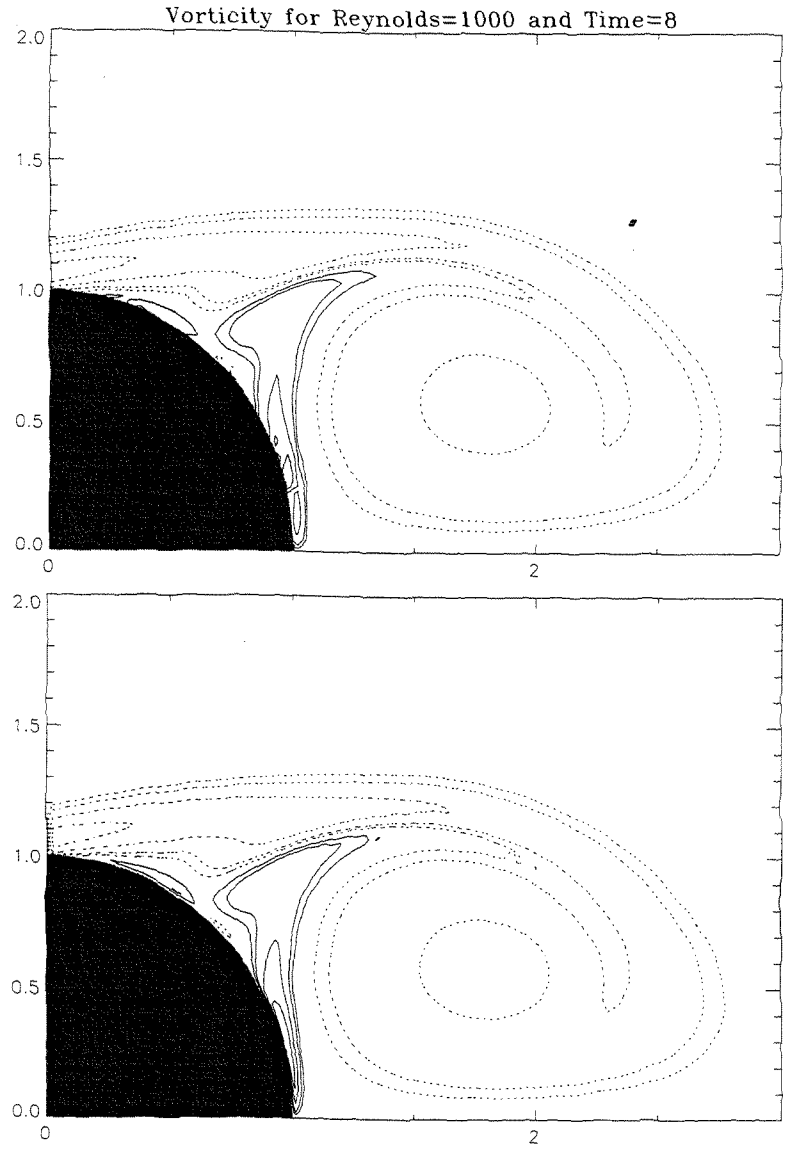


**Figure 11: Comparison of measured vorticity field, Re=1000 flow, tU/R=8; vortex method (top), spectral method Maheo et al. [1995] (bottom).**

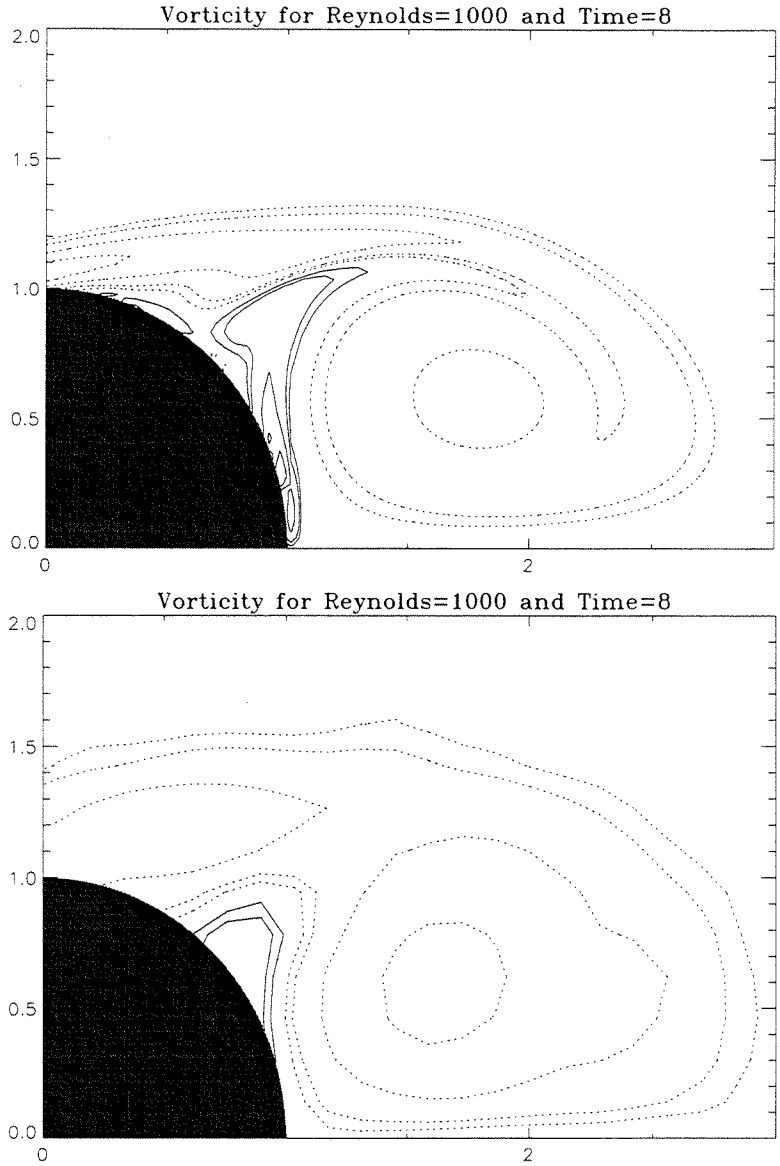


**Figure 12: Comparison of measured vorticity field, Re=1000 flow, tU/R=8; vortex method (top), DPIV Maheo et al. [1995] (bottom).**

Accurate measurement of bluff body forces can be difficult to achieve without sufficient resolution and thus forces serve as a discriminating method of validation. Techniques of force calculation are discussed in Appendix A. The drag force measured for impulsively started Re=3000 flow over a circular cylinder with the current vortex method is compared with results from a vortex method (Subramaniam [1996]) using the redistribution technique for diffusion and Henderson's [private communication] spectral methods. Agreement is very good as the methods yielded distinctly different results for

this sensitive parameter prior to full convergence. The PSE vortex method was run with a timestep of dt=0.01 and spatial resolution $\sigma^2=2\nu dt$.

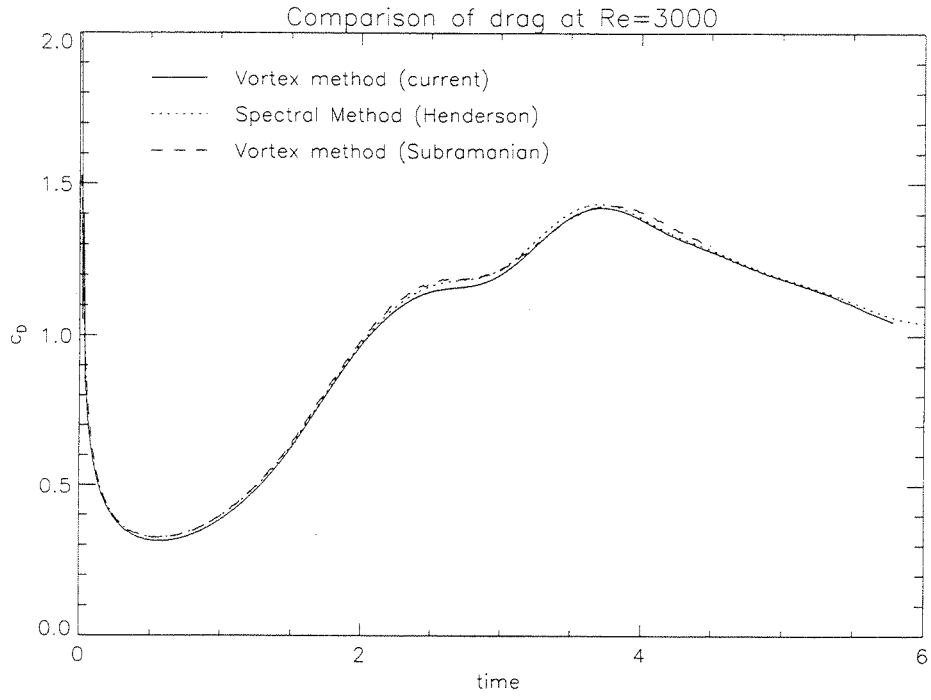


**Figure 13: Comparison of drag measurements for Re=3000 flow over a cylinder from different simulations.**

The technique for implementing an infinitely thin flat plate boundary in the current vortex method was discussed above. Tests were run on flow perpendicular to a flat plate at Re=126, varying time step dt and spatial resolution ($\sigma^2=2\nu dt$). This validation proved the converge of the current computational technique, as seen in the plots of streamlines and vorticity contours in Figure 14. For both functions, the simulation converges for the tested resolution dt=0.02, as evidenced by agreement with the dt=0.005 simulation.

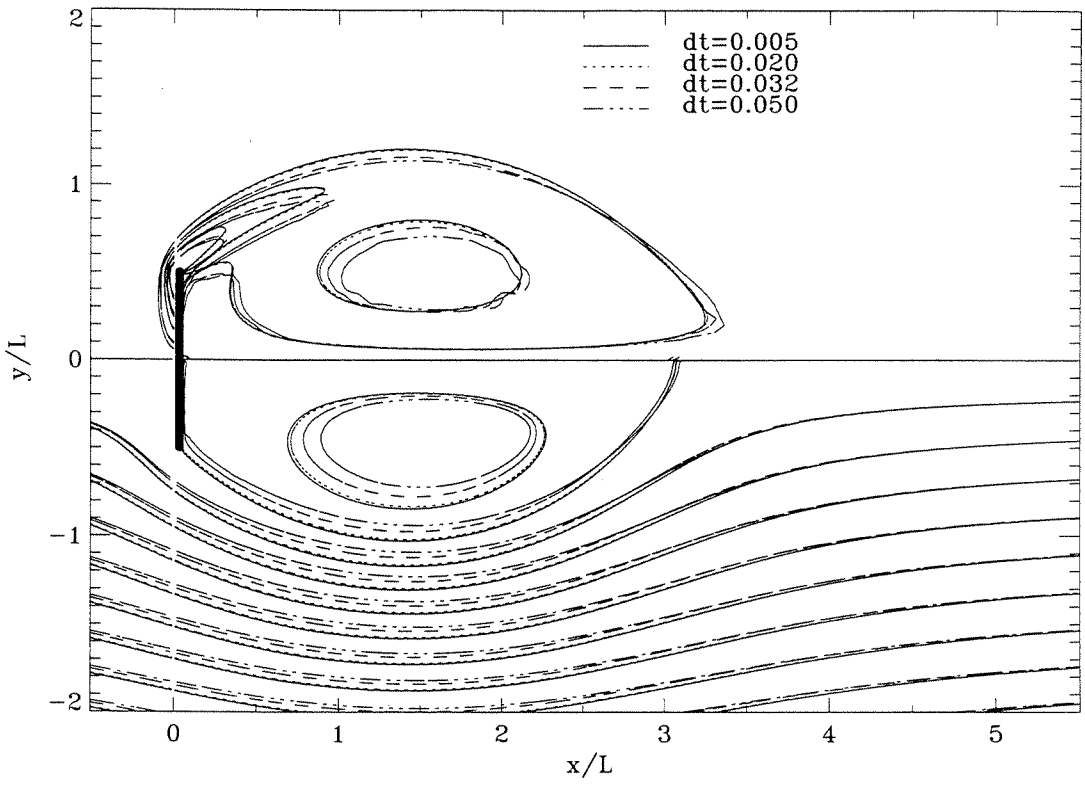


**Figure 14: Comparison of vorticity contours (top) and streamlines (bottom) for vortex method with varying levels of resolution, impulsively started Re=126 flow over a flat plate.**

A commonly used method of validation is comparison of computational results with experimental flow visualizations. Although such comparison has historically been valuable to link between computational results and experiments, flow visualization is in fact a far less discriminating validation than those provided above and with the advent of DPIV is no longer necessary for comparison with experimental results. However, for completeness, such a validation is provided in Figure 15, where streamlines from the current vortex method for Re=20 impulsively started flow are compared with aluminum flake visualization from the experiments of Dennis et al. [1993]. Although technically the same quantities are not being compared as the experimental visualization supplies pathlines, variations occur over a sufficiently long time scale to make the comparison valid.

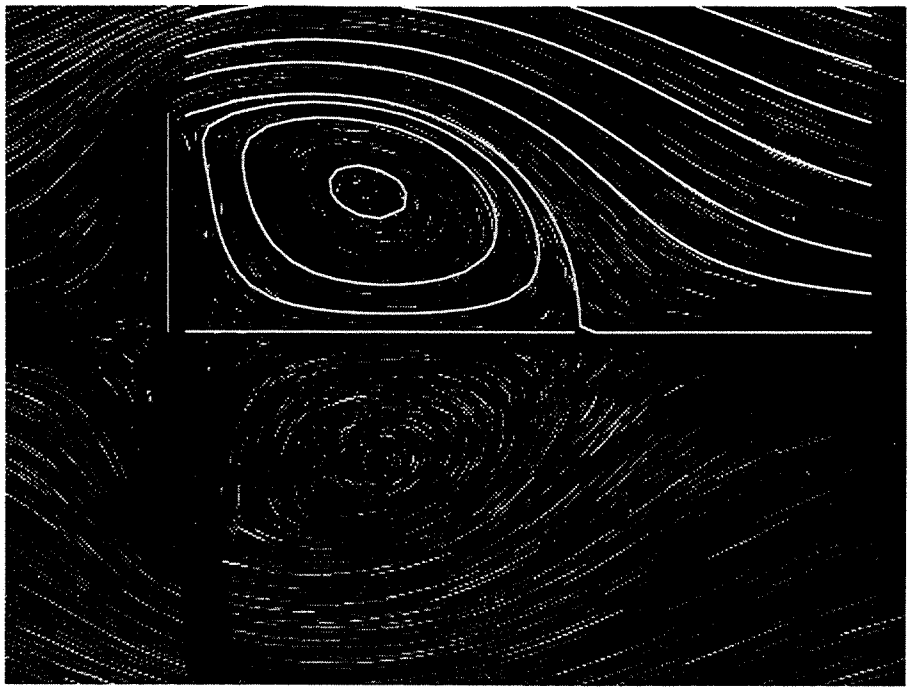

**Figure 15: Aluminum dust pathlines from experiment of Dennis et al. [1993] for impulsively started flow over a flat plate with streamlines from current vortex method simulation overplotted on upper half.**

The discussion of the particle strength exchange method above assumed a uniform $\sigma$ and h throughout the flow domain. Currently, strength exchange has only been formulated with such conditions and it remains questionable whether it can be constructed to allow much spatial adaptability with its stability constraints (work is currently underway on this topic by Koumoutsakos [private communication]). However, in bluff body flows, it is valuable to be able to adjust spatial resolution. The fine resolution which is required to resolve boundary layers can be excessive in the wake. A simplistic method has been constructed to allow for coarser resolution in the wake while maintaining an accurate strength exchange simulation near the body.

The new method is termed the 'inviscid far-wake' approach, for reasons that will become apparent. Once one considers flow beyond a few diameters downstream of the body, it can be conjectured that simulation errors in the downstream region will convect away from the body and have little effect on accurate simulation of the near-body region as effects scale inversely proportional to distance. Thus, a full particle strength exchange solution could be attempted in the near body region (with uniform particle sizes as

dictated by boundary layer resolution and copious particle overlap) while less particles can be used in the 'far-wake', treating this region as inviscid.

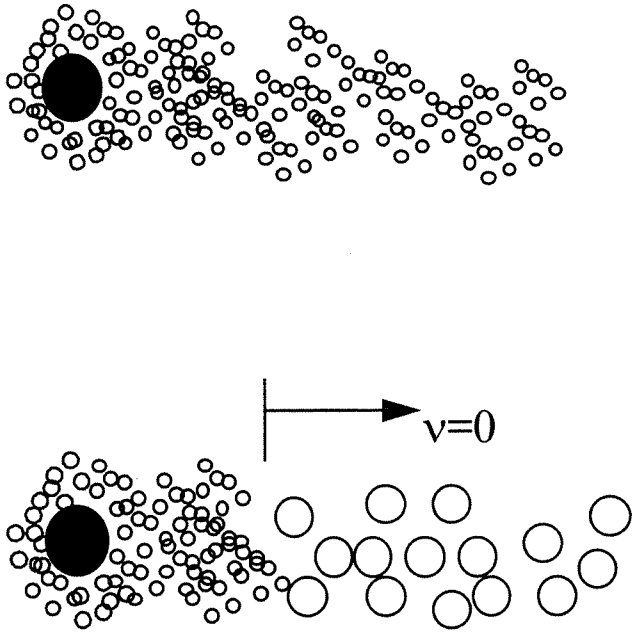


**Figure 16: Diagram of computational elements used for simulating flow over a cylinder. A full strength exchange simulation (top) and the adjustment to fewer wake particles in the 'inviscid far wake' approach.**

The idea of merging particles and neglecting diffusion in the far wake is tested on impulsively started Re=100 flow over a cylinder. In the 'merged' situation (i.e., where the inviscid far wake method is applied), the coarsening is allowed beginning six diameters downstream of the cylinder center. The approximate particle spacing is three times larger in this downstream region, allowing for an order of magnitude fewer particles and making such simulations much more feasible. The results in Figure 17 and Figure 18 demonstrate that although the vorticity field in the downstream region is clearly affected by the inviscid approach, the differences with the fully viscous approach do not propagate upstream to any significant degree. As the Reynolds number goes even higher, one expects the inviscid wake method to become more and more accurate as the viscous influence lessens.

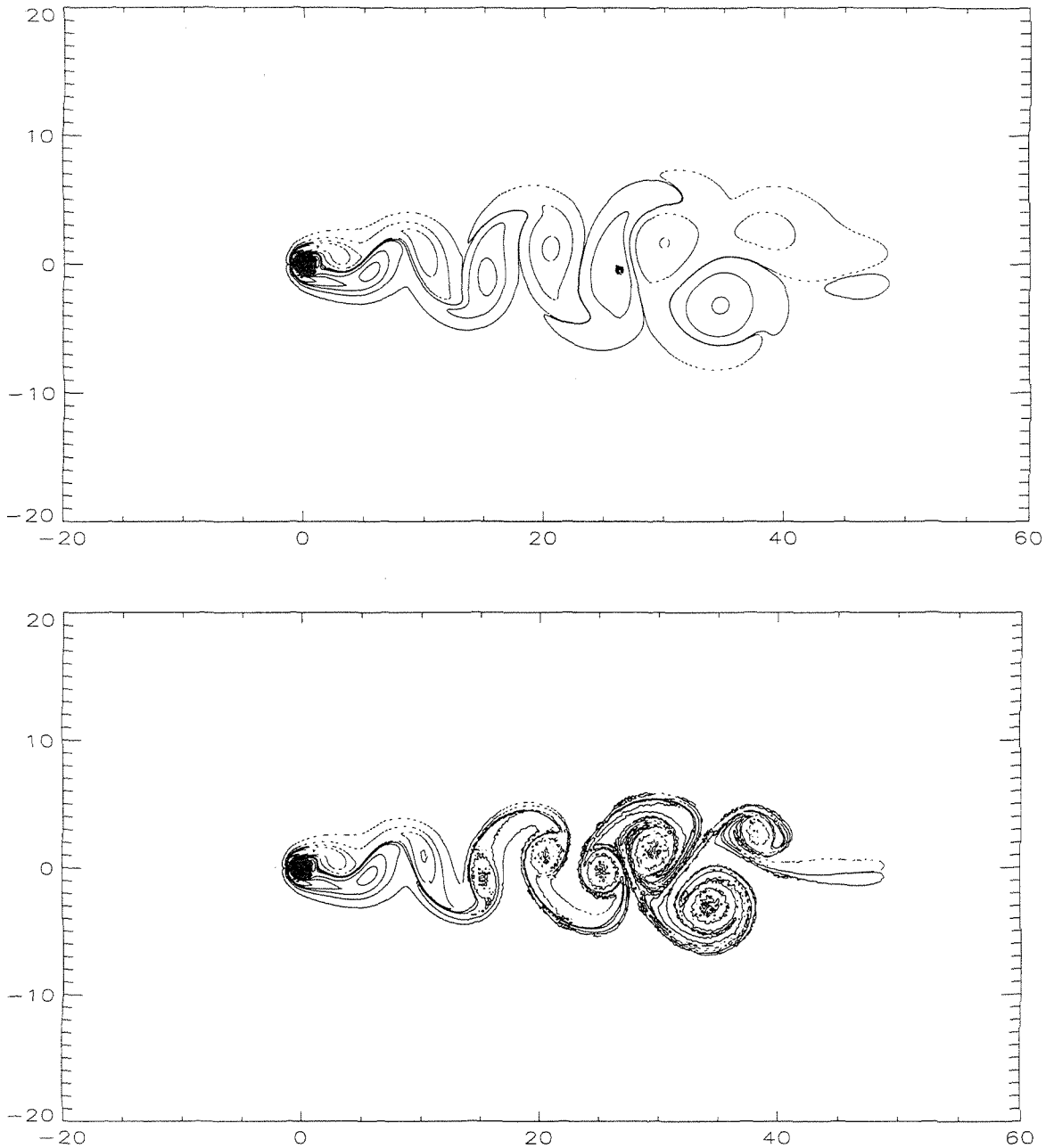


**Figure 17: Vorticity contours at tU/R=50 for Re=100 flow, full strength exchange simulation (top) and 'inviscid far wake' method (bottom)**

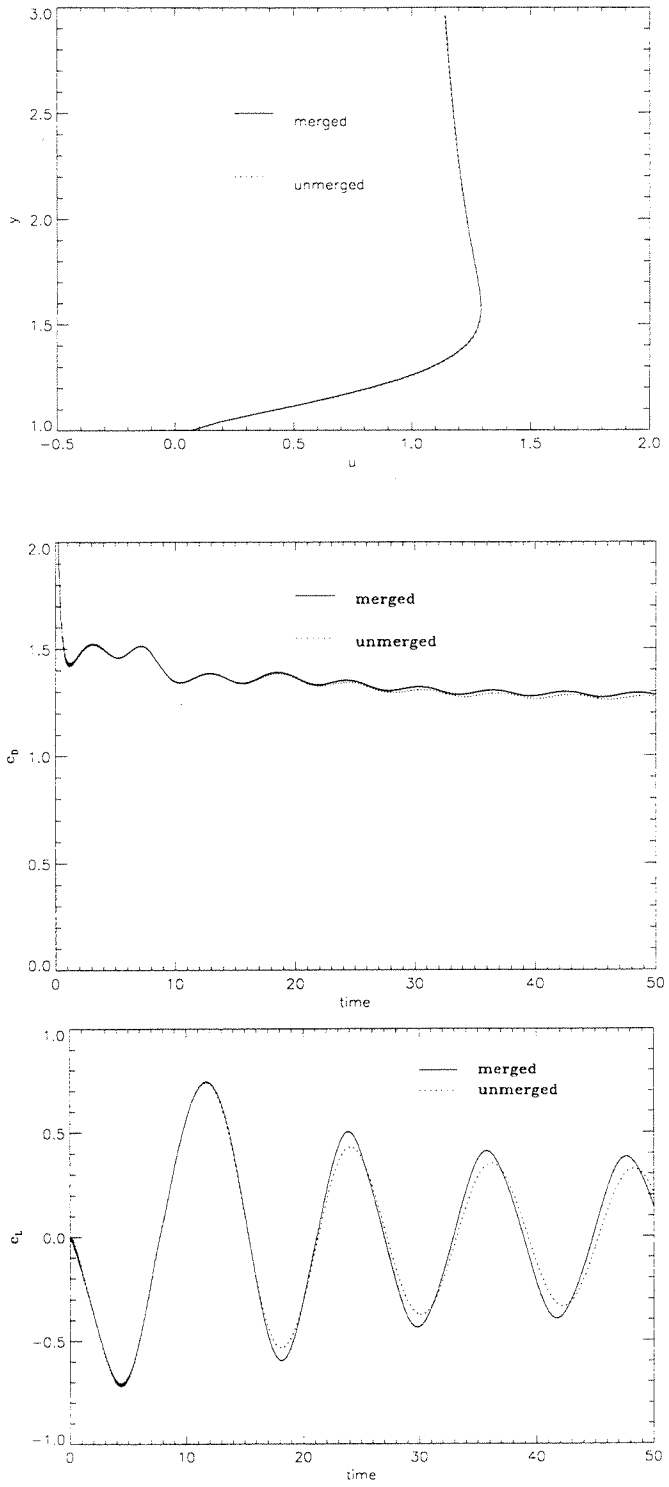


**Figure 18: Data from simulation detailed in Figure 17, comparing simulations with and without 'inviscid far wake' approach. Pictured are: velocity profile at $\theta=90^o$ (top), drag coefficient (middle) and lift coefficient (bottom).**

Thus the 'inviscid far wake' approach makes it possible to run a high resolution strength exchange vortex method beyond simply starting flow. However, the need to use the boundary layer resolution uniformly in the interior region again becomes too costly as one attempts higher Reynolds numbers. As a result, the core expansion viscous approach is also studied in this work as described below for applicability to such problems.

### 2.2.5 Core Expansion

#### 2.2.5.1 Introduction

Vortex methods utilize a particle description to represent the vorticity field such that the field is given by

$$\omega(\underline{x},t)=\sum_{i=1}^{N}\Gamma_i(t)\eta(|\underline{x}-\underline{x}_i|,t) \tag{2.75}$$

The core expansion method is unique among viscous treatments because rather than attempting to simulate viscous effects through modification of $\Gamma_i$ or $\underline{x}_i$, it utilizes a time-dependent core function $\eta$. Due to the linearity of the diffusion equation, this enables the use of an exact solution for the viscous effects in the vorticity equation. Taking the vorticity field as

$$\omega(\underline{x},t)=\sum_{i=1}^{N}\Gamma_i\eta(|\underline{x}-\underline{x}_i|,t) \tag{2.76}$$

along with the previously introduced Gaussian core function

$$\eta(|\underline{x}-\underline{x}_i|,t)=\frac{1}{2\pi\sigma(t)}e^{-\frac{|\underline{x}-\underline{x}_i|^2}{2\sigma(t)^2}} \tag{2.77}$$

the diffusion equation governing the viscous step

$$\frac{\partial\omega}{\partial t}=\nu\nabla^2\omega \tag{2.78}$$

is exactly satisfied if

$$\frac{d\sigma^2}{dt} = 2\nu \tag{2.79}$$

Thus, the core expansion technique involves expanding the core size of the Gaussian particles each time step $\Delta t$ by

$$\sigma^2(t+\Delta t) = \sigma^2(t) + 2\nu\Delta t \tag{2.80}$$

An issue to keep in mind, however, is that although the diffusion is simulated exactly by this method, the convective error which scales as $O(\sigma^2)$ with Gaussian particles is impacted by the expansion of the core function. Other choices are possible for the core function $\eta$, and the method can even be extended to handle an anisotropic viscosity as in Leonard [1997], but the Gaussian is exclusively used in this work as discussed earlier.

The basic approach of core expansion described above was proposed by Leonard [1980] but objected to by Greengard [1985] based on a lack of convergence in the limit of infinitesimal parameters. Of course, the method described above is clearly incomplete as the core size cannot be allowed to grow without bound in light of the convective error. Implementations of the approach that recognize the above shortcomings have included localized remeshing, in which a particle can be split into multiple new particles with smaller $\sigma$.

**Figure 19: Particle splitting - the solid particle is split into three dashed particles of lesser core size.**

Rossi [1996] showed that core expansion with splitting was convergent. However, splitting leads to an excessive number of computational particles. This difficulty can be alleviated by allowing a merger of multiple particles into a single new element.

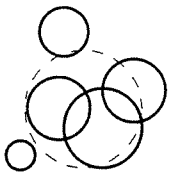

**Figure 20: Particle merging - the solid particles are merged into the single dashed particle of larger core size.**

The resultant method, with core expansion, splitting, and merging is fully grid-free and allows for precise control and easy adjustment of spatial resolution. Thus the core expansion method provides an alternative to the strength exchange technique with the potential to maintain high accuracy yet remain truly Lagrangian and provide the adaptability necessary to limit computational costs.

However, there has been relatively little development of the core expansion approach outside of Rossi's [1996] [1997] recent work. The crucial questions in the core expansion approach are how to formulate the splitting and merger of vortex particles. Rossi, as in some previous studies, chose the conservation of the zeroth (circulation), first, and second moments of vorticity as constraints. A study to determine the best choices for the constraints is presented below, as well as investigation of further complications arising from the inclusion of boundaries in the core expansion approach.

First, consider only the splitting step. As in past studies, the splitting is formulated by placing down an axisymmetric distribution of new particles to replace a single particle. An axisymmetric distribution is chosen because unbounded diffusion of a Gaussian has no angular dependence. The new particles of core size $\sigma_j$ are all placed at a radius r from the center of the original particle of core size $\sigma_i$. Another technique where one of the particles is instead placed at the original particle center is also explored later and seen to have no significant effect. The following parameters will be used in the discussion of the splitting step below:

$$\alpha = \frac{\sigma_j}{\sigma_i}$$

$$k = \frac{r}{\sigma_i}$$

A particle just prior to the splitting step will be referred to as a parent and the particles resulting from a split will be referred to as child particles. The circulation of a parent particle is distributed equally to its child particles. This scheme satisfies the zeroeth and first moment of vorticity constraints. Namely, for a particle of index i centered at location $\underline{x}_i$ being split into multiple particles of index j centered at locations $\underline{x}_j$,

$$\Gamma_i = \sum_{j=1}^{N} \Gamma_j \tag{2.81}$$

$$\Gamma_i \underline{x}_i = \sum_{j=1}^{N} \Gamma_j \underline{x}_j \tag{2.82}$$

independent of the number of particles of index j and the choice for radius r.

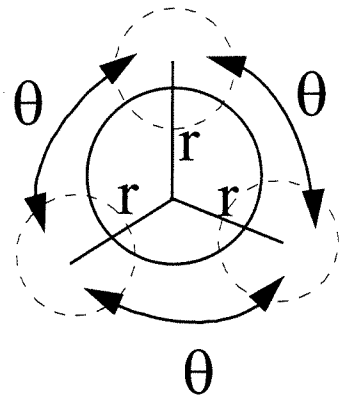


**Figure 21: Particle splitting from solid particle to dashed particles. The solid particle will be called a 'parent' and the dashed particles as 'children'.**

Thus the choice of r can be utilized to implement one more constraint. The traditional choice referred to above is conservation of second moment of vorticity, which for Gaussian particles can be expressed as

$$\Gamma_i\left(\left|\underline{x}_i\right|^2 + 2\sigma_i^{\,2}\right) = \sum_{j=1}^{N} \Gamma_j\left(\left|\underline{x}_j\right|^2 + 2\sigma_j^{\,2}\right) \tag{2.83}$$

For constraint (2.83), which will be referred to as the second moment constraint, the free parameter r is given by

$$r = \sigma_i \sqrt{2\left(1-\alpha^2\right)} \tag{2.84}$$

The splitting ratio $\alpha$ is assumed to lie between 0 and 1, and Rossi [1996] shows the error in the splitting behaves as $O(1-\alpha^2)$.

Clearly the parameter r is critical to the accuracy of the splitting step, but there is no known past work to assess other options for determination of r or to evaluate just how effective the second moment constraint limits splitting error. As the real goal in splitting is to reproduce the vorticity field as accurately as possible and not simply to conserve moments of vorticity, another logical choice for setting r that does not incur excessive computational overhead is to maintain the vorticity value at the pre-split particle's center $\underline{x}_i$. This constraint, referred to as the center vorticity constraint, can be expressed as

$$\frac{\Gamma_i}{\sigma_i^2} = \sum_{j=1}^{N} \frac{\Gamma_j}{\sigma_j^2} e^{-\frac{r^2}{2\sigma_j^2}} \tag{2.85}$$

which sets the splitting radius r as

$$r = 2\alpha\sigma_i\sqrt{-\ln(\alpha)} \tag{2.86}$$

Clearly (2.84) and (2.86) differ considerably, as is evident in Figure 27.

### 2.2.5.2 Determining Splitting: One-Dimensional Tests

To begin investigating the choice for the final constraint which determines r, consider a one-dimensional situation in which the effects of differing constraints can be examined clearly. A one-dimensional Gaussian particle is given as

$$\eta(x) = \frac{1}{\sqrt{2\pi\sigma^2}} e^{-\frac{x^2}{2\sigma^2}} \tag{2.87}$$

and the one-dimensional diffusion equation

$$\frac{\partial\omega}{\partial t} = \nu\frac{\partial^2\omega}{\partial x^2} \tag{2.88}$$

is exactly satisfied by the core expansion

$$\frac{d\sigma^2}{dt} = 2\nu \tag{2.89}$$

just as in the two-dimensional case. The expressions for r in the one-dimensional case are also identical to the two-dimensional situation. Tests below will examine the accuracy of the splitting alone for one-dimensional Gaussian particles.

Consider splitting a single one-dimensional parent into two children located a distance r on each side of the parent's center (a one-dimensional equivalent of the two-dimensional splitting schemes). As shown below in Figure 22, the center vorticity constraint is considerably more accurate in preserving the vorticity field of a parent particle over the splitting step. It is clearly seen that preservation of the second moment of vorticity does not necessarily imply the vorticity field itself is preserved. In Figure 23 it can be seen that the lesser accuracy of the second moment constraint is characteristic of the one particle splitting problem over all useful values for $\alpha$. The 'ideal' relation $r=f(\alpha)$ in Figure 23 was empirically found by canvassing the possible choices for r at given values of $\alpha$ and measuring the $L_1$ error created in the vorticity field by the splitting. The expected convergence of both constraints towards $r=0$ for $\alpha=1$ can be seen in this plot, as well as the significant discrepancy between the second moment and center vorticity constraints for values of $\alpha$ useful in a discrete computation.

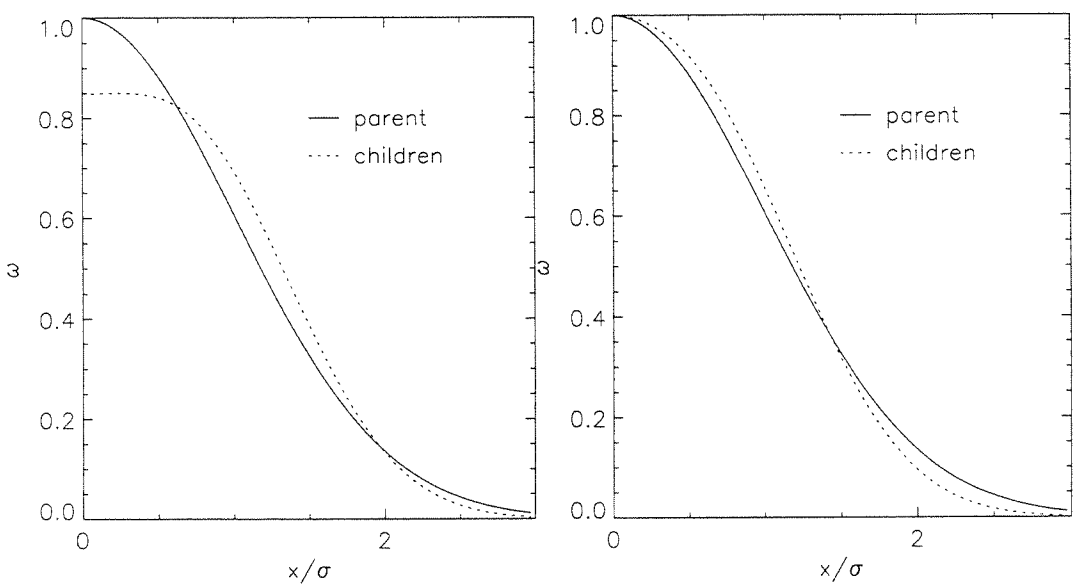


**Figure 22: The field of a one-dimensional particle (parent) and the combined field from the two particles replacing it (children), using $\alpha=0.7$. The constraint on the splitting radius r is second moment (left) and center vorticity (right).**

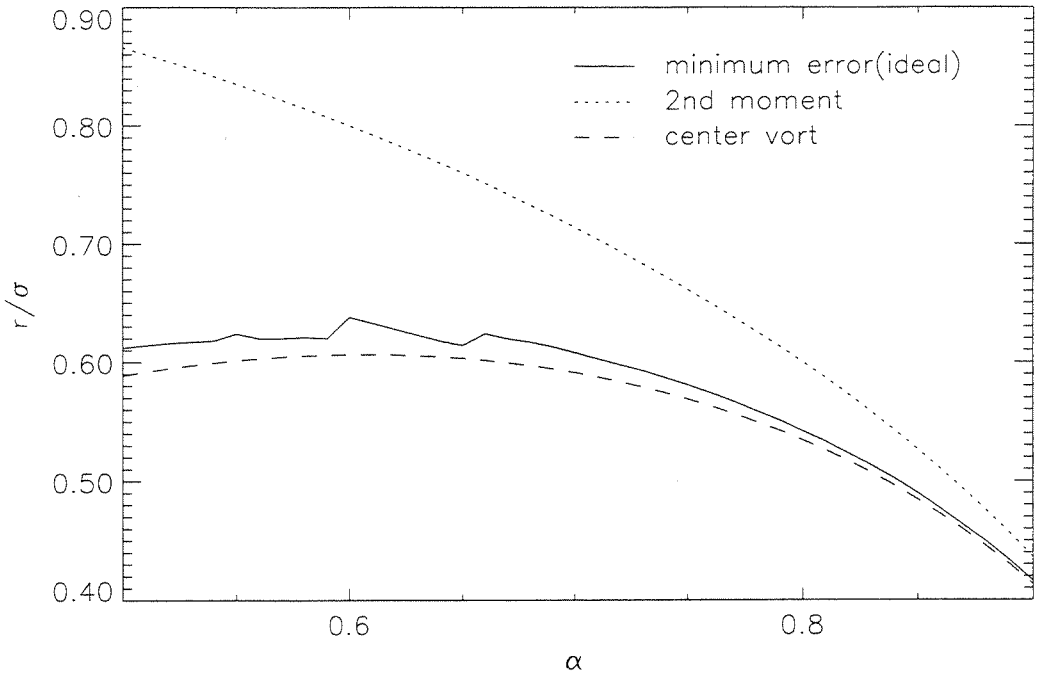


**Figure 23: The 'ideal' choice for splitting radius r (based on $L_1$ error) for the splitting of a single one-dimensional parent to two children compared to the second moment and center vorticity constraints.**

However, the results in Figure 22 also indicate that the splitting of a single particle is not the correct issue for evaluating a constraint on the radius r. Even for the more accurate center vorticity constraint, the error between the parent and child fields is significant. In high-resolution vortex methods, there will be much overlapping of the distributions of neighboring particles (typical spacing will have particles separated by $x/\sigma \sim 1$) so that the regions of error in Figure 22 will superpose, with possible amplification or cancellation of this error.

Thus, consider a one-dimensional case with eleven identical vortex particles, equally spaced by increments of $x/\sigma=1$ from -5 to 5, which are each split into two children. Such a field would be expected to exhibit a constant vorticity field in its center (where all relevant overlapping particles have been included). In the fully overlapped region, it can be seen in Figure 24 that error has been lowered greatly due to cancellation as compared to the single particle case. Furthermore, it appears that the center vorticity constraint yields less accurate results for this situation, unlike the single particle case.

Based on the results of testing this 11 particle scenario with range of splitting parameters (cf.-Figure 25), neither constraint clearly leads to 'ideal' splitting.

In fact, in various other one-dimensional tests using a variety of particle fields, neither constraint consistently leads to higher accuracy. It appears that the issue of preserving the vorticity field through the splitting step cannot be theoretically founded in one of the simple constraints proposed. A technique using multiple measurement points for error minimization tailored to the local particle field could certainly address the problem, but just as certainly entails excessive computational overhead.

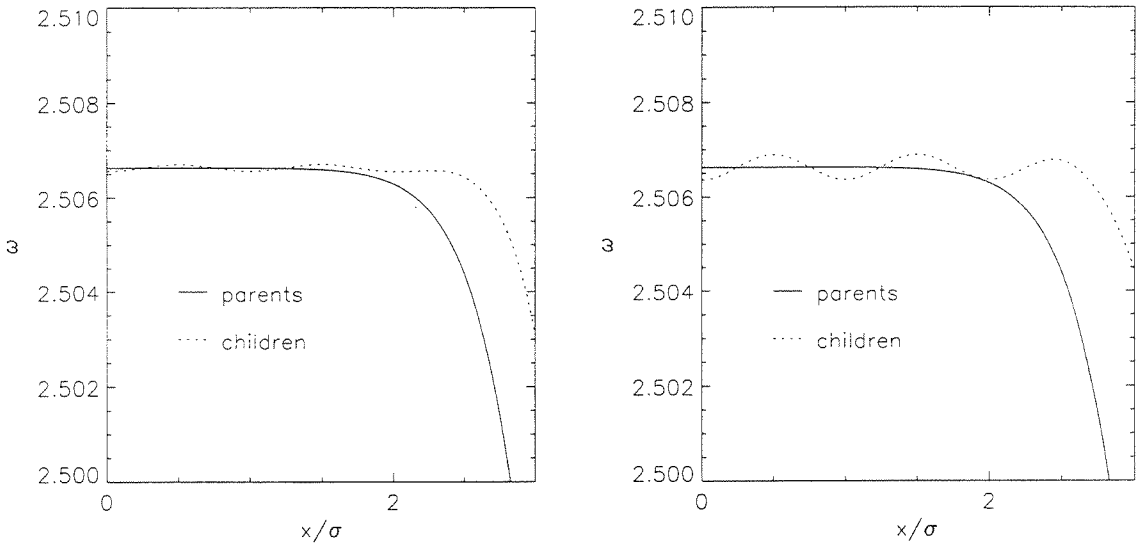


**Figure 24: The field from 11 identical one-dimensional particles (parents) and from the 22 particles replacing them (children), using $\alpha$=0.7. The final constraint used is second moment (left) and center vorticity (right). Note the limited scale on the y-axis.**

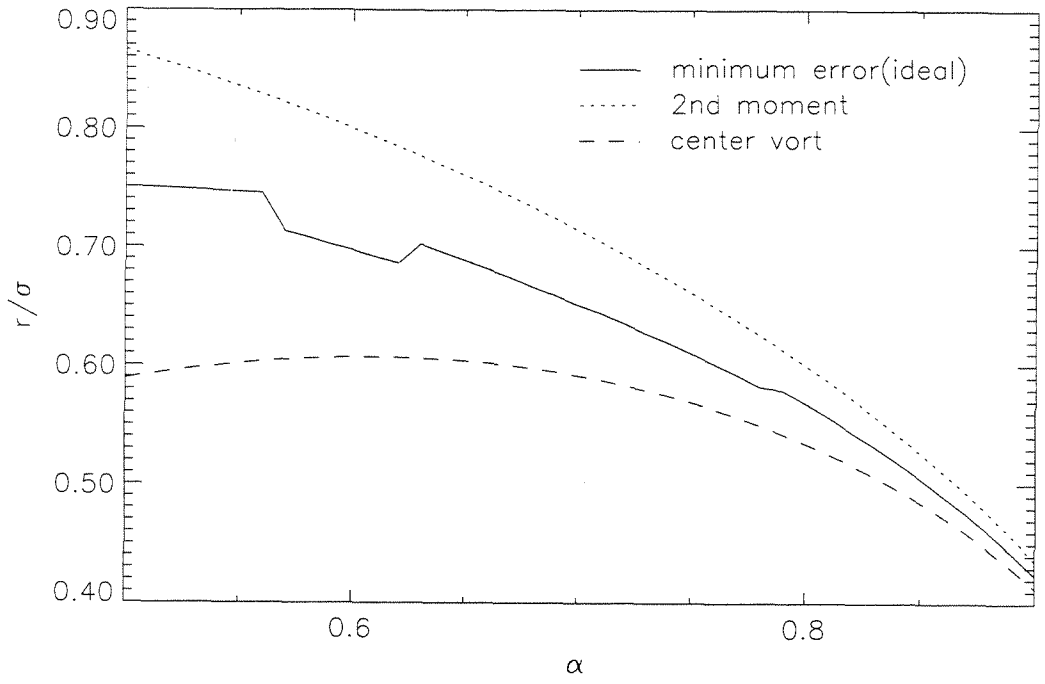


**Figure 25: The 'ideal' choice for splitting radius r (based on $L_1$ error) for the splitting of a single one-dimensional parent to two children.**

### 2.2.5.3 Determining Splitting: Two-Dimensional Tests

As the one-dimensional tests above do not indicate that either proposed constraint on the splitting radius r is ideal, a series of tests on a known two-dimensional exact solution are used to determine a r=f(α) relationship. The Lamb vortex

$$\omega(\underline{x},t)=\frac{\Gamma}{4\pi\nu t}e^{-\frac{|\underline{x}|^2}{4\nu t}} \tag{2.90}$$

is a known exact solution to the two-dimensional vorticity equation with the initial condition

$$\omega(\underline{x},t=0)=\Gamma\delta(x)\delta(y) \tag{2.91}$$

Simulations were undertaken using the Lamb vortex at t=1 with Γ=1 and ν=1 as an initial condition and a core expansion method with splitting from one parent to three children, unless otherwise noted. The simulations were run to t=2 with a timestep of Δt=0.02. The splitting radius is fixed as r=kσ for each case, where k is the constant introduced above, and the $L_1$ error measured on a velocity profile along a ray is used as a diagnostic. As a

point of reference, the $L_1$ error between the exact Lamb vortex and an inviscid simulation (where the t=2 profile would match the t=1 profile) is 0.0525. The simulations also utilize a merger scheme but, as will be discussed below, the choice of merger constraints does not seem critical to accuracy.

The tests were structured by sweeping over a range of choices for k for a given $\alpha$, using the measured error to define an ideal set of $(\alpha,k)$ pairs. The variation in results for a particular $\alpha$ can be seen in Figure 26, where as k is increased (and thus r increased), the method becomes more diffuse.

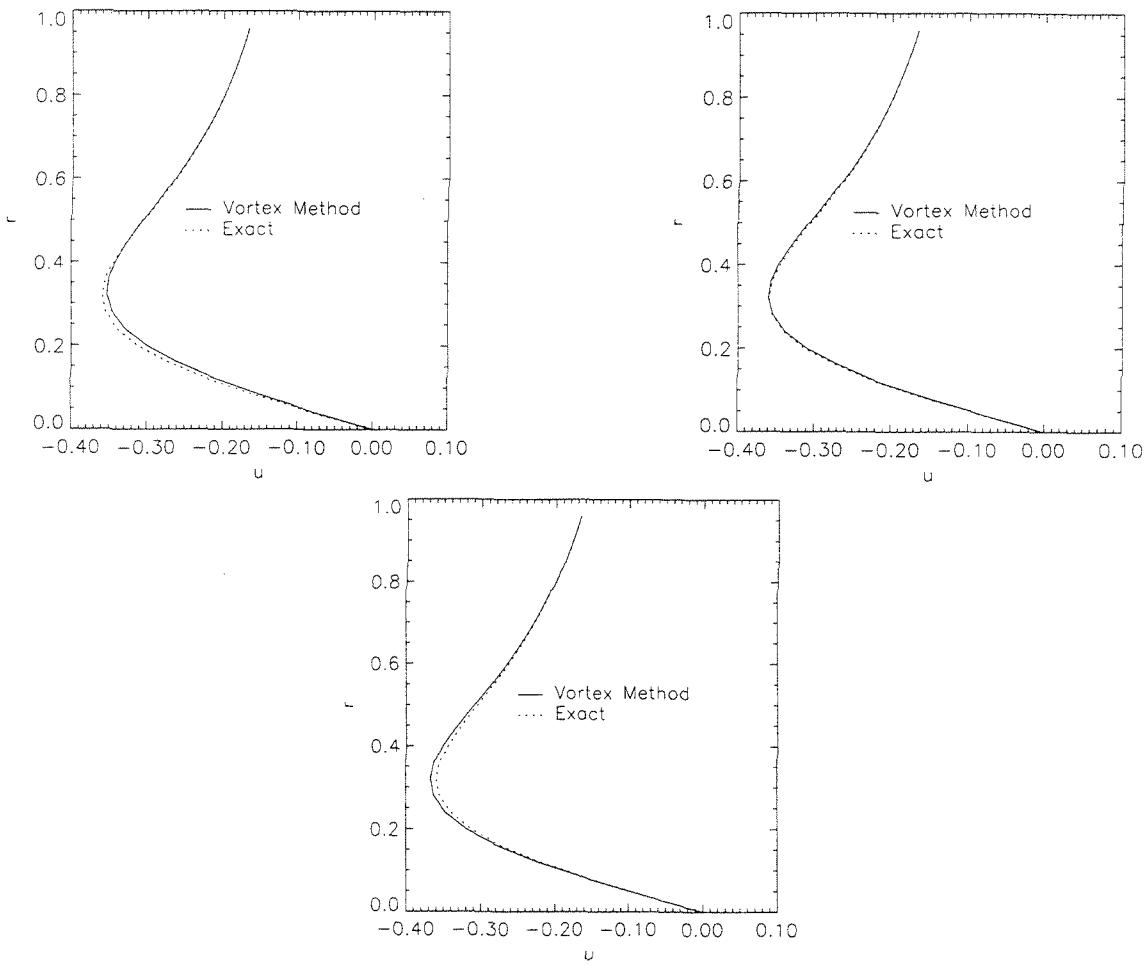


**Figure 26: Velocity profiles at $\theta=90^{\circ}$ for the Lamb vortex problem. Splitting based on $\alpha$=0.71, k=1.41 (error =0.0038) at top left, k=1.35 (error=0.0016) at top right, k=1.30 (error=0.0033) at bottom.**

A series of such tests were undertaken to flesh out a k=f(α) relationship. The results are plotted in Figure 27, labeled 'ideal', and compared to the k=f(α) curves resulting from the second moment and center vorticity constraints. A linear fit to the 'ideal' results from the tests is given by k=(3.9-3.6α), or

$$r(\alpha) = (3.9 - 3.6\alpha)\sigma_i \tag{2.92}$$

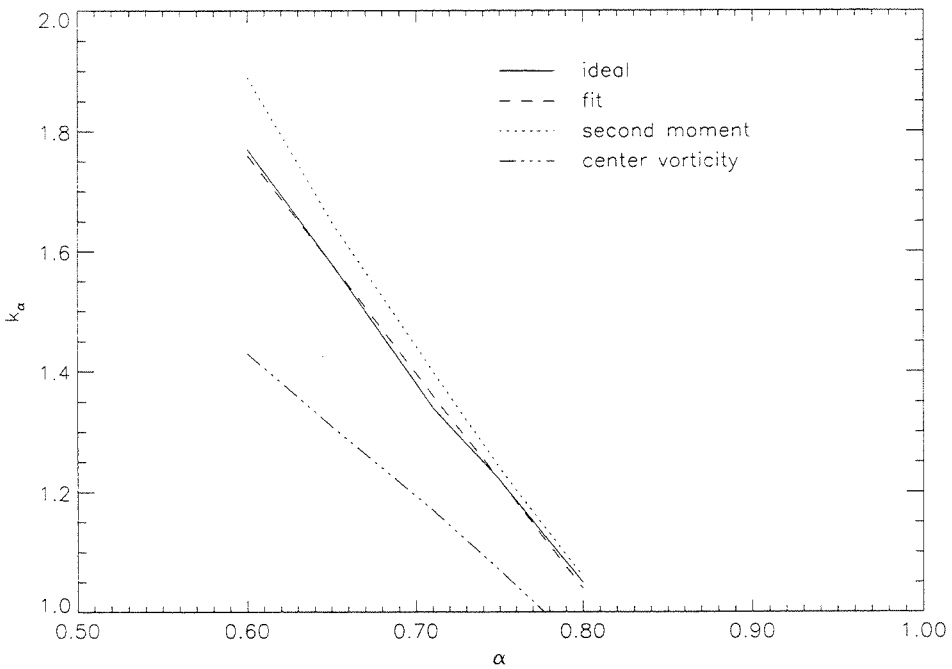


**Figure 27: The k=f(α) relationships: as measured in the Lamb vortex tests (ideal), based on the linear fit to the tests (fit), from the second moment constraint, and from the center vorticity constraint.**

Clearly, neither of the formal constraints (second moment or center vorticity) provide a good guideline for the splitting radius r.

Whether a different choice of child particle distribution than the axi-symmetric three particle scheme (diagrammed in Figure 21) would provide higher accuracy has not been thoroughly investigated. However, indications are that different distributions would not have a major effect compared to the sensitivity of the splitting radius r. The Lamb vortex problem was also simulated with a core expansion method in which a single parent was split into seven children, with six located axi-symmetrically at radius r and one at the center of the original particle. Their circulations were weighted by the value of the

vorticity field of the parent at the center of the child particles (i.e., giving the center particle a larger circulation than the other six). Results were similar to the three particle scheme, as seen in Figure 28, though the optimum choice for r differs.

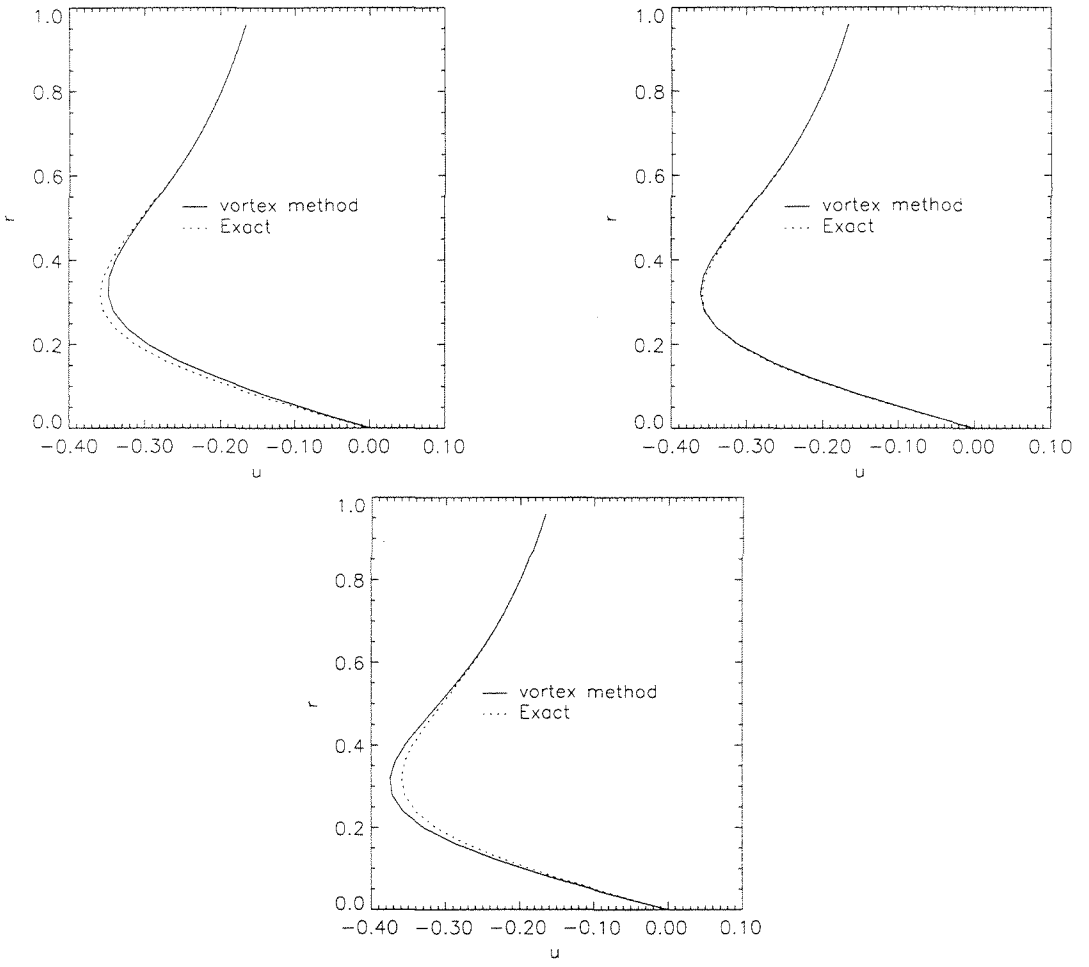


**Figure 28: Velocity profiles at $\theta=90^0$ for the Lamb vortex problem with a 1:7 splitting rather than 1:3. Splitting based on $\alpha=0.71$, k=1.69 (error =0.0053) at top left, k=1.55 (error=0.0013) at top right, k=1.41 (error=0.0059) at bottom.**

It is possible that more extensive study could reveal that splitting to seven particles or yet another more accurate choice is preferable to splitting to three. But the most sensitive choice seems to be the constraint to determine the splitting radius r.

As mentioned above, a merger step was also used in the Lamb vortex test simulations to control particle count. Merger does not simply invert the splitting step as it can be limited to only merge particles whose locations are relatively close, minimizing the error created in the vorticity field. The constraints of conservation of circulation and

first moment of vorticity are applied as with the splitting, defining the strength and location of a merged particle i based on the pre-merger particles j.

$$\Gamma_i = \sum_{j=1}^{N} \Gamma_j \tag{2.93}$$

$$\underline{x}_i = \frac{1}{\Gamma_i} \sum_{j=1}^{N} \underline{x}_j \Gamma_j \tag{2.94}$$

Constraints are placed on the merging of opposite-signed particles so that the term $1/\Gamma_i$ does not become problematic.

Again, a final constraint is available, but unlike the splitting case, the core size $\sigma$ is the remaining free parameter for the merging step. The center vorticity and second moment constraints have been considered in this work, where the second moment constraint results in the assignment

$$\sigma_i = \sqrt{\frac{1}{2\Gamma_i} \sum_{j=1}^{N} \left( \left| \underline{x}_j - \underline{x}_i \right|^2 + 2\sigma_j^{\,2} \right)} \tag{2.95}$$

and the center vorticity constraint results in

$$\sigma_i = \sqrt{\frac{\Gamma_i}{\sum_{j=1}^{N} \frac{\Gamma_j}{\sigma_j^{\,2}} e^{-\frac{\left| x_j - x_i \right|^2}{2\sigma_j^{\,2}}}}} \tag{2.96}$$

where again care is taken to assure that the denominators do not become ill-behaved. Results in the above tests showed no sensitivity to the choice of this constraint, nor did the merging step induce significant error compared to the splitting step as long as one followed reasonable guidelines such as not allowing merger between particles separated by more than a core radius.

#### 2.2.5.4 Incorporating Boundaries and Adaptive Resolution

The empirical studies above established the final elements of the basic implementation of the core expansion method used in this thesis. However, in order to simulate challenging bluff body flows, further issues must be addressed in terms of

defining the spatial adaptability of the technique and attempting to preserve accuracy in the vicinity of a viscous, no-slip boundary.

The core expansion technique allows for variable spatial resolution through control of the core size $\sigma$ with the splitting and merging processes. One approach is tested below on flow over a circular cylinder. In such flow, fine resolution is typically necessary near the cylinder, to resolve the boundary layer, while the relevant length scales are much coarser away from the body. Furthermore, as discussed in the particle strength exchange (PSE) section above, more error can be tolerated in the far wake, allowing larger minimum length scales there.

Informal testing led to the following definition for the core size of child particles based on location, assuming a cylinder radius of R=1 and freestream of U=1.

$$\sigma^2(r) = C\nu\Delta t \qquad r<r_{bl}\sigma_0$$

$$\sigma^2(r) = \left[K_{res}\left(r^2 - r_{bl}{}^2\sigma_0{}^2\right) + C\right]\nu\Delta t \qquad r>r_{bl}\sigma_0,\ \sigma^2<1/16$$

$$\sigma^2(r) = \tfrac{1}{16} \qquad \text{otherwise}$$

The parameter C should be related to the necessary resolution in the boundary layer (numerical and physical). Based on the discussion in the PSE section, it is typically chosen between 2-4, depending on the balance desired between accuracy and efficiency. Similarly, $r_{bl}$ is chosen to maintain the highest resolution near the body (and $\sigma_0$ is the core size for r=R). There is some investigation into the effects of varying $r_{bl}$ below. The other parameter considered below is $K_{res}$, which also allows one to scale between accuracy and efficiency as desired. Larger values of $K_{res}$ will yield fewer computational particles in a wake, but also result in a coarser resolution.

Special care must be taken near the boundaries to ensure that particles are not placed within the body during the splitting step. Some error is incurred in vortex methods when regularized particles lie close to the body, as a significant portion of the particle's vorticity field is then considered to lie within the boundary. An ad-hoc rule-of-thumb is to not allow a particle closer than half a core radius ($0.5\sigma$) to the boundary.

If during splitting the radius r is such that a post-fission particle might lie too close to the boundary, the three split particles are forced to align themselves with the boundary as diagrammed in Figure 29. The center of the closest particle (the post-

splitting particle which the dashed line passes through in Figure 29) is forced to lie at least $0.5\sigma$ from the boundary. If it initially is positioned closer to the boundary, it is moved outward along a ray to the center of the cylinder. If the near-boundary particle must be thus repositioned, its circulation is scaled down based on how far it is moved. The motivation behind the scale-down is to mimic the diffusive process near a semi-infinite boundary, which would be given by a core expanding particle and its image vortex inside the boundary, also undergoing core expansion. Thus the expansion into the boundary is reflected outward in a qualitative sense.

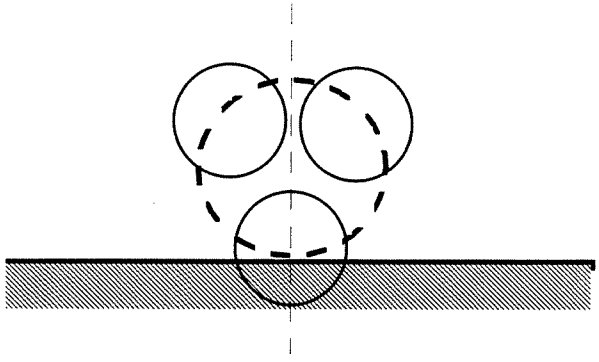

**Figure 29: Template for particle splitting near a boundary from one pre-splitting particle (dashed circle) to three particles (solid circles). The dashed line passes through the center of two particles as shown and is perpendicular to the flat panel boundary.**

Finally, the discretization of the diffused vortex sheet at the boundary can be handled in a more appropriate manner than in the PSE approach due to the grid free nature of the core expansion method outlined in this section. Rather than relying on the distribution of particles near the body for accurate mapping of the diffused vortex sheet, new particles are created to represent the field of the diffused vortex sheet. This is done with five particles per panel segment of the vortex sheet, placed as shown in Figure 30. The amount of sheet circulation distributed to each particle is weighted based on the value of the diffused sheet's vorticity field at each particle's center. Thus the central particle will receive the largest circulation.

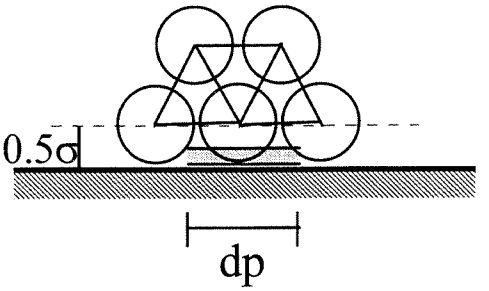


**Figure 30: Schematic of five particles used for discretization of the diffusion of a vortex sheet segment. Line segments drawn between particles are of length σ. The central particle lines up with the center of the sheet segment.**

The choices outlined above for adapting the core expansion method to a boundary were adopted based on informal testing, but are somewhat ad-hoc in nature and must be tested to measure the accuracy of this approach, as well as to understand the effects of the various additional parameters. The case of Re=100 flow over a circular cylinder is used for this validation. The flow is given an asymmetry to trigger vortex shedding by including a rotational oscillation in the cylinder's motion of $\Omega=0.5\sin(0.25\pi t)$ from t=0-8, with a freestream velocity U=1 and cylinder radius R=1. Beyond t=8, the cylinder is held rigid. Without in some way triggering an initial asymmetry, an accurate computation would take excessive time to generate sufficient numerical asymmetry to allow the vortex shedding instability to take hold. In physical situations, such asymmetric perturbations are always present to trigger shedding. As an added note, use of a constant freestream is interchangeable with constant linear motion of the body.

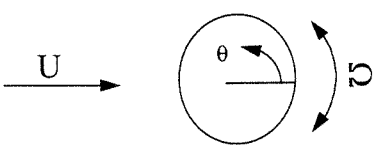


**Figure 31: Layout of flow over a circular cylinder with rotation.**

Two features of the Re=100 flow are used as diagnostics. The velocity profile at $\theta=90^\circ$ and t=8 is compared with the result from a converged PSE simulation. The known reliability of the PSE approach for the initial stages of flow over a circular cylinder is

discussed above. The vorticity field is also examined once the flow has clearly reached its periodic state, with contours plotted at $\omega=\pm0.5, \pm1, \pm2, \pm5, \pm10$. The simulations utilize a time step $\Delta t=0.02$, $r=k\sigma$ based on the fit given above, $\alpha=0.8$, spatial resolution based on $C=2$, $r_{bl}=15$ (unless otherwise noted), and values of $K_{res}$ as discussed below, and particle spacing (in vortex sheet discretization) of $h=\sigma$.

The vorticity field resulting from use of the PSE viscous method (with no adaptive spatial resolution but applying the inviscid, merged far-wake approach discussed earlier beyond six diameters downstream) is given in Figure 32. This simulation exhibits a shedding frequency $S_f=fD/U=0.170$ and an average drag coefficient over a shedding cycle of $c_D=1.33$, which agree to within 5% of established values, which themselves are slightly uncertain. Although the wake develops as anticipated, structures can be seen which are clearly an artifact of the inviscid nature of the far wake.

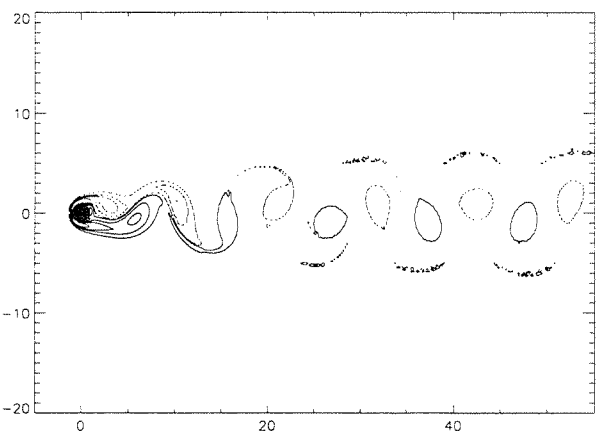


**Figure 32: Vorticity field for Re=100 flow, PSE approach.**

To explore the various parameters involved in the core expansion approach to this flow, first consider the adaptive resolution term $K_{res}$. The effects of different choices can be seen in Figure 33, Figure 34, and Figure 35. A clear tendency towards convergence can be seen as $K_{res}$ is refined. A further indication of this convergence is given by the measurement of $S_f=0.155$ and $c_D=1.33$ (averaged over a shedding cycle) for $K_{res}=0.25$ but a much less accurate $S_f=0.140$ and $c_D=1.48$ for $K_{res}=2$. All further Re=100 tests in this section use the conservative value of $K_{res}=0.25$.

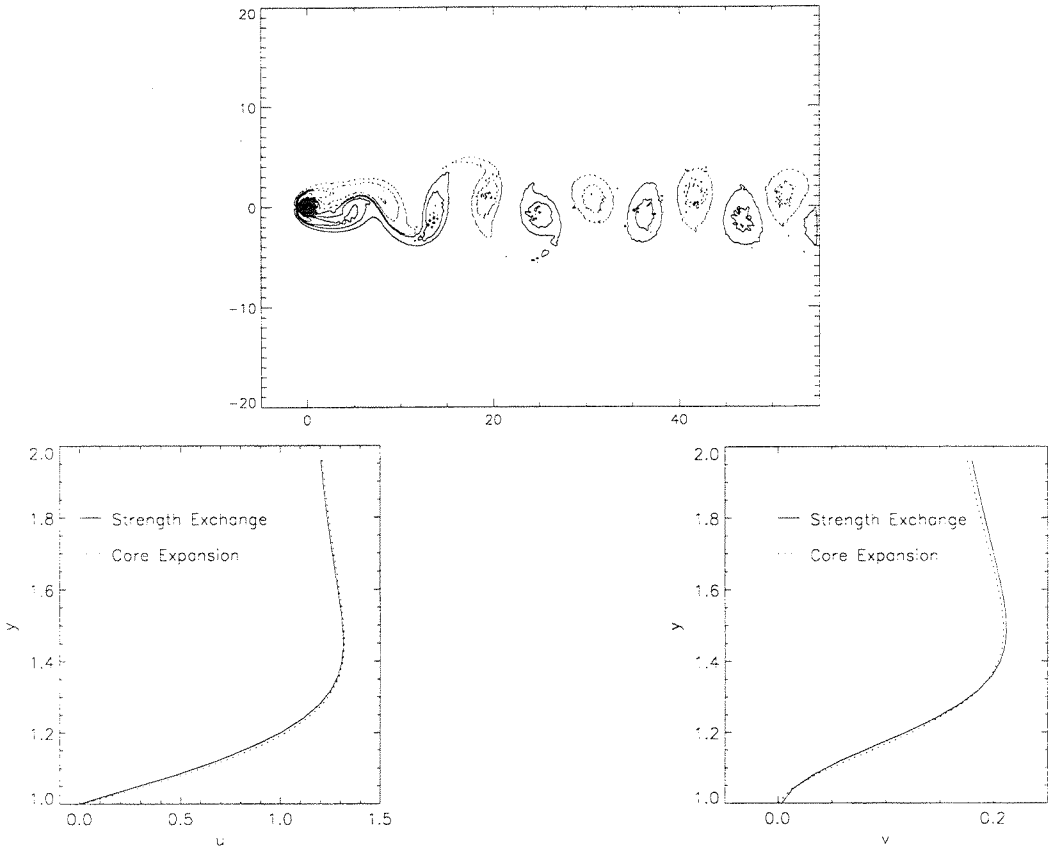


**Figure 33: Core expansion with $K_{res}$=0.25. Vorticity contours (top) and velocity at t=8 with u (left) and v(right) components across the boundary layer at $\theta$=90°.**

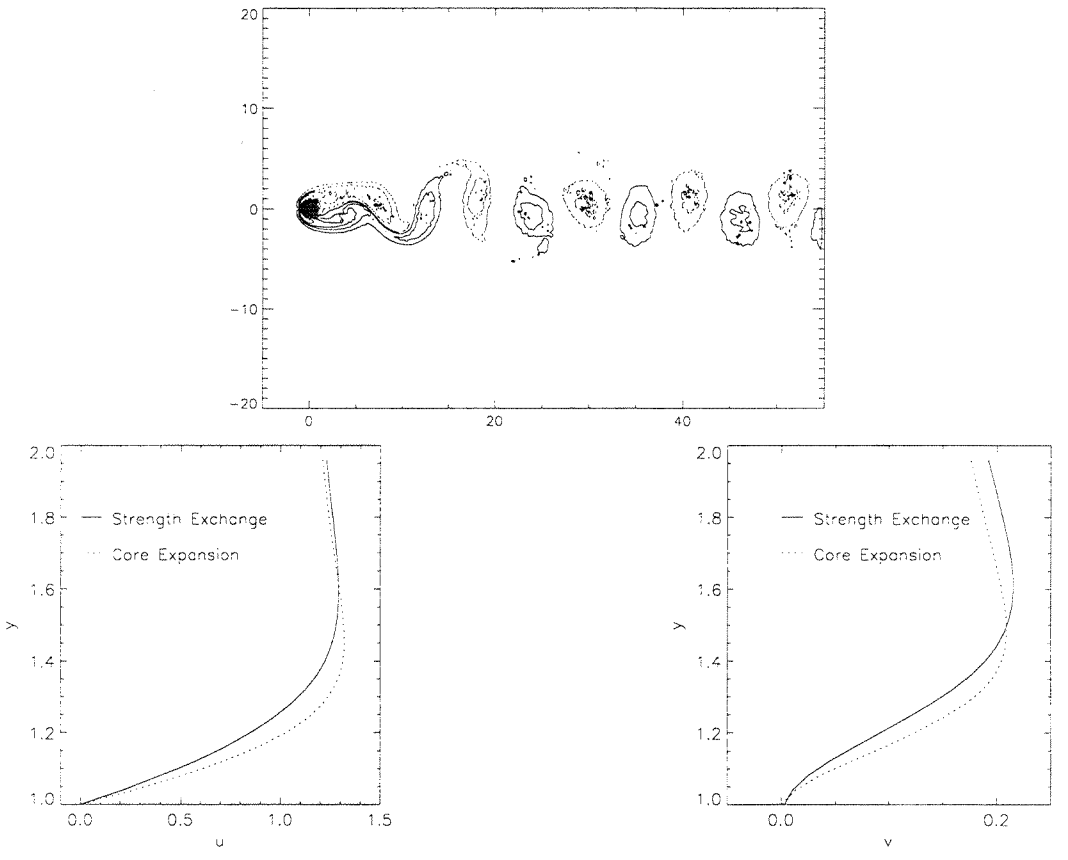


**Figure 34: Core expansion with $K_{res}$=0.5. Vorticity contours (top) and velocity at t=8 with u(left) and v(right) components across the boundary layer at θ=90°.**

Another important term in defining the adaptive spatial resolution is $r_{bl}$. It defines the inner region in which the maximum level of resolution is utilized. The expectation that higher accuracy is achieved with larger values of this term is verified by the results in Figure 36.

Yet another important issue in the adaptive spatial resolution is the choice for C, which defines the finest scale of resolution. As discussed earlier, it must be chosen so that the numerical boundary layer for each time step's vortex sheet flux is accurately transmitted. Yet it cannot be chosen too small or the α of the splitting step will become too small, yielding large splitting error. The effects of increasing to C=4 are evident in Figure 37. Clearly this is less accurate than the use of C=2, though it could be considered acceptable if one wishes to improve the computational efficiency.

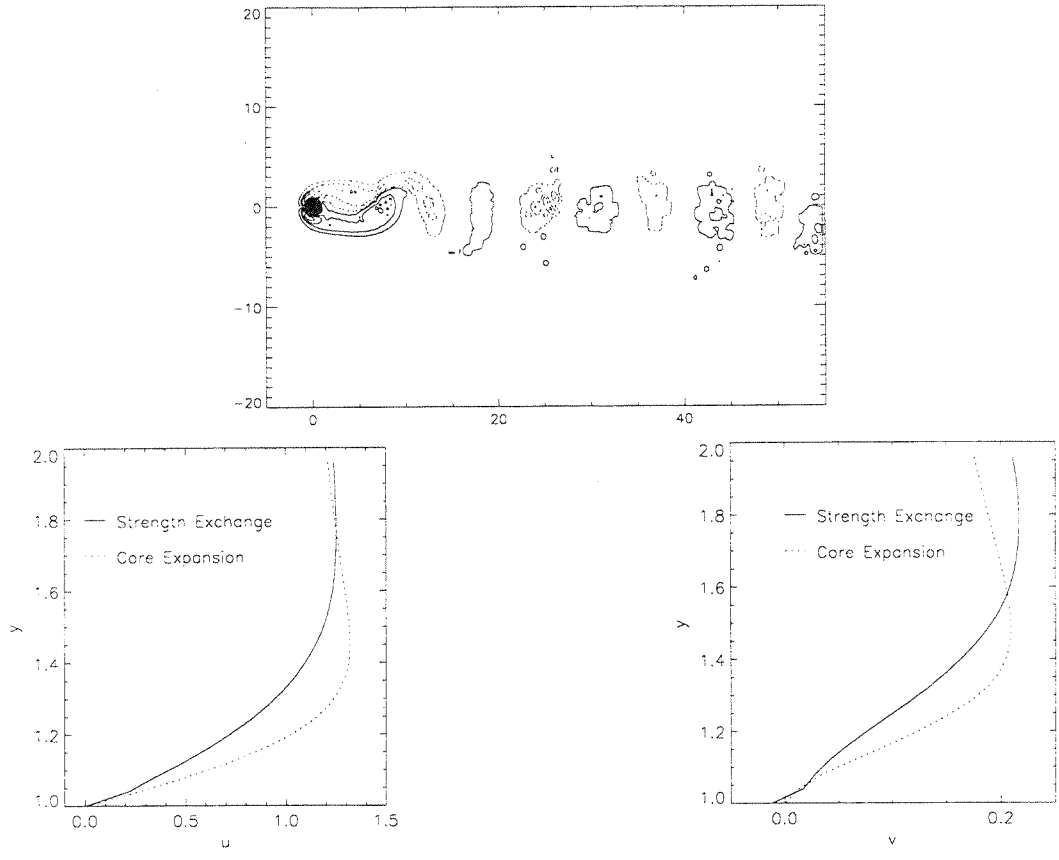


**Figure 35: Core expansion with $K_{res}$=2. Vorticity contours (top) and velocity at t=8 with u(left) and v(right) components across the boundary layer at $\theta$=90°.**

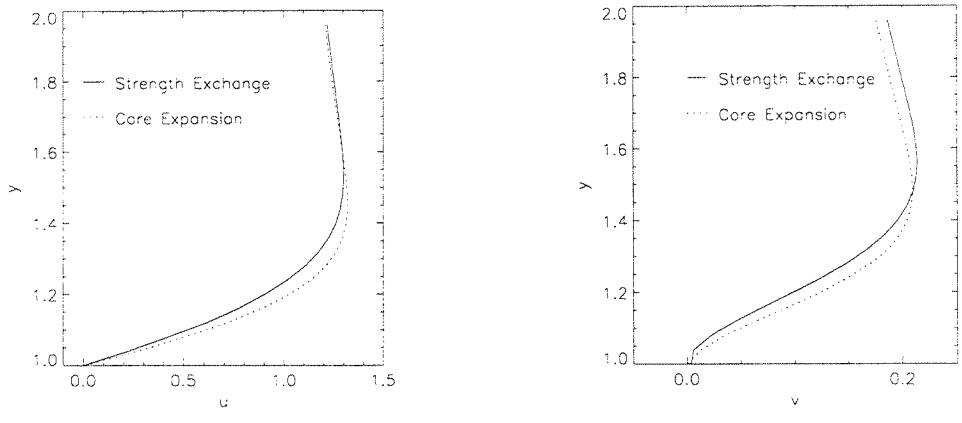


**Figure 36: Velocity profiles (u(left) and v(right) components) along a $\theta$=90° ray through the boundary layer at t=8 for $r_{bl}$=10.**

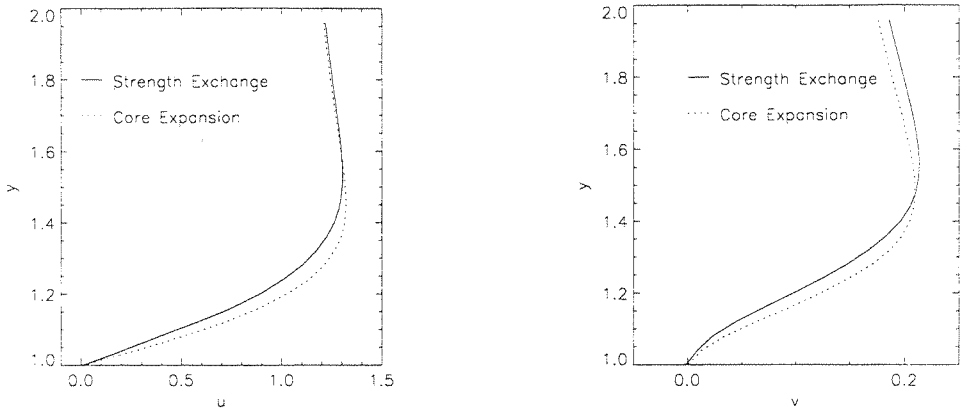


**Figure 37: Velocity profiles (u(left) and v(right) components) along a θ=90° ray through the boundary layer at t=8 for C=4.**

The length of the time step is also important when one wishes to balance accuracy with efficiency. As can be seen in Figure 38 and Figure 39, it is possible to use a more aggressive time step than $\Delta t=0.02$ and obtain reasonable accuracy. In fact, it appears that in this case the use of a more aggressive time step strikes a better balance between accuracy and efficiency than increasing C to reduce the number of particles. It is reasonable to suspect that such behavior reflects the value of properly resolving the numerical boundary layer from the diffusing vortex sheet, which relies upon the choice of C rather than $\Delta t$.

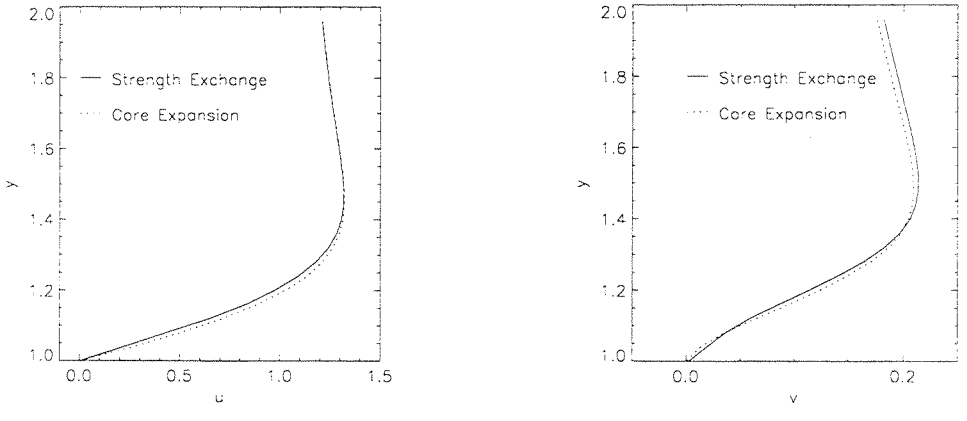


**Figure 38: Velocity profiles (u(left) and v(right) components) along a θ=90° ray through the boundary layer at t=8 for $\Delta t=0.04$.**

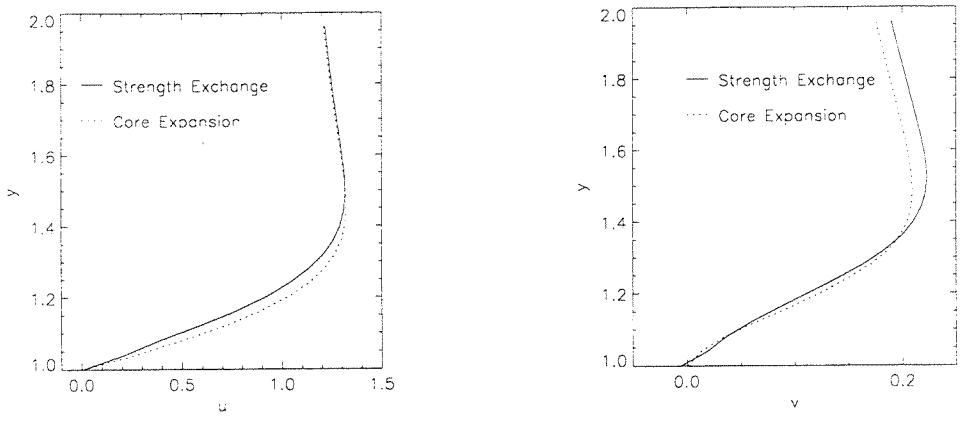


**Figure 39: Velocity profiles (u(left) and v(right) components) along a $\theta=90^{o}$ ray through the boundary layer at t=8 for $\Delta t=0.08$.**

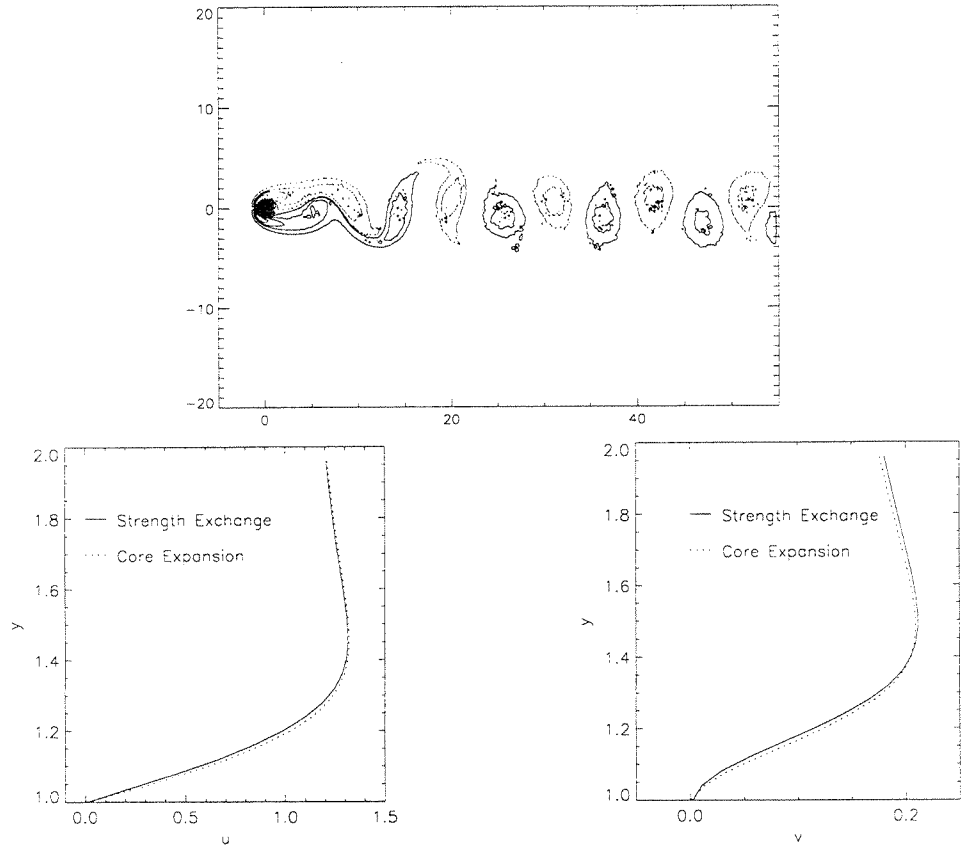


**Figure 40: Core expansion with $N_{fuse}$ =10, $(r^2/\sigma^2)_{max}$=0.5. Vorticity contours (top) and velocity at t=8 with u(left) and v(right) components across the boundary layer at $\theta=90^{o}$.**

Constraints must also be placed on the merger step utilized in these simulations. Two whose influence are considered here are the maximum number of particles allowed to merge into a single new particle, $N_{fuse}$, and the maximum distance a merged particle is allowed to lie from the center of the new particle, $(r^2/\sigma^2)_{max}$ (where r is the distance and $\sigma$ refers to the particle core size). Other Re=100 simulations in this section used $N_{fuse}$ =5 and $(r^2/\sigma^2)_{max}$ =0.25. As revealed in Figure 40 and Figure 41, it is important to keep these parameters limited to minimize error, but perhaps more aggressive values are permissible in order to reduce the overall particle count through more extensive merging.

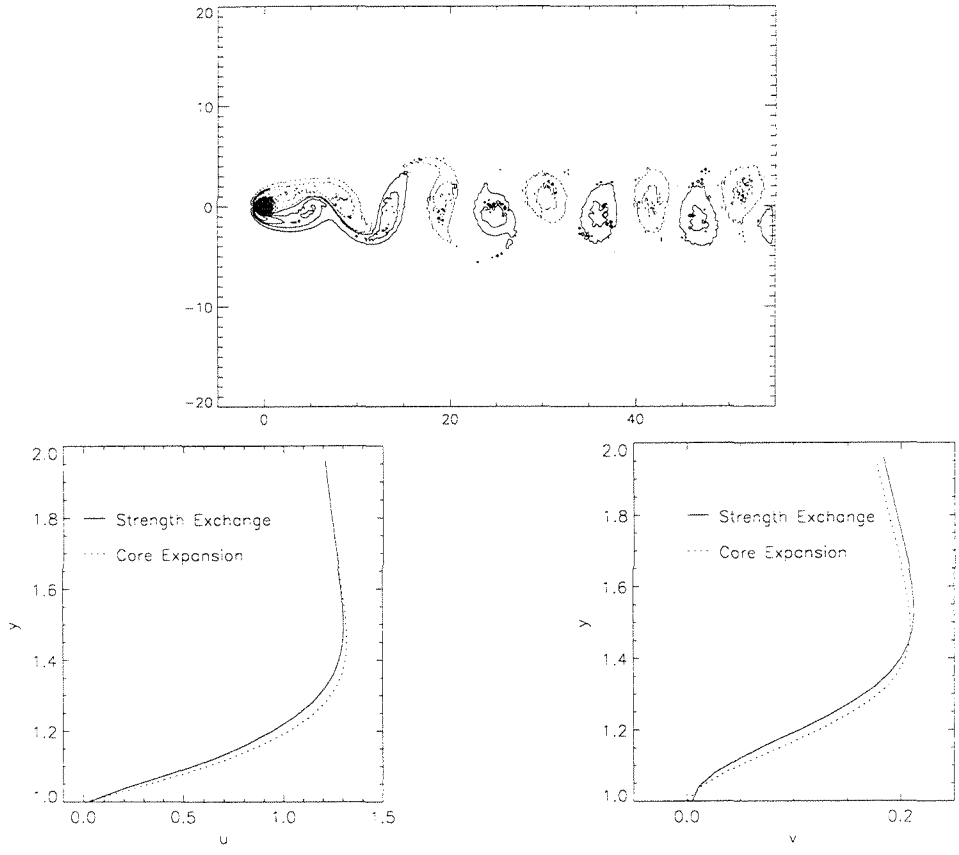


**Figure 41: Core expansion with $N_{fuse}$ =10, $(r^2/\sigma^2)_{max}$=1.0. Vorticity contours (top) and velocity at t=8 with u(left) and v(right) components across the boundary layer at $\theta$=90°.**

A final issue of interest concerns the accuracy of using the more traditional conservation of second moment of vorticity to set the value for the splitting radius r rather than the fit for r=k$\alpha$, especially since the two yield a similar constraint as seen in

Figure 27. The results of a simulation using the second moment constraint on the splitting radius are given in Figure 42 and reveal excessive diffusivity, suppressing vortex formation in the far wake where it is well-known to exist. Such a result is consistent with the fact that the splitting radius given by the second moment constraint is always larger than that set by the $r=k\alpha$ curve fit, leading to extra diffusivity. Note that evidence that a larger value for r (at least in the range of values being explored) yields excessive diffusivity is seen in the above results of the Lamb vortex simulations.

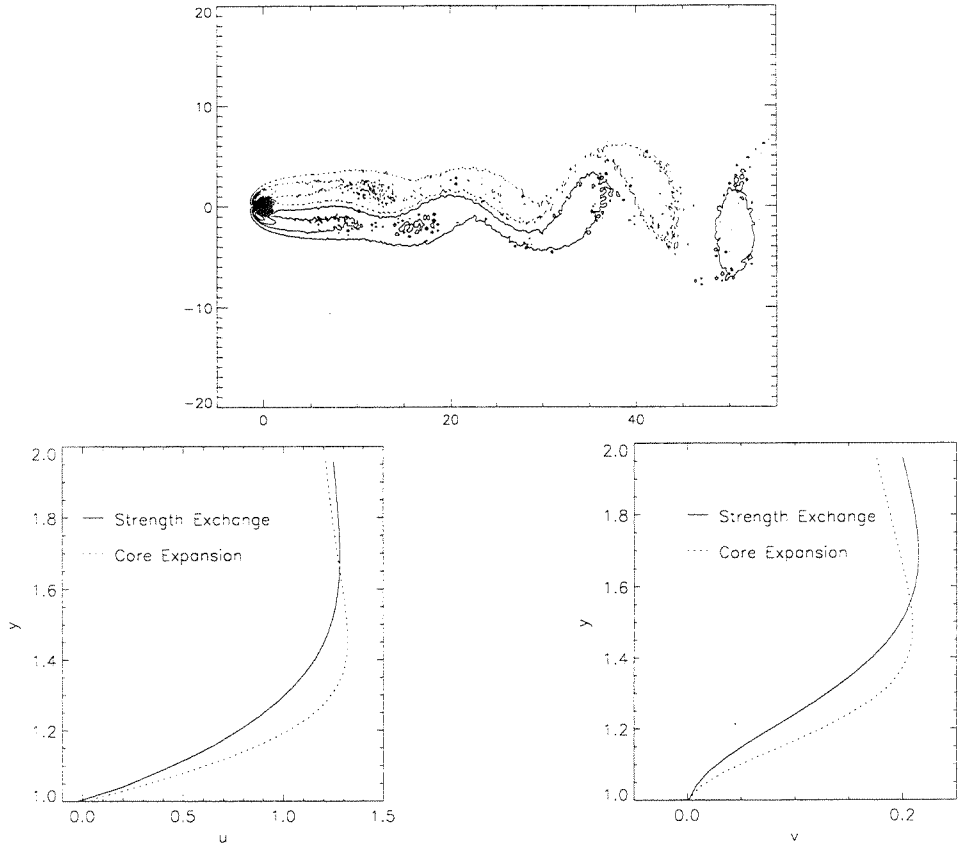


**Figure 42: Core expansion with second moment of vorticity conservation to constrain splitting. Vorticity contours (top) and velocity at t=8 with u(left) and v(right) components across the boundary layer at $\theta=90^{o}$.**

Also of note is the increase in efficiency due to use of the core expansion method. The results given in Figure 33 were obtained from a simulation which required only half the computation time as those in Figure 32 with the PSE method while yielding comparable accuracy. And with the more aggressive particle merging yielding the results

in Figure 40, the simulation ran six times faster than the PSE approach with the drag coefficient and shedding frequency measurements unchanged from the case in Figure 33.

In order to verify that the above parameter determination did not simply tune the flow for a particular set of conditions, similar flows with Re=125-250 are tested while keeping the above parameters constant. These simulations use $\Delta t=0.02$, $\sigma^2=2\nu\Delta t$, $r_{bl}=15$, $K_{res}=0.25$, $N_{fuse}=10$, and $(r^2/\sigma^2)_{max}=0.5$. The resultant shedding frequencies ($S_f=fD/U$) are compared to a curve fit of Henderson's [1996] computational results, which are in good agreement with experimental data (cf. - Hammache et al. [1991]). The present results are found to be in good agreement as seen in Figure 43. Similarly, the drag coefficient averaged over a shedding cycle exhibits behavior comparable to Henderson's [1996] results. The discrepancies present in Figure 44 are exaggerated due to the scale of the plot, but both sets of results clearly exhibit the same Reynolds number trend. Vorticity fields from the simulations once the periodic state has been established display the expected modifications to wake formation as seen in Figure 45 and Figure 46.

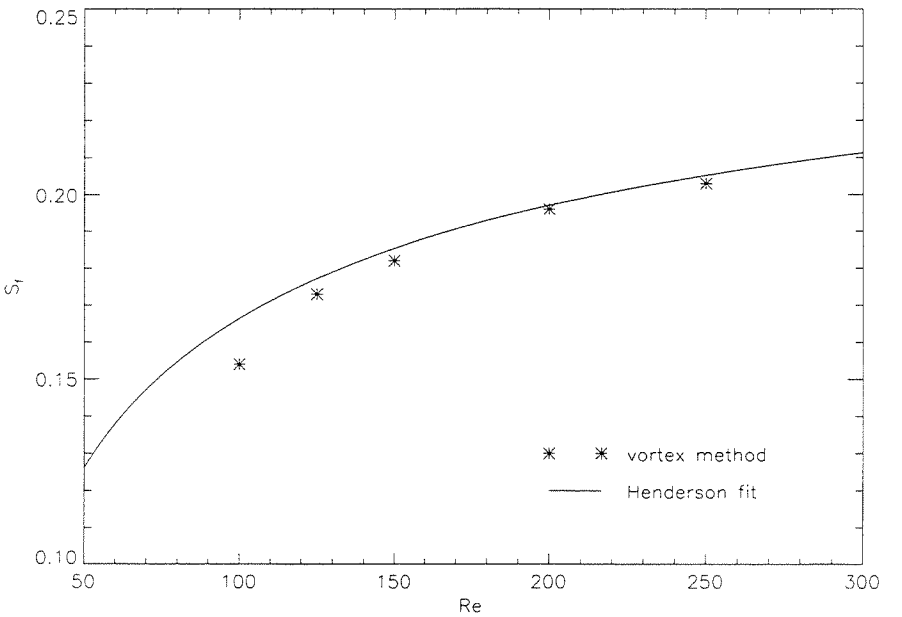


**Figure 43: Shedding frequency versus Reynolds number for core expansion simulations compared with Henderson's [1996] results.**

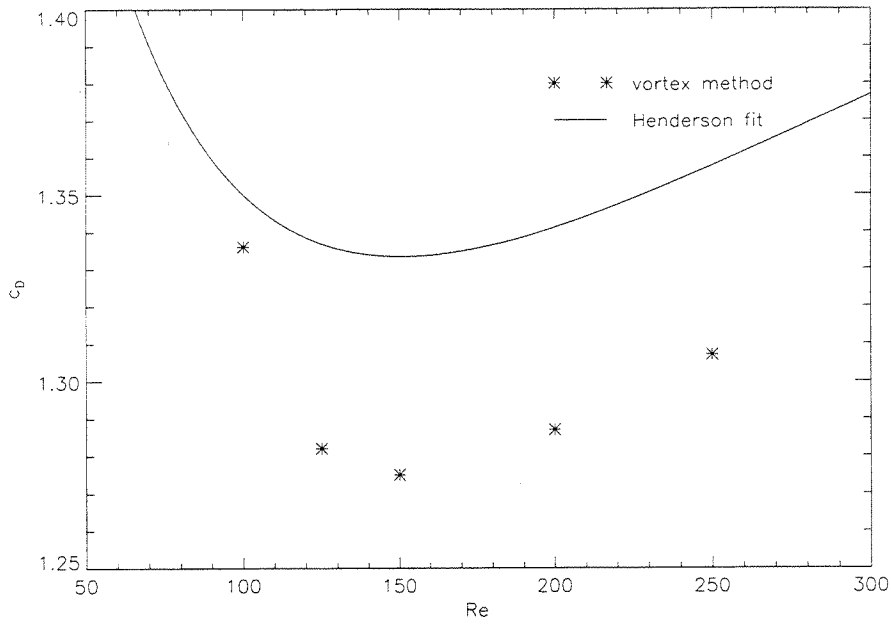


**Figure 44: Drag coefficient versus Reynolds number - core expansion simulations compared to Henderson's [1996] results. Note the narrow scale of the y-axis.**

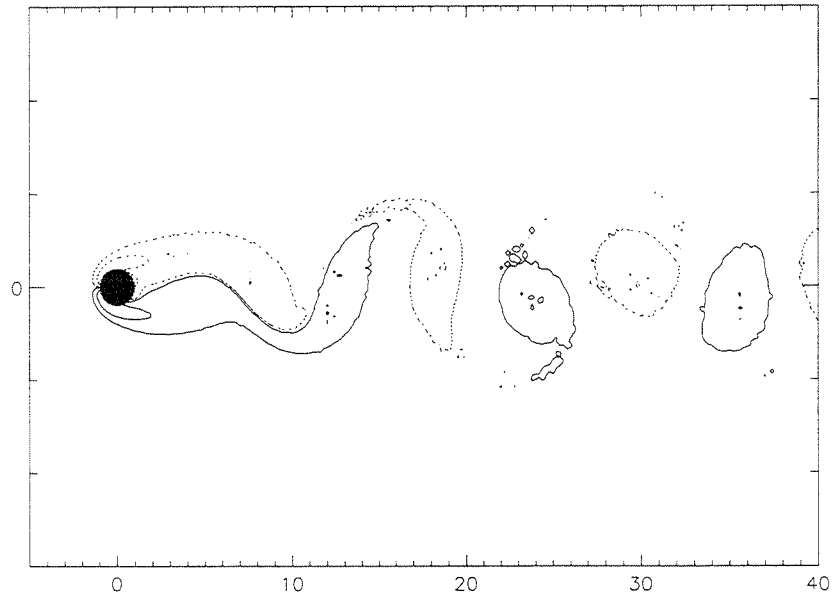


**Figure 45: Vorticity field from a core expansion simulation at Re=100, contours at $\omega = [\pm 0.1, \pm 1.0]$.**

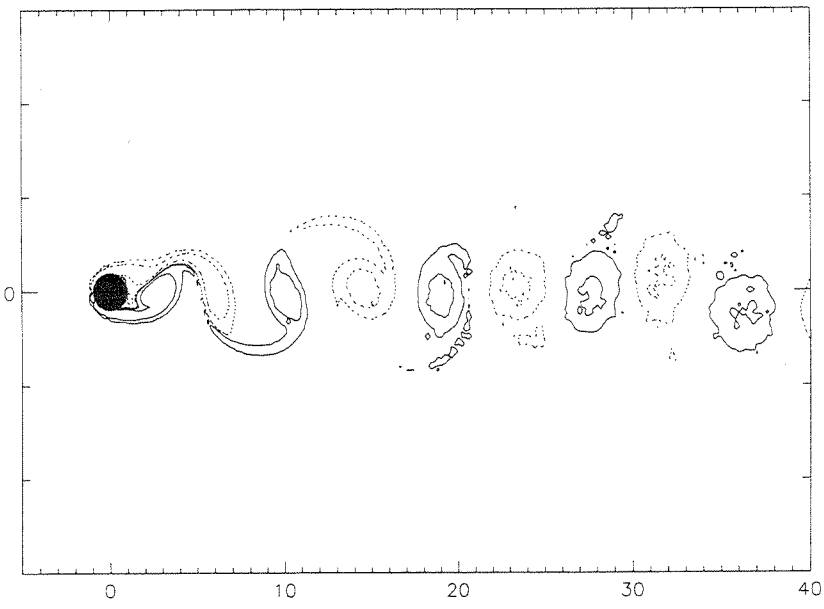


**Figure 46: Vorticity field from a core expansion simulation at Re=250, contours at $\omega$= [±0.1, ±1.0].**

The above low-Re simulations clearly exhibit convergence of the core expansion method and its potential to balance accuracy and efficiency. However, the primary interest in developing vortex methods is for flows at much higher Reynolds number, where gradients in the flow are much sharper and relevant length scales are much finer. Thus, below, the core expansion approach is applied to the early stages of impulsively started Re=3000 flow over a circular cylinder to assess its behavior in more challenging conditions. This flow was used as a benchmark in validating the PSE method above. The drag coefficient results from that benchmark test are used as a standard for these core expansion simulations. Unless otherwise stated, the same parameters are used for these Re=3000 simulations as at Re=100 except more aggressive merging with $N_{fuse}$ =10 and $(r^2/\sigma^2)_{max}$=0. 5 is implemented. Unlike the Re=100 tests, for the Re=3000 cases the cylinder is held rigid the entire simulation from t=0-6.

First the appropriate value for $K_{res}$ is considered (with $\Delta t$=0.02) as this was found to be a fairly sensitive parameter in the Re=100 tests and has much influence over the computational speed. Using the drag coefficient as a diagnostic due to its known sensitivity, it can be seen in Figure 47 that the results converge for a similar value of $K_{res}$ as in the Re=100 case.

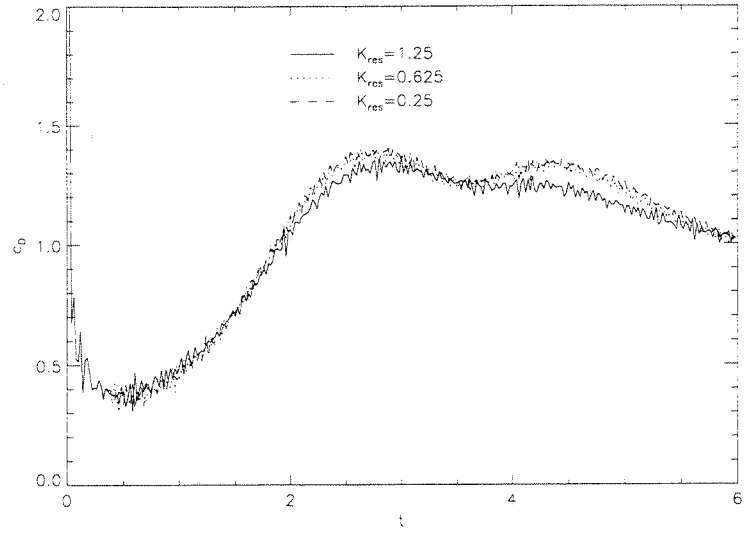


**Figure 47: Drag for impulsively started Re=3000 flow, Δt=0.02, core expansion, various choices for $K_{res}$.**

A comparison to the known benchmark for the drag coefficient (using the PSE method at Δt=0.01) reveals quite a bit of discrepancy. However, as seen in Figure 48, the core expansion result does in fact agree with the PSE result at Δt=0.02, indicating that the differences with the PSE benchmark are simply due to a lack of convergence in time discretization. By t=3, the core expansion simulation at Δt=0.02 executes three times faster than the PSE approach with the same timestep and apparently equivalent accuracy.

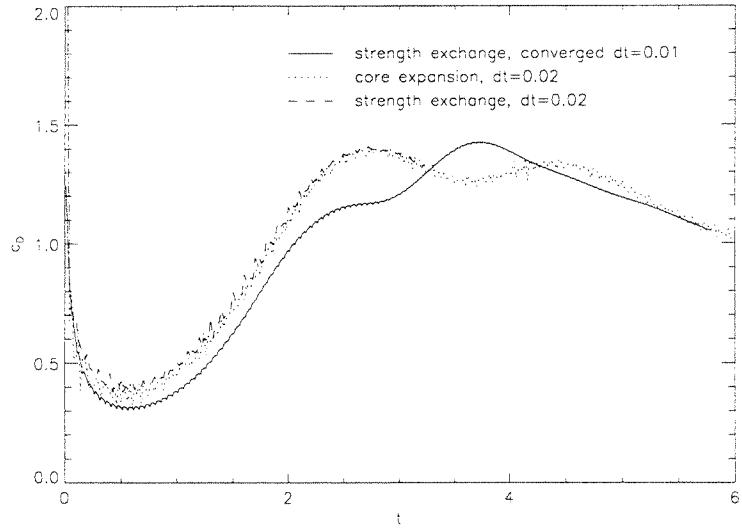


**Figure 48: Drag for impulsively started Re=3000 flow using differing viscous methods.**

However, the core expansion technique does not converge as quickly, when $\Delta t$ is decreased, to the benchmark result as the PSE method. As seen in Figure 49, it is necessary to reduce the timestep to $\Delta t=0.005$ before the core expansion simulation yields a drag acceptably close to the converged PSE result. As shown in Figure 50, refinement of the adaptive spatial resolution parameters was also required (although $K_{res}=5$ was found acceptable). This behavior could be expected as the spatial resolution in the boundary layer is at a finer scale for a smaller timestep based on the $\sigma^2=2\nu\Delta t$ relationship, thus requiring a larger $r_{bl}$ to maintain the finest resolution over the same region of the boundary layer. At t=6 the core expansion simulation with $\Delta t=0.005$ executes three times faster than the converged PSE method. As the wake grows, the core expansion technique gains in efficiency compared to the PSE approach due to its spatial adaptivity, minimizing the particle count.

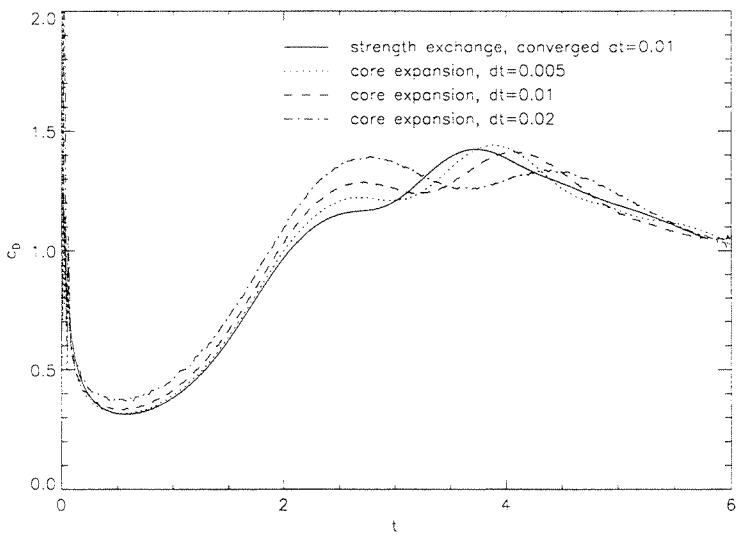


**Figure 49: Drag for impulsively started Re=3000 flow using differing timesteps.**

A final interesting aspect of the Re=3000 starting flow is the extent to which variation in the drag is reflected in the simulated vorticity fields. As seen in Figure 51, the field varies quite noticeably when the drag error is more significant and can be seen converging in concert with the convergence observed in the drag coefficient.

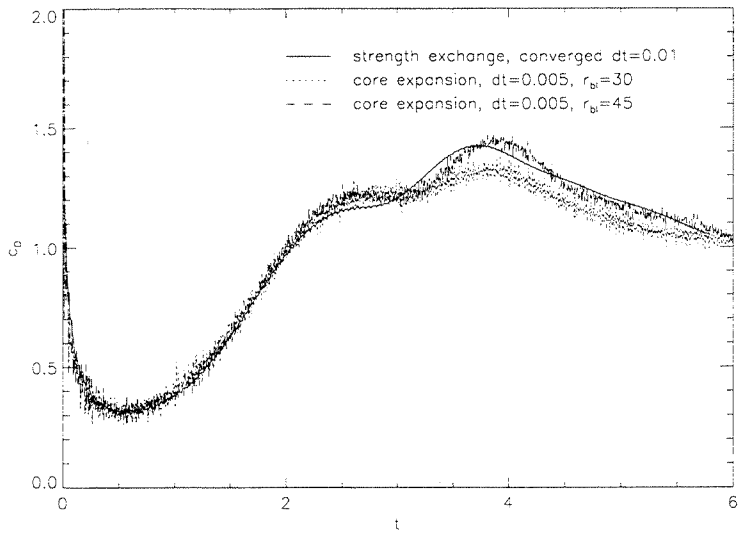


**Figure 50: Drag for impulsively started Re=3000 with variation of $r_{bl}$.**

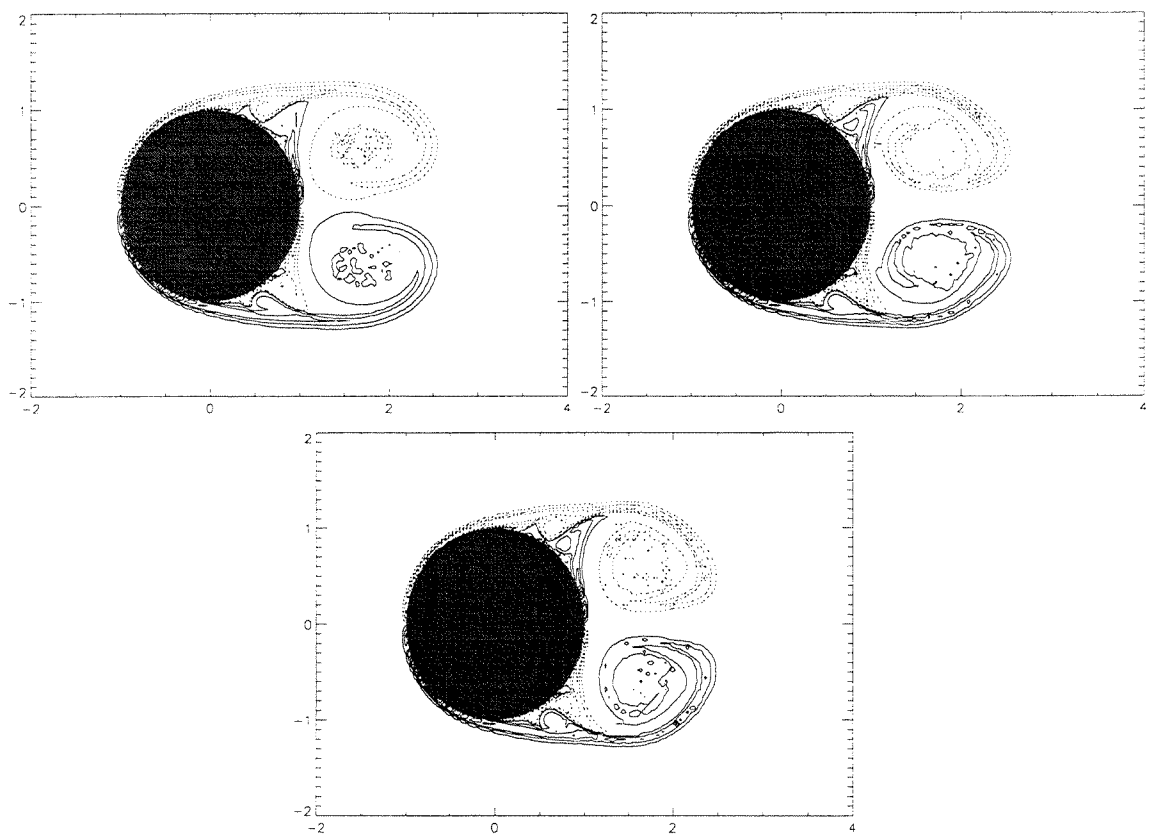

**Figure 51: Vorticity for converged core expansion simulations, Re=3000 starting flow at t=6, Δt=0.02 (top left), Δt=0.01 (top right), and Δt=0.005 (bottom).**

# 3 Elastically Mounted Circular Cylinder

## 3.1 Introduction

There are many practical examples of the use of three-dimensional structures with a circular or otherwise bluff cross section. Members of this class such as cables are subject to unpredictable behavior and failure due to structural oscillation induced by unsteady fluid forces. Thus there is much practical interest in predicting the interaction between the structural and fluid environments impacting these bluff bodies. Such prediction is hindered by the complexity of bluff body flow, compounded by the addition of flexibility in the structure.

A canonical problem in the study of such flow induced vibration is two-dimensional flow over a circular cylinder, where the cylinder is held rigid inline with a constant freestream but considered to be on an elastically damped support in the cross-stream direction.

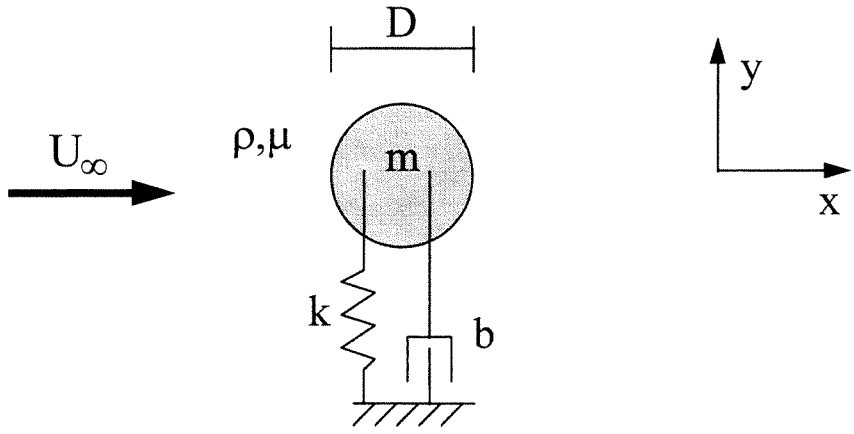


**Figure 52: Layout of canonical flow induced vibration problem.**

The elastic mounting is intended to model the effects of a three-dimensional structure. The motion of the system is governed by an equation of motion in the y-direction

$$m\ddot{y} + b\dot{y} + ky = F_y \tag{3.1}$$

m=cylinder mass, b=damping coefficient, k=spring(elastic) coefficient,

$F_y$=cross-stream (lift) force from the fluid

The complexity of bluff body flow has hindered attempts to express $F_y$ in terms of the body motion and thus obtain an analytical model for the system. As a result, attention has focused on experiments and simulations to deduce models of the system. However, despite a reasonably large body of work in this area, the problem is still largely unsolved due to the large parameter space governing the system and a lack of understanding of how various combinations of these parameters impact the system's response. The computational study presented below explores and clarifies behavior in some limiting regions of the system's parameter space which can help to define a framework for modeling.

There are two approaches to the study of the flow induced vibration problem above, both of which are well-reviewed by Parkinson [1989]. One can investigate forced bluff body motion (i.e., prescribed trajectories for the body) and attempt to use the resultant database to predict the free motion of the actual system. This approach has yielded a wealth of valuable data that helps to guide understanding of these flows. However, the symbiotic relationship between the flow development and body motion renders the elastically mounted system quite complex, making such prediction difficult.

The second approach is to directly study the elastically mounted system, though there are quite a few complications in establishing an experimental investigation of the problem. Until recently, this approach was typified by early findings such as Koopmann [1967] and Feng [1968], in which it was observed that the cylinder response was predicated on a match between the characteristic frequency of the vortex shedding and characteristic frequency of the mechanical system. When the difference between the two frequencies was relatively small, the cylinder vibrated with a significant amplitude at the frequency of the mechanical system (termed 'lock-in'). Outside of this region, the cylinder vibration amplitude is relatively low with the frequency characteristic of the fluid system. Results in Feng's study were scaled against a reduced velocity U where

$$U = \frac{U_\infty}{\omega_n D} \qquad \omega_n = \sqrt{\frac{k}{m}}$$

and a hysteresis was observed in the lock-in region.

Perhaps because Feng's basic results were physically reasonable, a great deal of modeling effort was subsequently undertaken to reproduce a system that exhibited both

lock-in and the hysteresis. Sophisticated techniques were used to base $F_y$ on the cylinder motion y(t) and yet the models still had much difficulty in reproducing the expected behavior.

However, Feng's findings were for a specific set of fluid and structural parameters and recent work suggests they are only representative of part of the parameter space. Gharib et al. [1997] experimentally observed a much wider range of cylinder response than Feng for a system with much smaller mass and damping (in non-dimensional terms, as discussed below) than in Feng's study. Khalak et al. [1996] made similar observations in an independent study. Gharib also observed that the cylinder did not lock-in to the mechanical frequency but followed the characteristic fluid frequency. These observations motivated the computational study below to investigate structural parameters in the limit as they reach zero (m=0,b=0,k=0) to help frame the behavior of this elastically mounted system.

## 3.2 Computational Study

### 3.2.1 Equation of Motion

The dimensional form of the equation of motion (3.1) should be recast into non-dimensional variables to define a parameter space for behavior of the system. Based on the belief that the mechanical frequency governs the system response, traditional non-dimensionalization employs $\omega_n$ and the cylinder length scale (either radius R or diameter D). In this work the cylinder radius R is used for consistency with the other sections. However, in the limiting cases m=0 and k=0, the mechanical frequency is not an appropriate choice and thus in this work the freestream velocity $U_\infty$ is used instead, yielding the non-dimensional equation of motion

$$m^*\ddot{y}^* + b^*\dot{y}^* + k^*y^* = c_L \tag{3.2}$$

$$m^* = \frac{\pi\rho_b}{\rho}, \quad b^* = \frac{b}{\rho U_\infty R}, \quad k^* = \frac{k}{\rho U_\infty{}^2}, \quad c_L = \frac{F_y}{\rho U_\infty{}^2 R}, \quad \rho_b = \text{body density / length}$$

An alternate form of (3.2) proves useful to assist in analyzing the system behavior. The lift coefficient $c_L$ can be decomposed into a term related to the acceleration of the body and a remainder that will be called the wake lift coefficient $c_{LW}$

$$c_L = -m_A \ddot{y}^* + c_{LW} \tag{3.3}$$

The term $m_A$ is the apparent mass which can be derived from potential flow theory (i.e., giving the force on a body accelerating in a potential flow). For an accelerating cylinder, the apparent mass is given by $m_A = \pi$. Thus the lift has been decomposed into what could be considered an inviscid term and a remaining term to represent the viscous effects as characterized by the wake. An alternative form of the non-dimensional equation of motion is thus

$$\left(m^* + \pi\right)\ddot{y}^* + b^*\dot{y}^* + k^* y^* = c_{LW} \tag{3.4}$$

Either (3.2) or (3.4) can thus be used in conjunction with a computational method to simulate the behavior of the system. The flow simulation will provide the lift forces on the right side of the equations and the trajectory of the body is updated between timesteps based on the equation of motion.

### 3.2.2 Computational Method

The particle strength exchange (PSE) vortex method discussed in Chapter 2 is used for simulations of the system in Re=100 flow. It was shown that the PSE approach is highly reliable for such conditions and the inclusion of the inviscid far-wake scheme facilitates computations of enough duration to determine the long-term behavior of the system. The lift coefficient can be obtained, as detailed in Appendix A, based on the relation

$$c_{Lb} = -\frac{2}{Re}\int_0^{2\pi}\left(\frac{\partial \omega^*}{\partial r} - \omega^*\right)\cos(\theta)d\theta \tag{3.6}$$

where the integral is evaluated on the body surface.

The discretization of the equation of motion (3.2) requires special care with a vortex method due to the indirect impact of body acceleration on the lift force. The simulation is configured to impose a freestream in y (in addition to the freestream in x) instead of motion of the body within the coordinate system of the computation. The

vorticity equation is invariant to the choice between a body-fixed and inertially-fixed frame of reference when an irrotational motion such as this is involved. However, force computation is sensitive to an accelerating reference frame. As a result, the lift in an inertially-fixed frame differs from the lift measured in a body-fixed frame. In the current computations, we measure the lift in a body-fixed frame $c_{Lb}$, which is related to the inertial-frame lift $c_L$ by

$$c_L = c_{Lb} + \pi\ddot{y} \tag{3.7}$$

However, a further complication arises because the acceleration of the freestream (in the body-fixed frame) contributes a factor to the lift identical to the apparent mass lift for a body in an inviscid accelerating freestream ($c_L = 2\pi\ddot{U}_{y\infty}$). The terms are the same because this effect is manifested by a vortex sheet (which also exists in the inviscid flow), thus going undetected in the particle vorticity field. Numerically, the diffused vortex sheet from the previous timestep will cause the acceleration from that timestep (t=0) to be reflected in the measured lift $c_{Lb}(t=\Delta t)$. Thus, the lift needs to be modified to account for the adjustment to the body's acceleration over a timestep. So, for the current computational technique, the measured lift $c_{Lb}$ must be modified to obtain the lift $c_L$ in (3.2) as follows:

$$c_L(t) = c_{Lb}(t) + 2\pi\left(\ddot{y}^*(t-\Delta t) - \ddot{y}^*(t)\right) + \pi\ddot{y}^*(t) = c_{Lb}(t) + 2\pi\ddot{y}^*(t-\Delta t) - \pi\ddot{y}^*(t) \tag{3.8}$$

Basically, (3.8) decomposes the lift in (3.2) into the terms known explicitly and those which are implicit in the solution of the equation of motion. The equation of motion (3.2) can thus be updated at the end of a timestep by

$$\ddot{y}^*(t) = \frac{1}{m^* + \pi}\left[c_{Lb}(t) + 2\pi\ddot{y}^*(t-\Delta t) - b^*\dot{y}^*(t') - k^*y^*(t')\right] \tag{3.9}$$

where the damping and elastic terms require an approximation for the body velocity and position at time t, designated thus as time t'. These approximations can be obtained using the known body acceleration at earlier times.

To validate the computational method, simulations were run in comparison to the free vibration simulations of Blackburn et al. [1996] for an elastically mounted cylinder

at Re=250, $m^*=40$, $b^*=1.6\pi f_n^*$, and $k^*=320\pi^2 f_n^{*2}$ in a lock-in region (where $f_n^*=2\pi\omega_n^*$ and $f^*=fR/U_\infty$). These simulations included elastic motion both transverse to and in-line with the freestream, requiring an equation of motion similar to (3.2) for the in-line direction. A classical lock-in can be observed for these parameters, as seen in the comparison plotted in Figure 53. In this plot, the results are fitted as well as possible to $y^*=A^*\sin(2\pi f^* t^*)$, using diameter rather than radius for non-dimensionalization. The lift values and amplitudes in the plot are rms-averages while the drag values are simply time averaged. The frequency and forces are normalized by values for a fixed cylinder in two-dimensional Re=250 flow.

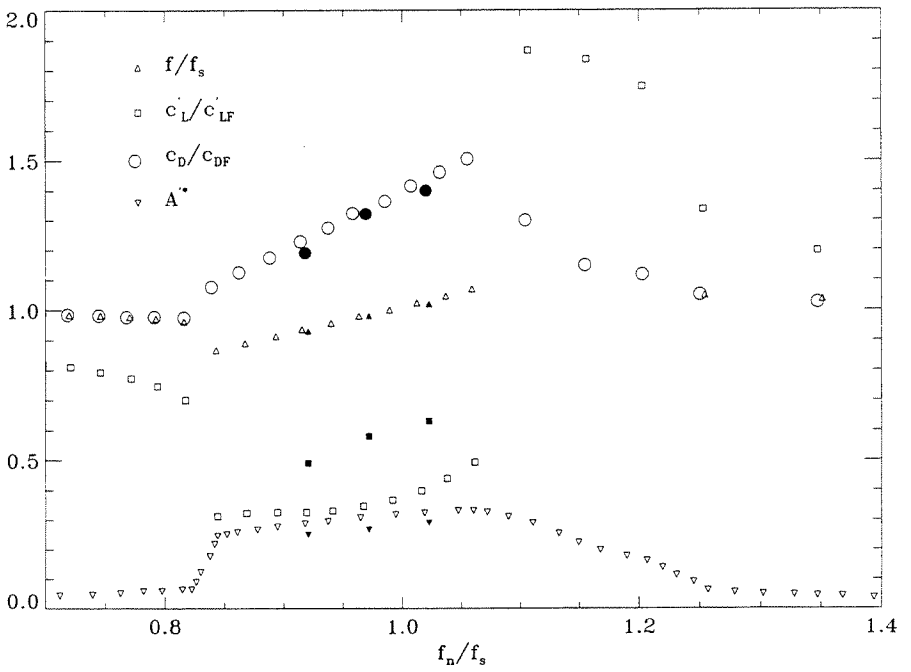


**Figure 53: Comparison of the PSE method (solid symbols) with results from Blackburn et al. [1996] (hollow symbols).**

Comparison was made only in the lock-in region for a simple validation of the PSE vortex method implemented on free vibration problems. The comparison is reasonably good as the lock-in behavior is clearly detected. The differences in lift coefficient and amplitude may be attributable to the shorter time of simulation in this study (50 diameters of streamwise motion) as opposed to the Blackburn investigation

(300 diameters). The vortex method results are in fact gradually moving toward those of the prior investigation at the conclusion of the simulations.

The simulations below are all elastic in the transverse direction only, governed by (3.2). The PSE approach is augmented with the inviscid far wake merging, beginning six diameters downstream. All simulations are at Re=100, using a timestep $\Delta t=0.02$, spatial resolution based on $\sigma^2=2\nu\Delta t$ and particle spacing $h\sim\sigma$, and remeshing of the particle field every 5 timesteps. The cylinder radius is taken as R=1 and freestream of $U_\infty = 1$ is used. As discussed in Chapter 2, an asymmetry is produced in the field by rotating the body over the first four diameters of downstream motion according to $\Omega=\sin(0.25\pi t^*)$ while holding it rigid transversely. Beyond $t^*=8$, the cylinder is not rotated but allowed to respond transversely to lift forces and the elastic support.

### 3.2.3 Limiting Case: $m^*=0$, $b^*=0$, $k^*=0$

The most extreme limit on the mechanical system is to essentially remove all of it, leaving only the requirement that the surface of the massless cylinder must remain solid. Setting $m^*=0$, $b^*=0$, and $k^*=0$ leaves the cylinder free to move in the plane x=0 solely under the influence of forces which are induced by unsteady vorticity, without mechanical or inertial forces. The motion of the cylinder in this situation is defined by balancing the apparent mass force due to acceleration with the measured influence of the wake.

Beyond the initial forcing, the cylinder quickly reaches a periodic state in which it oscillates with an amplitude of nearly one radius. Figure 55 indicates how quickly the periodic state is reached and that a single frequency ($f^*=0.078$) dominates the response. A third-harmonic is also present, though nearly undetectable. It is notable that the response frequency is very close to the shedding frequency for a fixed cylinder, $f_{fixed}^*\sim0.083$ (note that radius R is used for non-dimensionalization rather than the diameter D). In fact, the vorticity field established in the wake in Figure 54 is quite similar to the shedding pattern of a fixed cylinder.

Thus, without mechanical properties to influence response, the cylinder seems strongly drawn to a state defined by the natural characteristics of the wake. The wake is

compliant enough to produce a periodic state fairly similar to its natural state yet with differences to support the motion of the cylinder.

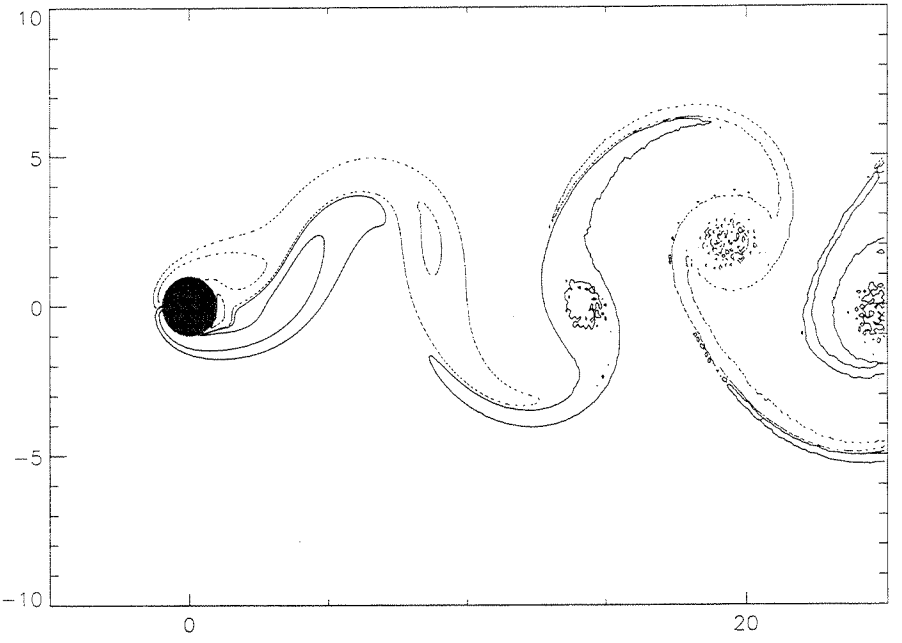


**Figure 54: Vorticity field for $m^*=0$, $b^*=0$, $k^*=0$ at minimum $y^*$ ($t^*=98.7$) with contours $\omega^*=\pm0.1, \pm1.0$.**

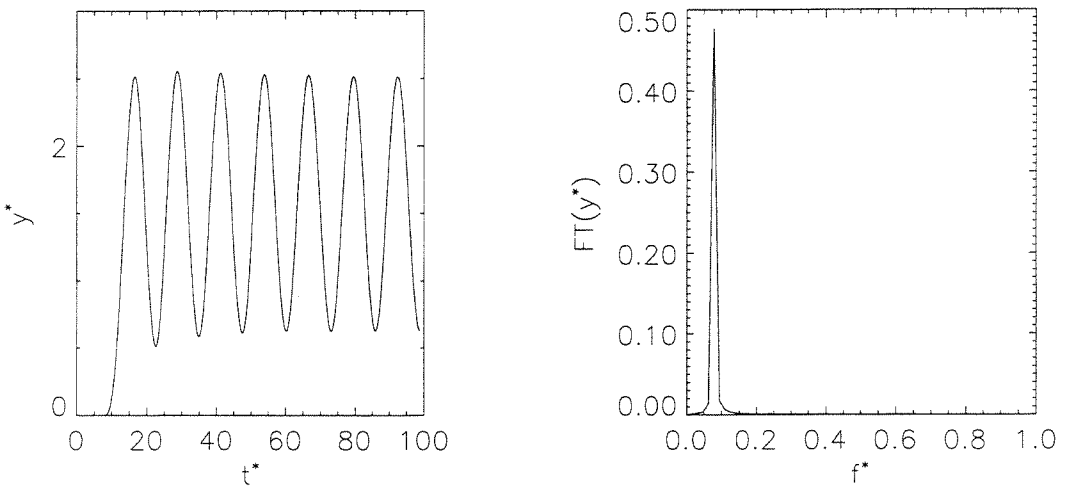


**Figure 55: Transverse motion $y^*$ (left) and the frequency spectrum of the motion (right) sampled from $t^*=34.9$-$98.7$ (5 cycles of periodic motion).**

### 3.2.4 Purely Elastic Support: $m^*=0$, $b^*=0$, $k^* \neq 0$

The system response in the absence of mechanical influences raises questions about the transition between that limiting state and classical lock-in behavior. To begin exploring this issue, supports are considered in which only the elastic resistive force is included. As there is no mass $m^*$, there is still no definable mechanical frequency, though if the apparent mass is considered as a physical mass, then a natural frequency of $\omega_n{}^* = \sqrt{\frac{k^*}{\pi}}$ is suggested. Simulation was possible only for $k^*>0$ as negative $k^*$ led to unstable cylinder response.

Sweeping over a range up to $k^*=8$ revealed a sizeable region in which the cylinder exhibited a large-amplitude, periodic response, similar to the case in 3.2.3. This behavior extended from $k^*=0$ to $k^* \approx 1.5$. In this range, the response can be well defined by

$$y^* = A^* \sin(2\pi f^* t^*) \qquad \text{where } A^* = \frac{A}{R} \tag{3.10}$$

Beyond this up to $k^* \approx 2.5$, there was a similar primary frequency to the cylinder response but amplitude modulation occurred as competing response frequencies became apparent as in the example in Figure 56. For larger $k^*$, the response again became sinusoidal but with a greatly diminished amplitude.

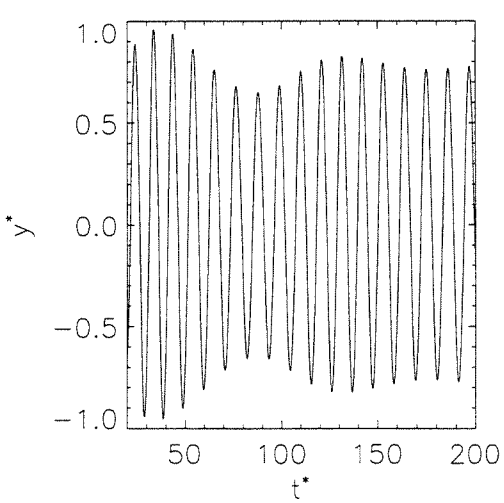


**Figure 56: Cylinder response amplitutue for a simulation of the system $m^*=0$, $b^*=0$, $k^*=2$.**

As seen in Figure 57, the amplitude and frequency of the response increase in the region $k^*<1.5$. The response is nearly a pure sinusoid as in the $k^*=0$ case. Unsurprisingly, the drag also increases in this region. The large increase in the maximum lift from 0 to 2 is interesting in light of the fact that the cylinder motion is relatively constant as measured by the amplitude and frequency. At $k^*=0.707$, the wake pictured in Figure 58 yields a fluctuating lift with amplitude 0.9 for a nearly sinusoidal motion defined by $A^*=1.18$ and $f^*=0.097$. At $k^*=1.414$, a similar nearly sinusoidal motion results with $A^*=1.14$ and $f^*=0.094$, yet the wake, as shown in Figure 59, generates a lift amplitude of 1.7. The topology of the wake in these cases does differ somewhat from the $k^*=0$ case, but still reveals a capacity in the fluid system to supply a broad range of lift while maintaining a fairly classical shedding pattern.

The behavior observed for $k^*<1.5$ stands contrary to the notion that such a synchronized state can only occur for the system near the lock-in conditions (i.e., where the mechanical frequency lies close to the natural shedding frequency) as such conditions do not exist for a massless body. Nor can a mechanical frequency be defined with the apparent mass to reveal lock-in as the response frequency remains relatively constant over a broad range of $k^*$.

As $k^*$ increases beyond 1.5, the cylinder response begins to become modulated rather than exhibiting a dominant frequency. Maximum values in the modulated responses are used in Figure 57 as well as the primary frequency. However, simulations were only taken for 50-60 diameters of downstream motion, which often provided an incomplete view of the system response for these more complex motions. This perhaps explains why data in the $1.5< k^*<2.5$ region seem to deviate from trends in the frequency and drag. This region behaves similarly to the 'upper branch' behavior observed in past flow induced vibration studies (e.g., Khalak et al. [1996]) and data in the $k^*<1.5$ region similarly resembles 'lower branch' behavior. Past studies found significantly higher amplitudes on the 'upper branch' than on the 'lower branch' and a discontinuous jump between the two but such behavior was not observed in the current results. The lack of a higher-amplitude region on the 'upper branch' in this study might be attributable to either the relatively low Reynolds number, insufficient simulation length, or lack of an appropriate trigger.

As $k^*$ becomes large, the parameters in Figure 57 can be seen decaying towards a fixed cylinder state ($A^*=0$). The drag can be seen asymptoting towards the fixed cylinder average of $c_D \approx 1.33$ and similarly the lift amplitude dropping off towards $c_L \sim 0.3$.

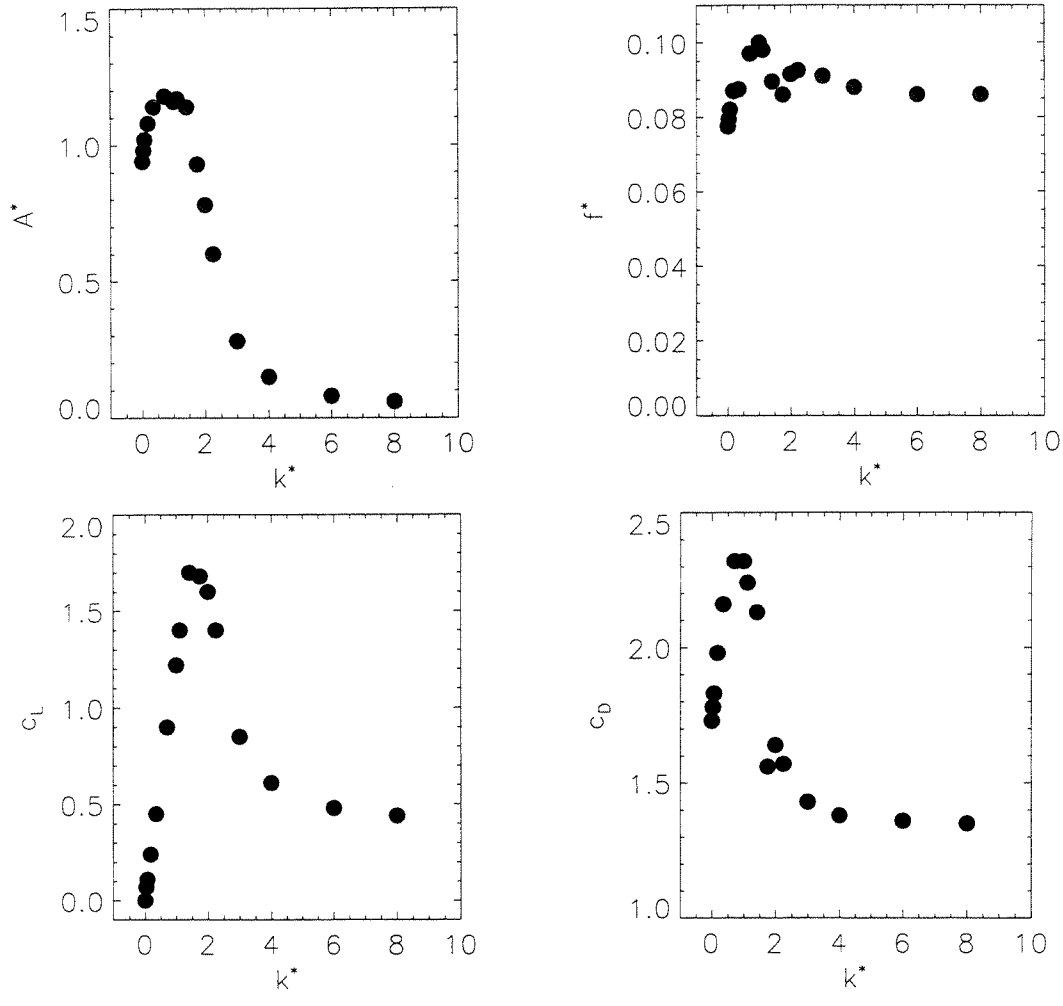


**Figure 57: Response for simlations with $m^*=0$, $b^*=0$, $k^* \neq 0$; pictured are amplitude (upper left), frequency (upper right), lift (lower left), and drag (lower right). Lift is the maximum amplitude of the lift coefficient while drag is an average over a response cycle.**

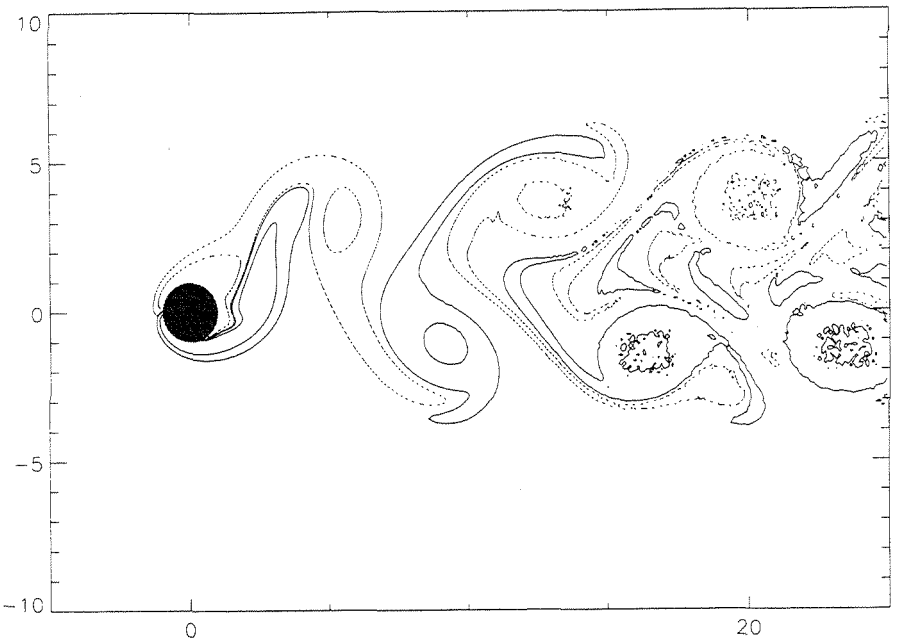


**Figure 58: Vorticity field for $m^*=0$, $b^*=0$, $k^*=0.707$ at minimum $y^*$ ($t^*=112.7$) with contours $\omega^*=\pm0.1, \pm1.0$.**

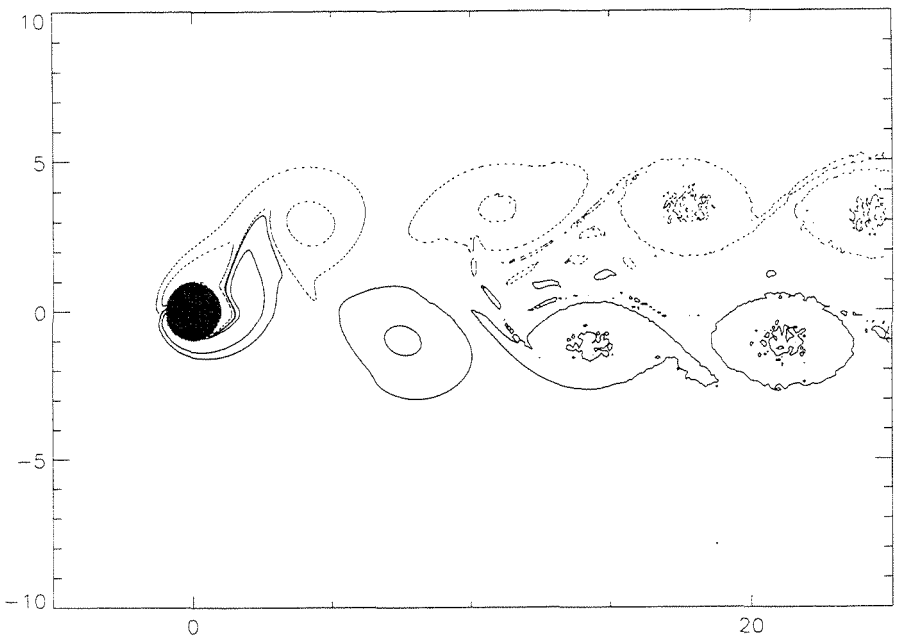


**Figure 59: Vorticity field for $m^*=0$, $b^*=0$, $k^*=1.414$ *at minimum* $y^*$ ($t^*=111.0$) *with* contours $\omega^*=\pm0.1, \pm1.0$.**

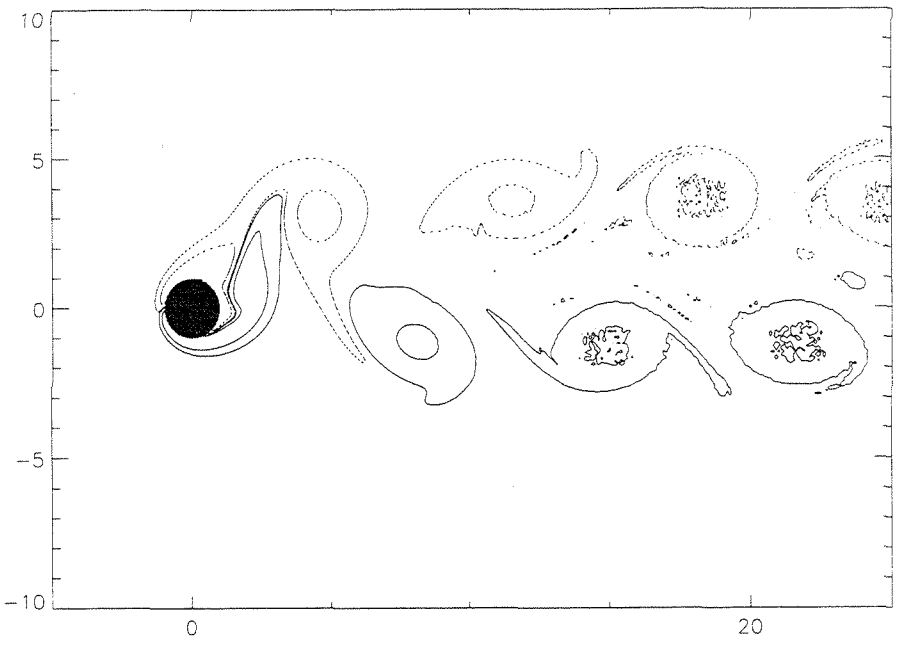


**Figure 60: Vorticity field for $m^*=0$, $b^*=0$, $k^*=1.155$ at minimum $y^*$ ($t^*=110.5$) with contours $\omega^*=\pm 0.1, \pm 1.0$.**

A final issue of note concerns the results for the simulation with $k^*=1.155$. In this case, the lift was solely composed of the apparent mass contribution, leaving $c_{LW}=0$. In other words, the lift in this case was identical to the lift for a cylinder in potential flow following the same trajectory. Figure 60 clearly shows, though, that a typical wake develops in this flow. It is quite a peculiar wake since it essentially makes no contribution to the measured lift at any time once the flow reaches this periodic state although it still generates drag. At this particular value of $k^*$, the response frequency is exactly that defined by the mechanical system if the apparent mass is used for as the body mass

$$f^*\left(k^* = 1.155\right) \approx \frac{1}{2\pi}\sqrt{\frac{k^*}{m_A(=\pi)}} \tag{3.11}$$

The existence of such a state could have been predicted based on the re-cast equation of motion (3.4) and is discussed below.

### 3.2.5 Mass Effects: $m^* \neq 0$, $b^*=0$, $k^* \neq 0$

Based on the observation that nearly pure sinusoidal motion occurred for $m^*=0$, it is possible to predict the effects of including mass by assuming a sinusoidal response. If pure sinusoidal motion is assumed, (3.2) with no damping ($b^*=0$) becomes

$$\left(k^* - 4\pi^2 f^{*2} m^*\right) A^* = \left|c_L\right|_{max} \tag{3.13}$$

Define a new term called the effective elasticity as

$$k_{eff}{}^* = \left(k^* - 4\pi^2 f^{*2} m^*\right) \tag{3.14}$$

The principle behind lock-in is that a resonant response can be expected at $k_{eff}{}^*=0$, due to (3.13). The massless tests above show that a resonant-like response can occur over a range of parameters off lock-in (i.e., $k_{eff}{}^* \neq 0$). If the apparent mass is incorporated into (3.14) to give

$$\left(k^* - 4\pi^2 f^{*2} (m^* + \pi)\right) A^* = \left|c_{LW}\right|_{max} \tag{3.15}$$

a resonance could still be expected in a massless case at $f^*=\frac{1}{2\pi}\sqrt{\frac{k^*}{\pi}}$. But as observed above, at this point instead $c_{LW}$ disappears instead. Thus the tests for $m^*=0$ stand in opposition to the viewpoint that the system should exhibit a lock-in response due to resonance and require a new means of characterization.

Note that for any choices ($k^*$,$m^*$) which keep $k_{eff}{}^*$ constant, a single response is consistent with the governing equation of motion. Thus, the influence of $k^*$ and $m^*$ can be folded into the single parameter $k_{eff}{}^*$, which expresses the fact that for pure sinusoidal motion, the inertia of the body essentially acts in opposition to the resistive elastic force. The inertia can thus be considered to modify the effective elastic coefficient.

This effective elastic coefficient $k_{eff}{}^*$ provides an ideal scaling for system behavior dominated by a single frequency. Traditionally, the reduced velocity U has been invoked for scaling due to the perceived reliance of the system response on the natural mechanical frequency. However, the reduced velocity is undefined for cases where the elasticity or inertia are zero. It is not clear a priori how well scaling with $k_{eff}{}^*$ will define behavior in the regions with multiple significant frequencies (such as $1.5<k^*<2.5$ in the tests of section 3.2.4).

In order to assess the new idea of scaling by $k_{eff}^*$, simulations were run with a non-zero body mass as well as non-zero elasticity but still with no damping. These results are compared with those found for the zero inertia case (in 3.2.4) in Figure 61 and Figure 62. Various choices are used for $m^*$, up to a maximum of nearly $m^*=15$ at which point the body is over 40 times as dense as the surrounding fluid. The results show that $k_{eff}^*$ does in fact collapse the two parameters, $m^*$ and $k^*$, into one effective parameter which properly scales the undamped system. Note that the new scaling works well even in the region of frequency competition. In fact, the inclusion of inertial force in the equation of motion had a tendency to encourage frequency competition in the responses.

It was also possible to find the behavior for $k_{eff}^*<0$, showing that the response quickly drops off and eventually asymptotes towards the fixed cylinder values. Thus a picture is formed of the complete behavior of the undamped system at Re=100, with a region in which the wake and mechanical system can synchronize to establish a large-amplitude, periodic response. Outside of this region, significant motion of the body does not appear possible which would generate a wake whose lift could sustain the motion. The presence of the response frequency $f^*$ in the scaling $k_{eff}^*$ is not desirable for use of these results as a predictive tool. However, knowing the results in Figure 61 a priori, it appears that it would be possible to accurately predict the vortex induced oscillation characteristics of any undamped system at Re=100.

Although the traditional reduced velocity scaling is not defined for many of the cases exhibited in Figure 61 and Figure 62, a modified reduced velocity can be proposed which includes the apparent mass with the body mass in order to define a natural mechanical frequency, thus yielding

$$U_{am} = \frac{U_\infty}{D\omega_{n,am}^*} \qquad \text{where } \omega_{n,am}^* = \sqrt{\frac{k^*}{(m^* + \pi)}} \tag{3.16}$$

The results of scaling based on this parameter are provided in Figure 63 and Figure 64. Clearly, the scaling does not define the behavior well, as multiple responses are possible for a given value of the reduced velocity. Note also that even for this modified scaling, the cases simulated with $k^*=0$ are still not defined.

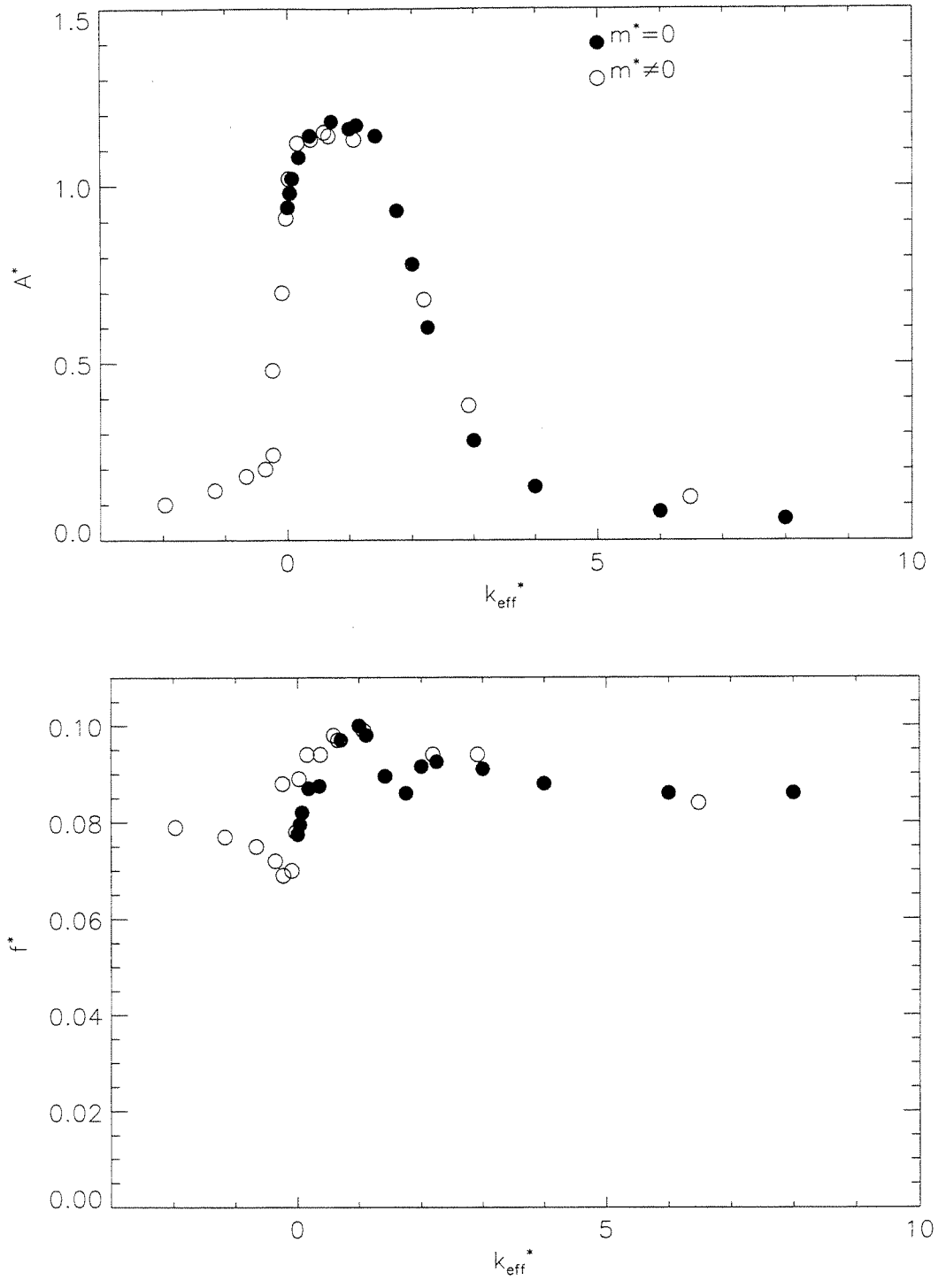


**Figure 61: Amplitude (top) and frequency (bottom) response for undamped systems with and without body inertia, plotted against the effective elasticity.**

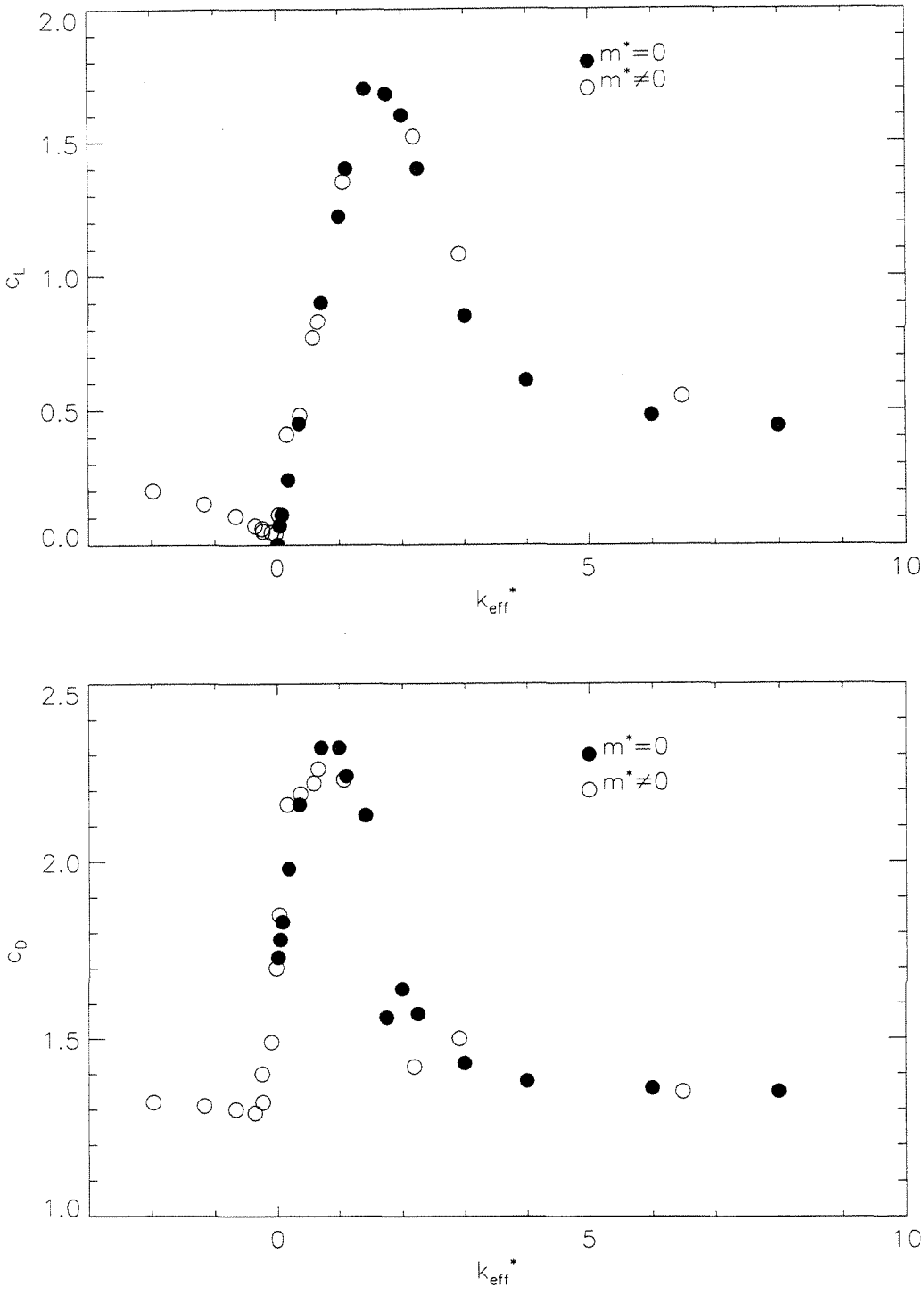


**Figure 62: Maximum lift magnitude (top) and average drag (bottom) for undamped systems with and without body inertia, plotted against the effective elasticity.**

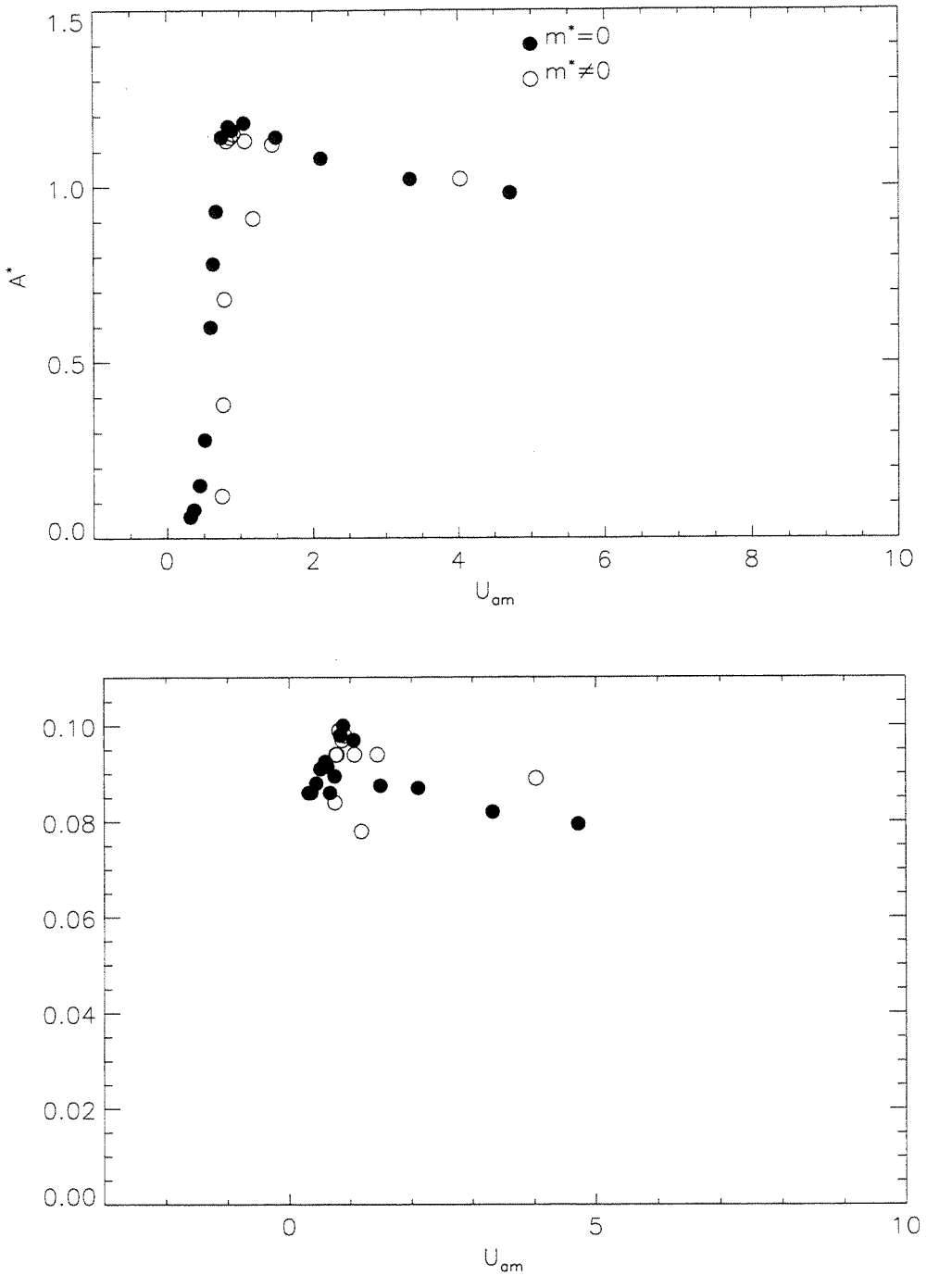


**Figure 63: Amplitude (top) and frequency (bottom) response for undamped systems with and without body inertia, plotted against the 'apparent mass' reduced velocity.**

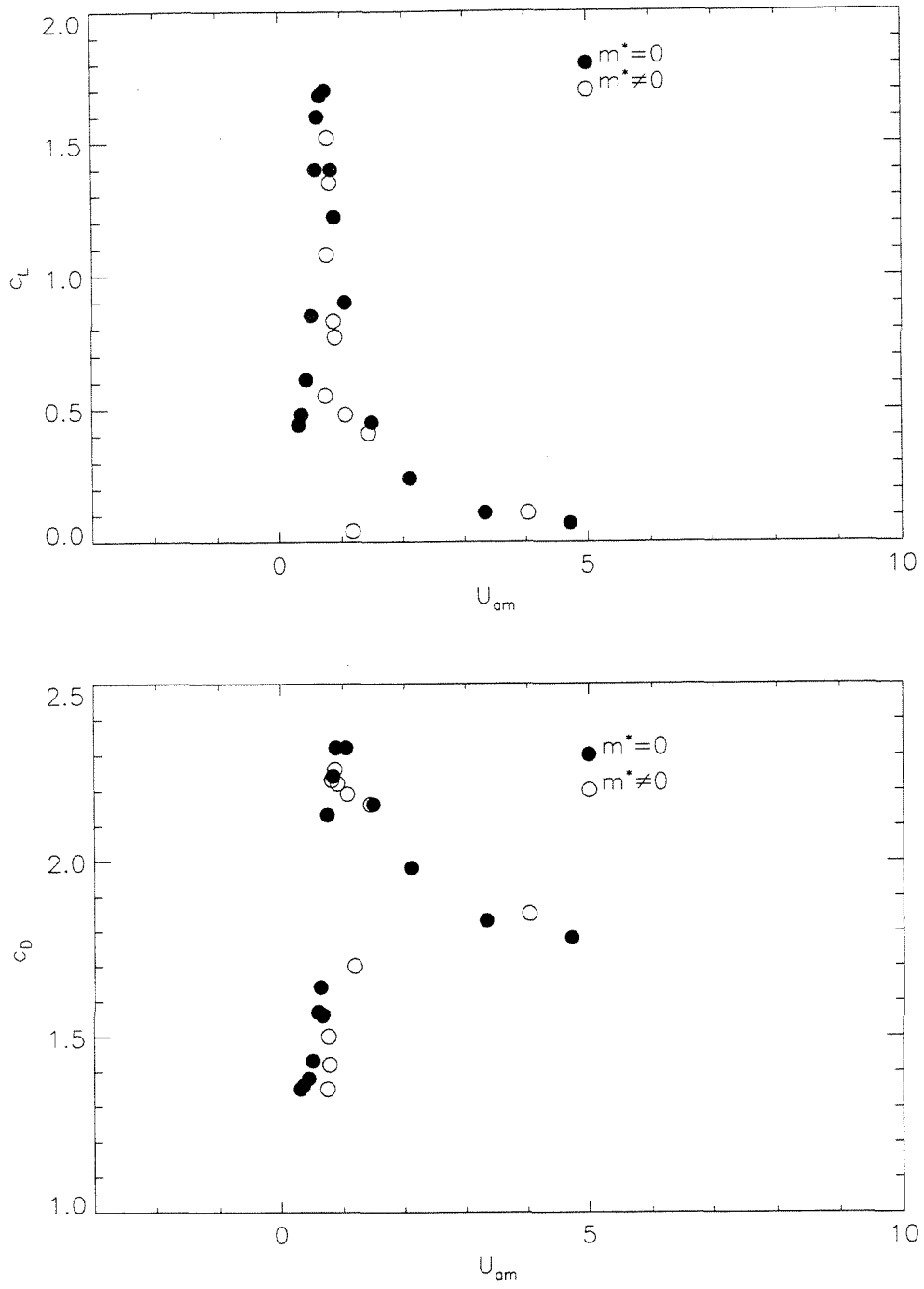


**Figure 64: Maximum lift magntude (top) and average drag (bottom) for undamped systems with and without body inertia, plotted against the 'apparent mass' reduced velocity.**

The flaws in reduced velocity scaling are further evident by comparing it to scaling by $k_{eff}^*$ on systems intentionally chosen to yield a constant reduced velocity. As seen in Figure 65, despite the fact that the reduced velocity is constant, a range of systems responses are possible. These responses can be clearly defined through scaling by the effective elastic coefficient.

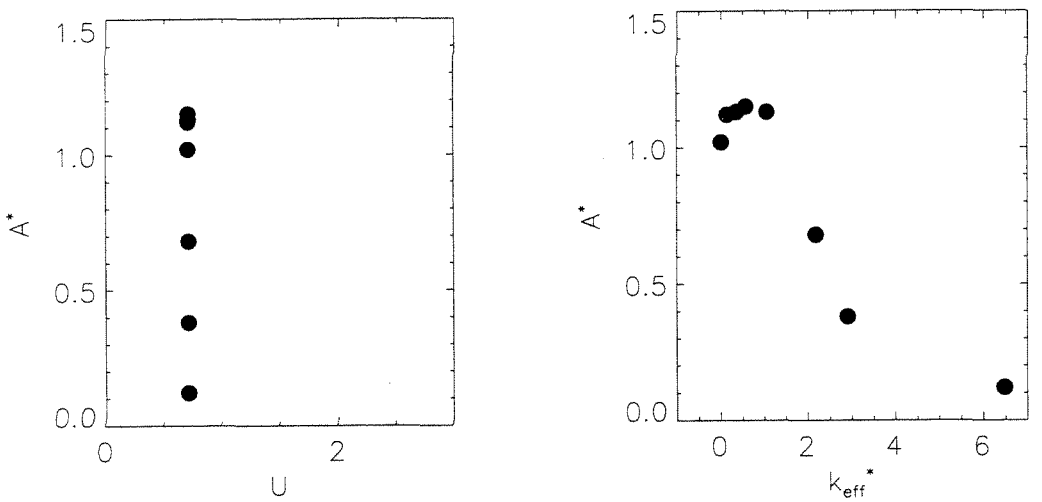


**Figure 65: Response for systems with both non-zero body mass and spring constant. Reduced velocity scaling (left) and effective elasticity (right).**

It is possible to reconcile the view of flow induced vibration for an undamped system provided above and classical lock-in behavior for which reduced velocity was considered an appropriate scaling. Note that when the system response frequency $f^*$ matches the natural mechanical frequency $f_n^*$, the effective elasticity $k_{eff}^*$ is zero by definition. Thus the lock-in state is, in fact, within the observed synchronized region in which the system experiences a large response. For a large value of $m^*$, small deviations in frequency from $f_n^*$ will quickly move the value of $k_{eff}^*$ outside the synchronized region. Thus, for large $m^*$, lock-in behavior is consistent with the observations above. Only at small $m^*$ does it become clear that lock-in does not necessarily define the system response. Perhaps the more complex synchronization between the mechanical properties, body motion, and permissible states of the wake is instead the key. Of course, the data presented in this chapter only make such conjecture possible and a much more extensive survey would be required for verification.

| $k^*$ | $m^*$ | $f^*$ | $A^*$ | $c_L$ | $c_D$ |
|---|---|---|---|---|---|
| 0.0 | 0.0 | 0.078 | 0.94 | 0.0 | 1.73 |
| 0.03535 | 0.0 | 0.080 | 0.98 | 0.07 | 1.78 |
| 0.0707 | 0.0 | 0.082 | 1.02 | 0.11 | 1.83 |
| 0.17675 | 0.0 | 0.087 | 1.08 | 0.24 | 1.98 |
| 0.3535 | 0.0 | 0.092 | 1.14 | 0.45 | 2.16 |
| 0.707 | 0.0 | 0.097 | 1.18 | 0.90 | 2.32 |
| 1.0 | 0.0 | 0.100 | 1.16 | 1.22 | 2.32 |
| 1.115 | 0.0 | 0.098 | 1.17 | 1.40 | 2.24 |
| 1.414 | 0.0 | 0.090 | 1.14 | 1.70 | 2.13 |
| 1.75 | 0.0 | 0.086 | 0.93 | 1.68 | 1.56 |
| 2.0 | 0.0 | 0.092 | 0.78 | 1.60 | 1.64 |
| 2.25 | 0.0 | 0.092 | 0.60 | 1.40 | 1.57 |
| 3.0 | 0.0 | 0.091 | 0.28 | 0.85 | 1.43 |
| 4.0 | 0.0 | 0.088 | 0.15 | 0.61 | 1.38 |
| 6.0 | 0.0 | 0.086 | 0.08 | 0.48 | 1.36 |
| 8.0 | 0.0 | 0.086 | 0.06 | 0.44 | 1.35 |
| 4.37 | 10.0 | 0.097 | 1.14 | 0.83 | 2.26 |
| 4.94 | 10.0 | 0.099 | 1.13 | 1.35 | 2.23 |
| 2.37 | 10.0 | 0.078 | 0.91 | 0.04 | 1.70 |
| 0.0 | 1.76 | 0.072 | 0.20 | 0.07 | 1.29 |
| 9.89 | 20.0 | 0.094 | 0.38 | 1.08 | 1.50 |
| 14.84 | 30.0 | 0.084 | 0.12 | 0.55 | 1.35 |
| 2.48 | 5.0 | 0.098 | 1.15 | 0.77 | 2.22 |
| 1.24 | 2.5 | 0.094 | 1.13 | 0.48 | 2.19 |
| 0.50 | 1.0 | 0.094 | 1.12 | 0.41 | 2.16 |
| 7.42 | 15.0 | 0.094 | 0.68 | 1.52 | 1.42 |
| 0.05 | 0.1 | 0.089 | 1.02 | 0.11 | 1.85 |
| 0.0 | 0.5 | 0.070 | 0.70 | 0.04 | 1.49 |
| 0.0 | 3.0 | 0.075 | 0.18 | 0.10 | 1.30 |
| 0.0 | 1.25 | 0.069 | 0.24 | 0.05 | 1.32 |
| 0.0 | 5.0 | 0.077 | 0.14 | 0.15 | 1.31 |
| 0.0 | 8.0 | 0.079 | 0.10 | 0.20 | 1.32 |
| 0.0 | 0.8 | 0.088 | 0.48 | 0.06 | 1.40 |

**Table 2: Results for Re=100 simulations with no damping ($b^*=0$).**

### 3.2.6 Effects of Non-Zero Damping

The use of zero damping provided a simplified system in which basic analysis could help to define the system response. The addition of damping complicates matters as the equation of motion for the body cannot be simplified to the same extent with a single frequency assumption. Due to the damping a phase shift must be incorporated between the lift and body response. Consider as before a single frequency response

$$y^* = A^* \sin(2\pi f^* t^*) \tag{3.17}$$

and assume the lift behaves as

$$c_L = c_{L0} \sin(2\pi f^* t^* + \phi) \tag{3.18}$$

Substitution into the equation of motion (3.2) yields two equations

$$\frac{c_{L0}}{A^*} = \sqrt{k_{eff}^{*2} + 4\pi^2 f^{*2} b^{*2}} \tag{3.19}$$

$$\phi = \tan^{-1}\left(\frac{2\pi f^* b^*}{k_{eff}^*}\right) \tag{3.20}$$

Thus, for constant damping, the parameter $k_{eff}^*$ defines the system response wherever the single frequency assumption is reasonable. Note, though, that at a given Reynolds number there could still be many families of responses as the required synchronization between the wake and body changes with $b^*$. Thus the synchronized region for $b^*=0$ studied above might not reflect the behavior at larger $b^*$. From an analytic perspective, both parameters are required to define the response of a damped system at a given Reynolds number.

In the current study, basic cases were simulated with fixed $m^*=0$ and $k^*=1$ in which damping was varied to get an idea of the effects of damping. The results in Figure 66 were fairly predictable. Damping tended to mute the amplitude response and the phase $\phi$ increased with larger damping (as the damping term thus came to dominate elastic term in the equation of motion). The frequency of response did not vary significantly, with higher frequency accompanying larger amplitude motion as observed in the undamped systems. Much more study is required to gain an idea of how damping effects can be integrated with the more complete understanding of the undamped system.

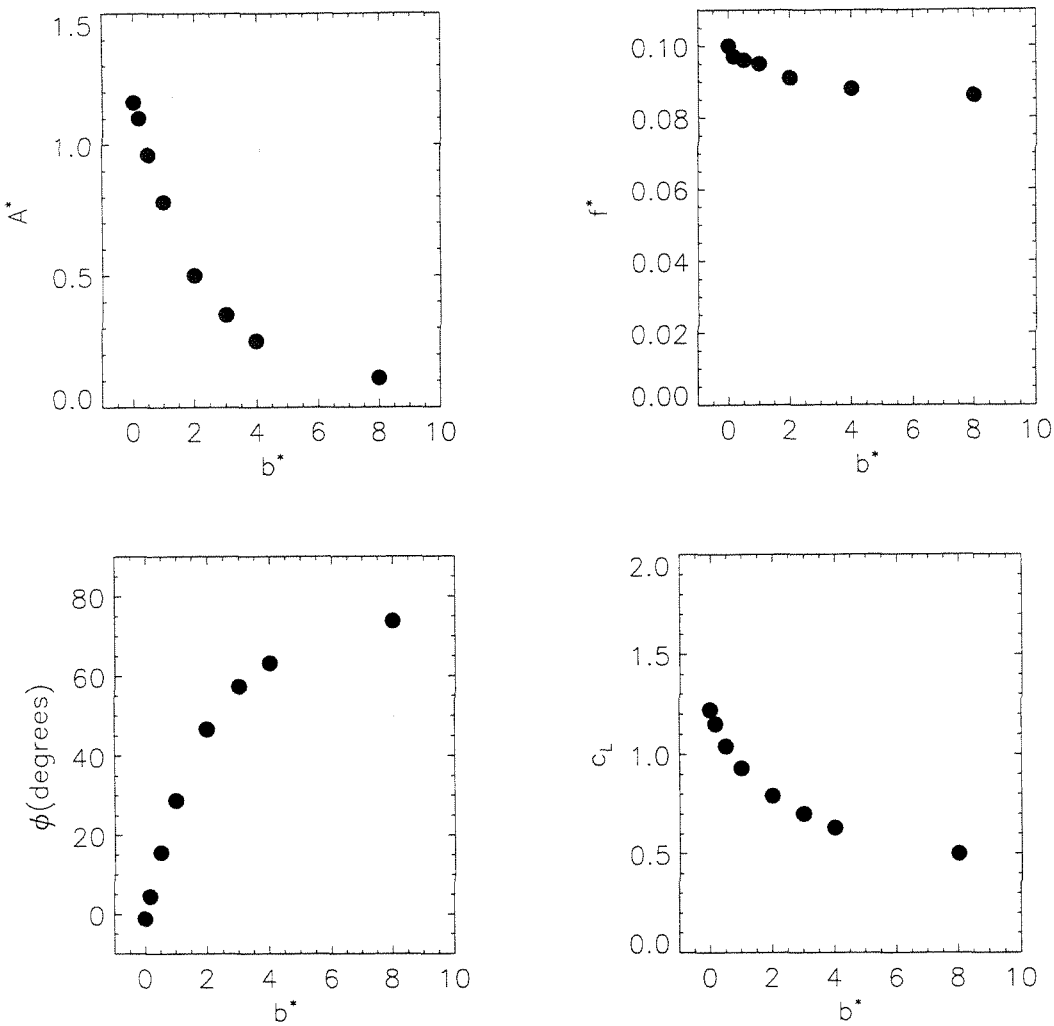


**Figure 66: Response for damped systems with $m^*=0$, $k^*=1$; amplitude (upper left), response frequency (upper right), phase (lower left), and lift (lower right).**

| $b^*$ | $f^*$ | $A^*$ | $c_L$ | $\phi$(degrees) |
|---|---|---|---|---|
| 0.0 | 0.01 | 1.16 | 1.22 | -1.16 |
| 0.1675 | 0.097 | 1.10 | 1.15 | 4.49 |
| 0.5 | 0.096 | 0.96 | 1.04 | 15.58 |
| 1.0 | 0.095 | 0.78 | 0.93 | 28.73 |
| 2.0 | 0.091 | 0.50 | 0.79 | 46.64 |
| 3.0 | 0.090 | 0.35 | 0.70 | 57.30 |
| 4.0 | 0.088 | 0.25 | 0.63 | 63.20 |
| 8.0 | 0.086 | 0.11 | 0.50 | 73.80 |

**Table 3: Results for Re=100 simulations with $m^*=0$ and $k^*=1$.**

# 4 Drag Reduction Via Rotational Oscillation - Circular Cylinder

## 4.1 Introduction

Flow over a circular cylinder has become a canonical problem for generalized study of bluff body flows. Despite the simplicity of its geometry, the flow exhibits a wealth of bedeviling phenomena such as the complex vortex dynamics of the wake, unsteady boundary layer separation points, and shear layer instability. It thus provides a testbed for study of all the primary characteristics of bluff body flows. Despite an enormous amount of attention since Roshko's[1954] measurements helped define the problem, many traits of these flows remain poorly understood.

The substantial mixing and significant forces which characterize bluff body flow are important in many practical applications. The rich nature of bluff body phenomena provide many routes towards flow control which can be beneficial in these applications. Thus much study has been directed toward control of bluff body flow. For example, a recent experiment by Tokumaru et al.[1991] revealed drag reduction, caused by the rotational oscillation of a circular cylinder in a freestream. This effect had no clear basis in previous findings in the field. Experimental observations suggested a delay in boundary layer separation might be driving the drag reduction, yet such a result is not the logical outcome for the forcing utilized. Although the rotation favors a delay when it causes the body surface to move in the flow direction, there would be a corresponding separation enhancement on the opposite half of the body. Thus the computations below were undertaken to explore the problem in more detail.

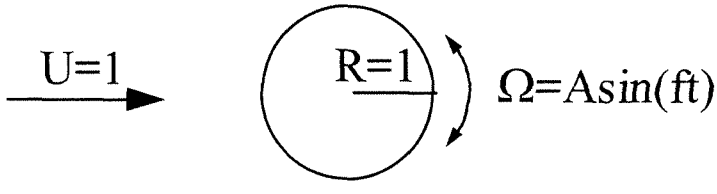


**Figure 67: Schematic of control problem.**

Tokumaru[1991] studied flow over a circular cylinder undergoing rotational oscillation $\Omega=A\sin(ft)$ while in a Re=15000 freestream. It was observed that for oscillation amplitudes on the order of the freestream velocity and at oscillation frequencies a few times higher than the natural shedding frequency, drag reduction up to 85 percent occurred. The experiment was in water (thus rendering the flow essentially incompressible), and the flow visualization in Figure 68 reflects the key observation that the forcing narrows the transverse extent of the wake, suggesting a delay in boundary layer separation.

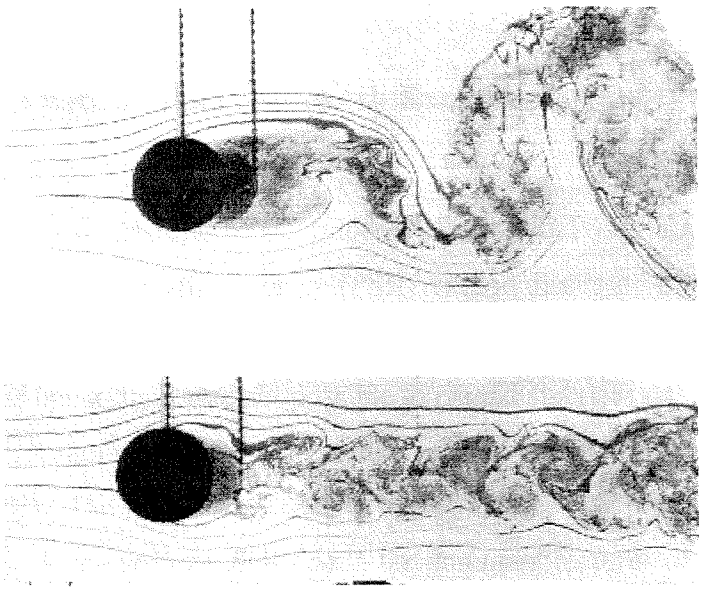

**Figure 68: Flow visualization from the Tokumaru[1991] study. Unforced flow ($\Omega=0$) at top and forced flow ($\Omega=3\sin(\pi t)$) at bottom for Re=15000 flow.**

Various questions were raised by Tokumaru's findings which the below computations endeavor to resolve. The wealth of data available from the computations provide insight to the physics driving the observed wake narrowing and drag reduction. The drag measurement from the experiment relies upon various approximations. Direct measurements from the computations help to verify the experimental force quantification. Suspicion that the drag reduction is simply the result of a turbulent transition (with the oscillation combining with the freestream to create a relative Reynolds number beyond transition) in the boundary layer can also be addressed with the boundary layer resolution

of the simulations. Although the experiment is susceptible to three-dimensional effects, the strong forcing component in the motion could impose a virtual two-dimensionality in the near wake. Also, the two-dimensional simulations can help to clarify whether the phenomenon is dominated by two- or three-dimensional effects.

Simulations at a Reynolds number of this magnitude face hurdles in achieving a high level of accuracy due to the fine length scales which become relevant as viscous effects lessen. As a result, high-resolution computation is very challenging in this case even with contemporary computational resources.

## 4.2 Simulation with Particle Strength Exchange

### 4.2.1 Background

The first set of simulations of a cylinder with rotational oscillation in Re=15000 flow utilized the particle strength exchange (PSE) method discussed in Chapter 2. Due to the fine scales in the boundary layer and the need to maintain uniform resolution with the PSE approach near the body, it was not possible to extend simulations beyond 2.5 diameters of downstream motion from an impulsive start, despite the use of a 256 processor Cray T3D. The field also needed to be regridded every few timesteps due to the severe straining in the velocity field. Still, the dominant features of the flow appeared to establish themselves rapidly and thus were apparent in these simulations. The only scenario tested with the PSE vortex method was Re=15000 flow with the cylinder oscillation given by $\Omega=2\sin(\pi t)$. For this case, Tokumaru observed the wake narrowing pictured in Figure 68 and measured a drag coefficient of $c_D \cong 0.2$ (whereas $c_D \cong 1.2$ was found in the unforced case).

### 4.2.2 Results with the Parallel Particle-Box Code

A fair amount of effort was required for parallelization (for the T3D) of a sequential code, and thus an initial simulation used the $O(N\log_2 N)$ version of the vortex method as it is quite a bit smaller than the O(N) version. The O(N) version was later

implemented due to the excessive computational load and is discussed in the next subsection.

The simulation with the $O(N\log_2 N)$ code was taken to t=5 (2.5 diameters of downstream motion), which required 40 hours of use of all 256 processors and resulted in a field with 1.7 million computational particles during the final stages of the simulations. The flow was resolved to $\Delta x \cong 0.0015$ (where the cylinder radius R=1) and $\Delta t=0.004$. Remeshing was required every third timestep in order to maintain computational stability due to the severe straining of the particle mesh. A higher-resolution simulation presented in the next subsection indicates that although some relevant scales exist at finer resolution, the key behavior seems to be captured in these computations.

Vorticity fields presented below reveal flow phenomena that could explain the findings in Tokumaru's experiment. It appears that during each half forcing cycle (every $\Delta t=1$) a multipole vorticity structure is generated on alternating sides of the cylinder that is rapidly ejected from the boundary layer and quickly convects downstream. In Figure 69, two structures on opposite halves of the flow are characterized by significant amounts of both signs of vorticity. The structure in the upper half has already entered the wake while the lower structure lies just off the body surface. At this time, the body is rotating clockwise in accordance with its prescribed motion. Thus the boundary at y=1 is moving in the same direction as the freestream, which classically suggests that boundary layer separation would be delayed in this region. Conversely, boundary layer separation would be expected to be encouraged on the lower half (y=-1) because the body is moving in opposition to the freestream.

Thus, the behavior apparent in Figure 70 is surprising. While the body has rotated clockwise, a good deal of vorticity is seen lifting off the body on the upper-half, where suppression of separation was expected. Meanwhile, the boundary layer region appears quiescent on the lower half where separation enhancement was expected. Note also that the original multipole vortex structure on the upper half continues to move downstream and the multipole structure on the lower half has risen sharply off the body and downstream.

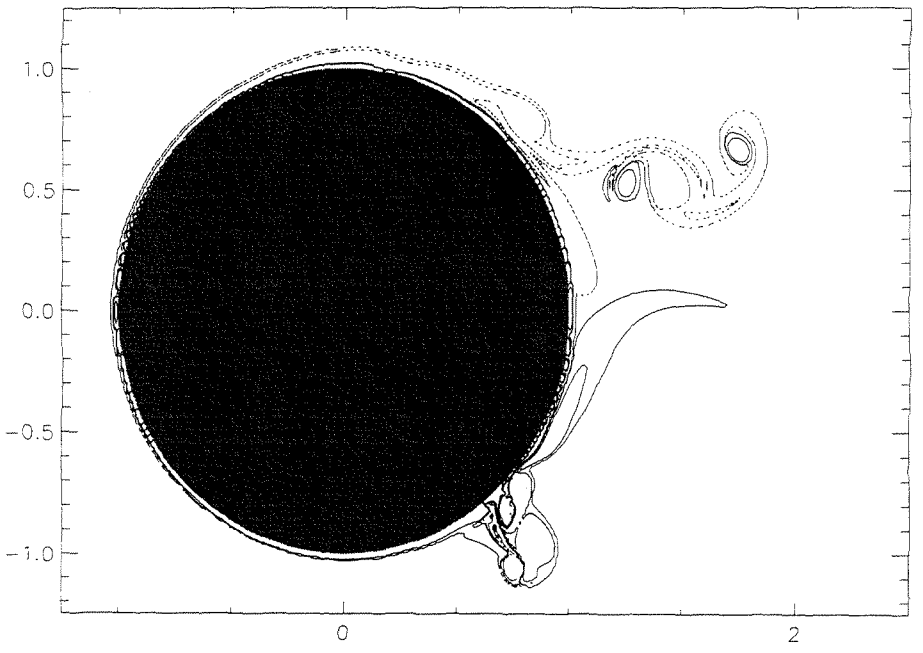


**Figure 69: Vorticity field for Re=15000 flow, $\Omega=2\sin(\pi t)$, t=3.15, contours at $\omega=\pm1$, $\pm10$. Positive vorticity is designated with solid lines, negative with dashed lines.**

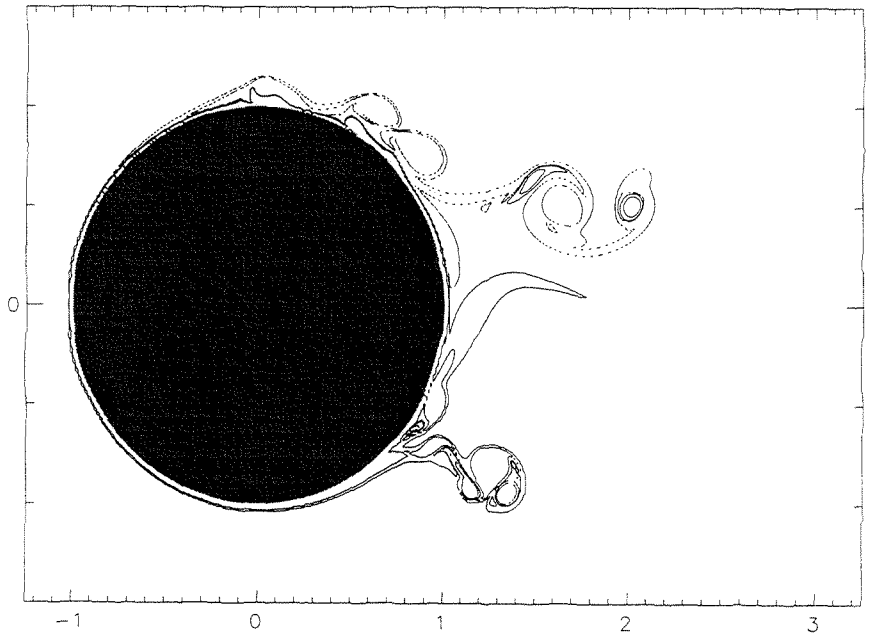


**Figure 70: Vorticity field for Re=15000 flow, $\Omega=2\sin(\pi t)$, t=3.6, contours at $\omega=\pm1$, $\pm10$.**

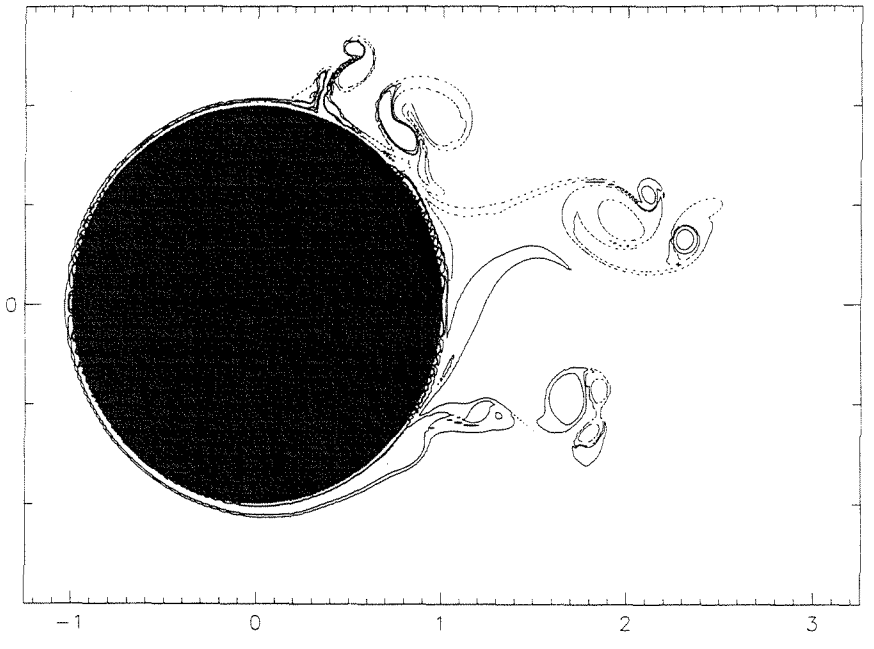


**Figure 71: Vorticity field for Re=15000 flow, $\Omega=2\sin(\pi t)$, t=4.0, contours at $\omega=\pm1, \pm10$.**

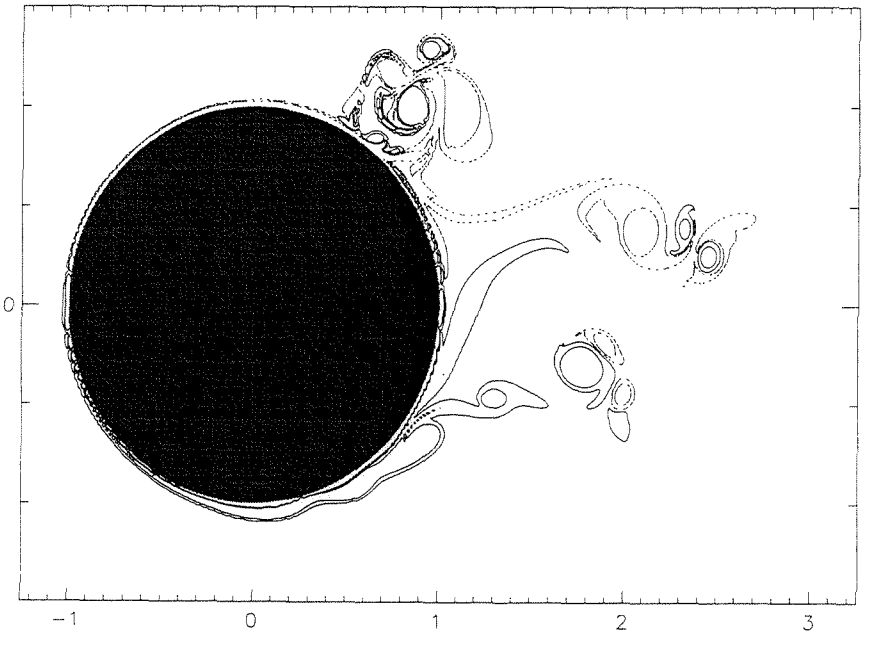


**Figure 72: Vorticity field for Re=15000 flow, $\Omega=2\sin(\pi t)$, t=4.3, contours at $\omega=\pm1, \pm10$.**

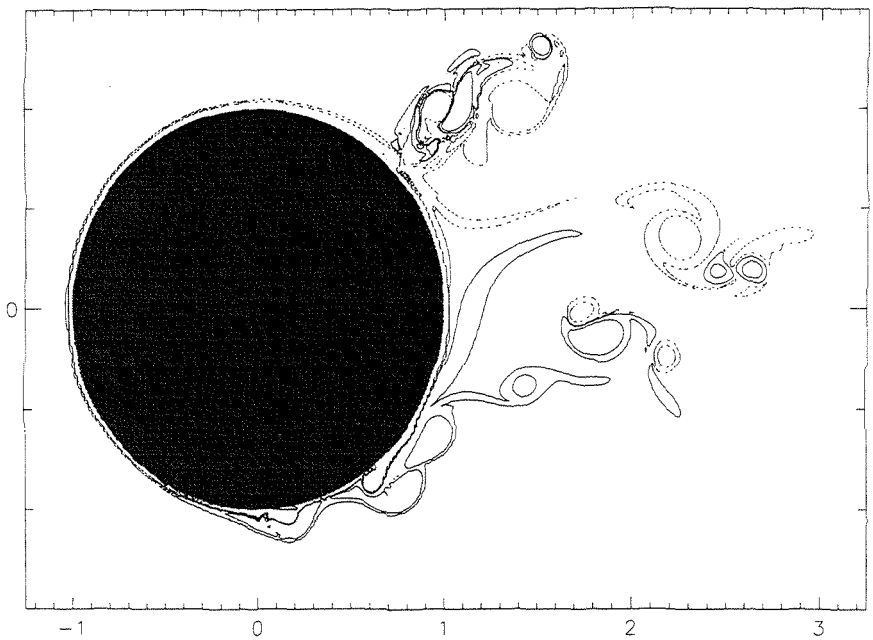


**Figure 73: Vorticity field for Re=15000 flow, $\Omega=2\sin(\pi t)$, t=4.6, contours at $\omega=\pm1$, $\pm10$.**

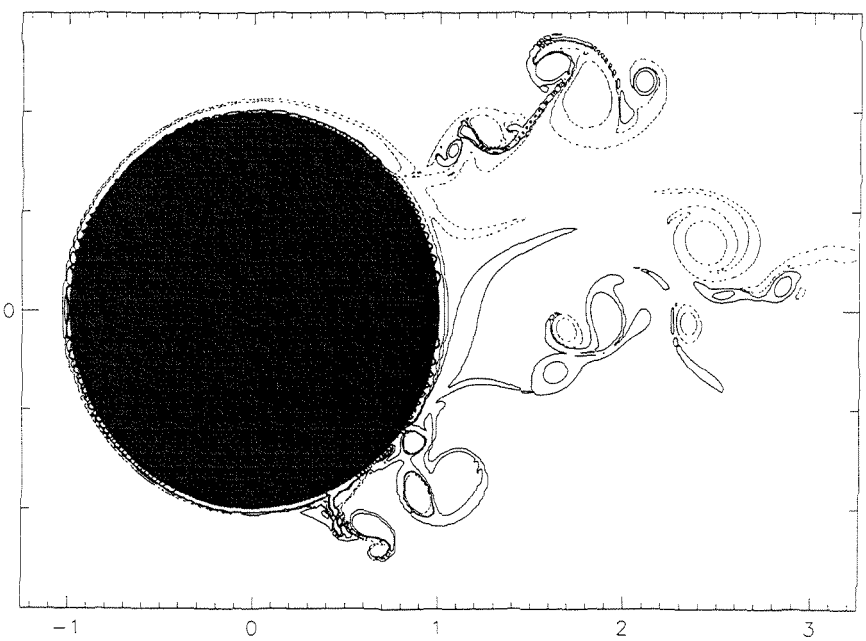


**Figure 74: Vorticity field for Re=15000 flow, $\Omega=2\sin(\pi t)$, t=5.0, contours at $\omega=\pm1$, $\pm10$.**

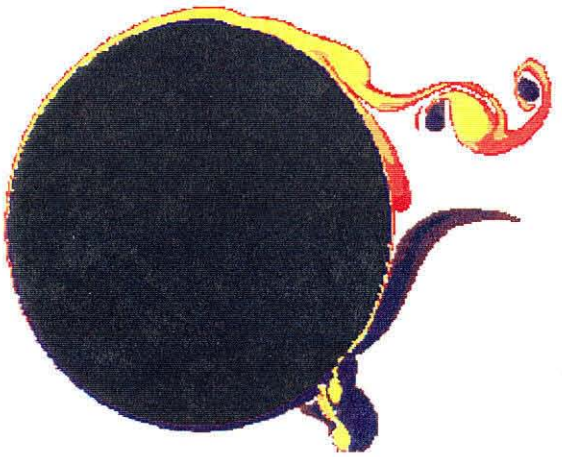

**Figure 75: Color vorticity plot at t=3.15**

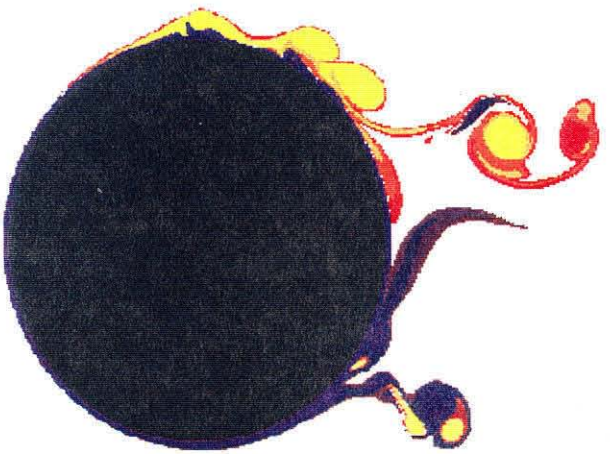

**Figure 76: Color vorticity plot at t=3.6.**

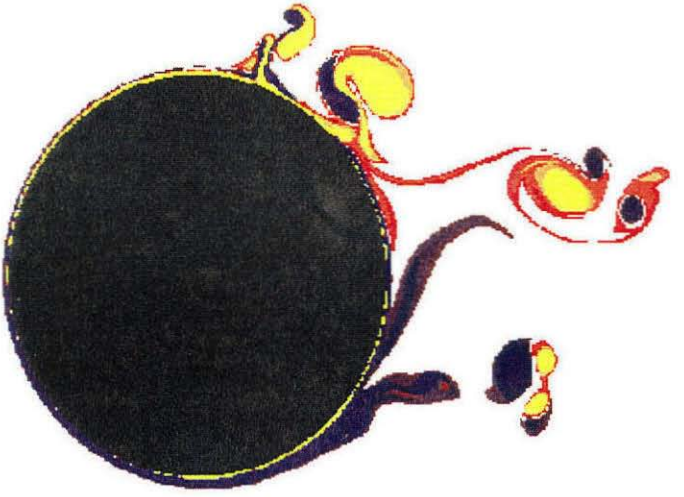

**Figure 77: Color vorticity plot at t=4.0.**

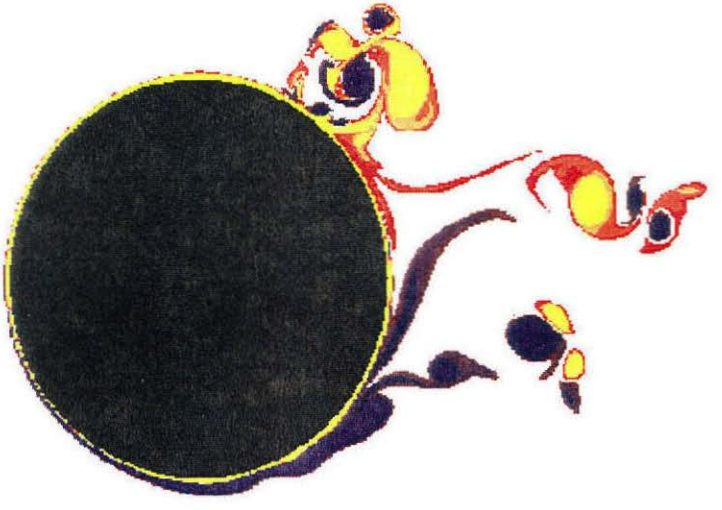

**Figure 78: Color vorticity plot at t=4.3.**

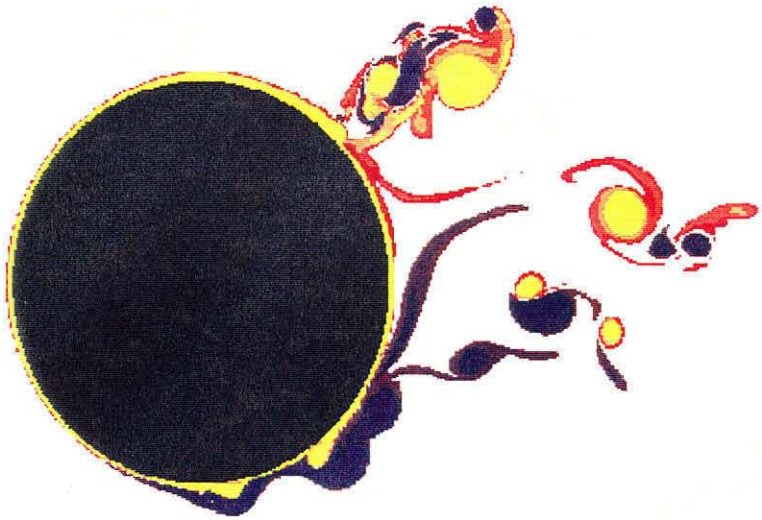

**Figure 79: Color vorticity plot at t=4.6.**

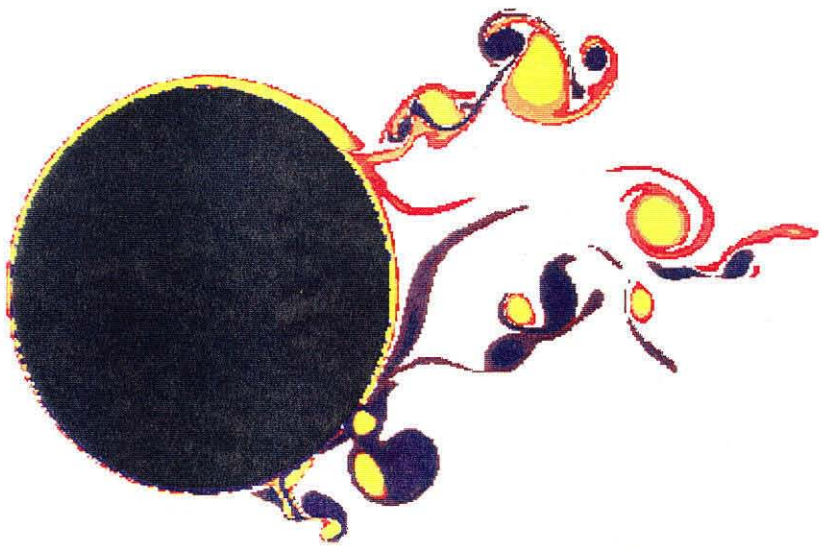

**Figure 80: Color vorticity plot at t=5.0.**

When the body has completed its clockwise rotation in Figure 71, the original structures have clearly shed from the body and entered the freestream and two new multipole vortex structures have risen during this half-cycle from the boundary layer on the upper half of the body. In Figure 72, Figure 73, and Figure 74, the same cycle repeats itself, but on the opposite half of the cylinder with rotation of the body counter-clockwise. In these plots, note the new vortex structures formed during the cycle of motion and their subsequent detachment from the body and convection into the near wake. They are considerably more complex than the original two structures apparent in Figure 69.

The simulation was stopped at t=5 as the computational expense, which increases with the wake growth, was becoming excessive. The vorticity in the wake was still too close to the body to attempt the wake approximation techniques discussed in Chapter 2. However, trends can clearly be seen developing by this time. The drag coefficient, given in Figure 81, is trending to lower values than the experimental measurements for a non-rotating cylinder of $c_D \cong 1.2$. The sharp unsteadiness observed in the drag coefficient appears to be related to the growth period of the multipole vorticity structures near the body. The distribution of pressure around the body at t=5 is shown in Figure 82. Pressure is obtained by relating the tangential pressure gradient on the body surface to the normal gradient of the vorticity field with the momentum equation, as given in Appendix A. It can thus be related to the strength of the vortex sheet used to satisfy the boundary condition, as derived in Chapter 2, due to its relationship to the vorticity field gradient. This method provides only a relative measure of the pressure as the precise value in relation to a reference quantity (such as the pressure in the undisturbed freestream) is not determined in this approach. The pressure distribution clearly indicates a strong recovery, indicative of a delay in separation and explaining the reduced level of the drag. The streamlines at t=5 are also plotted in Figure 83.

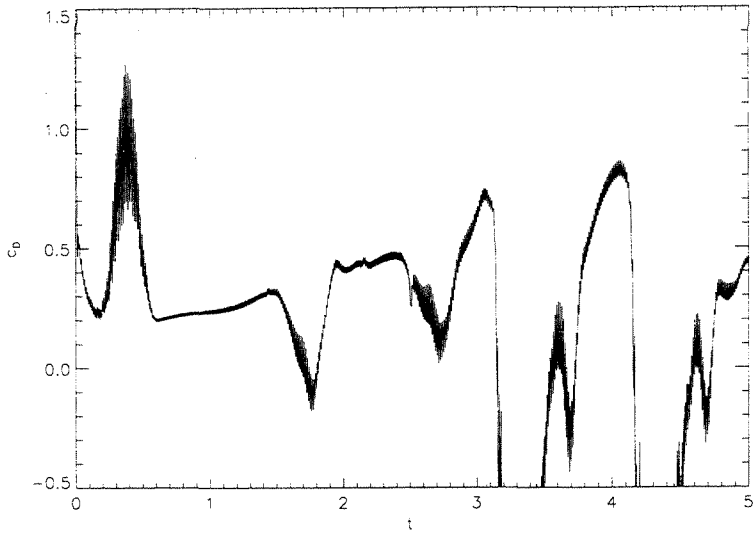


**Figure 81: Drag for Re=15000 simulation, $\Omega=2\sin(\pi t)$.**

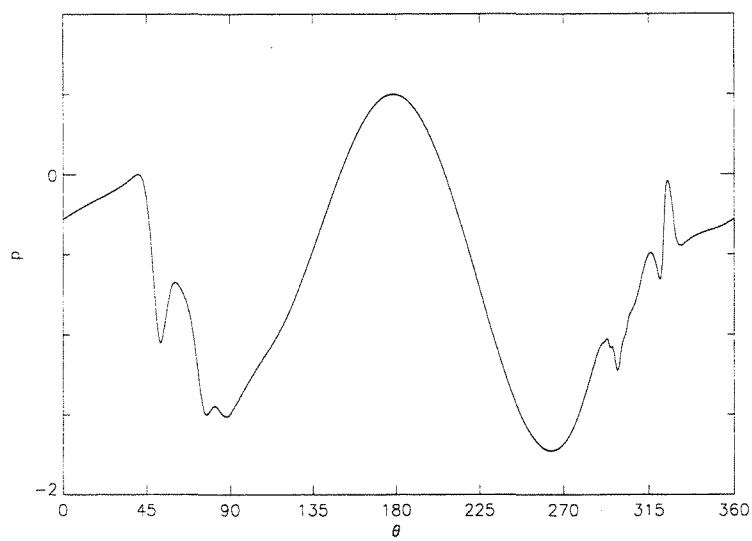


**Figure 82: Pressure distribution on the cylinder surface for Re=15000 flow, *$\Omega=2\sin(\pi t)$, at $t=5$. The reference value $p(\theta=180^{o})=0.5$ is chosen, which would be the* upstream stagnation point in the potential flow over a fixed cylinder.**

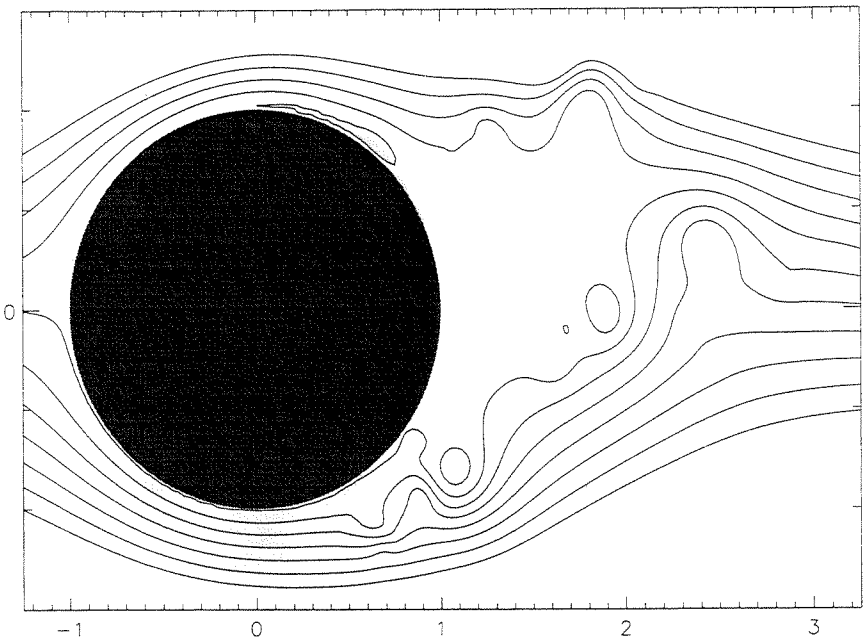


**Figure 83: Streamlines for Re=15000 flow, $\Omega=2\sin(\pi t)$, at t=5.**

### 4.2.3 Results with the Parallel Box-Box Code

In order to run a convergence test on the results in 4.2.2, an O(N) implementation of the vortex method was parallelized and used to simulate the same flow with $\Delta x \cong 0.001$ and $\Delta t=0.0025$. By t=3.15, this computation required almost 60 hours of use of 256 processors on the Cray T3D and entailed over 2 million computational particles. The vorticity field which evolved in this computation can be viewed in Figure 84 and the resultant drag coefficient in Figure 85. Similarities can be seen to the O(NlogN) simulation in both the generally reduced magnitude of the drag coefficient and the generation of the large vortex structures in the vorticity field. However, some smaller scale discrepancies exist between the two vorticity fields and the drag coefficient in Figure 85 does not exhibit the same level of unsteadiness as in Figure 81. The results strongly suggest that the computations have converged to the large-scale dynamics which characterize this flow but have not fully resolved smaller scale features. In an attempt to illuminate the dynamics behind the growth of the multipole vorticity structures, the velocity field inside the boundary layer is examined in Figure 86 through Figure 89. These fields are discussed in the next section.

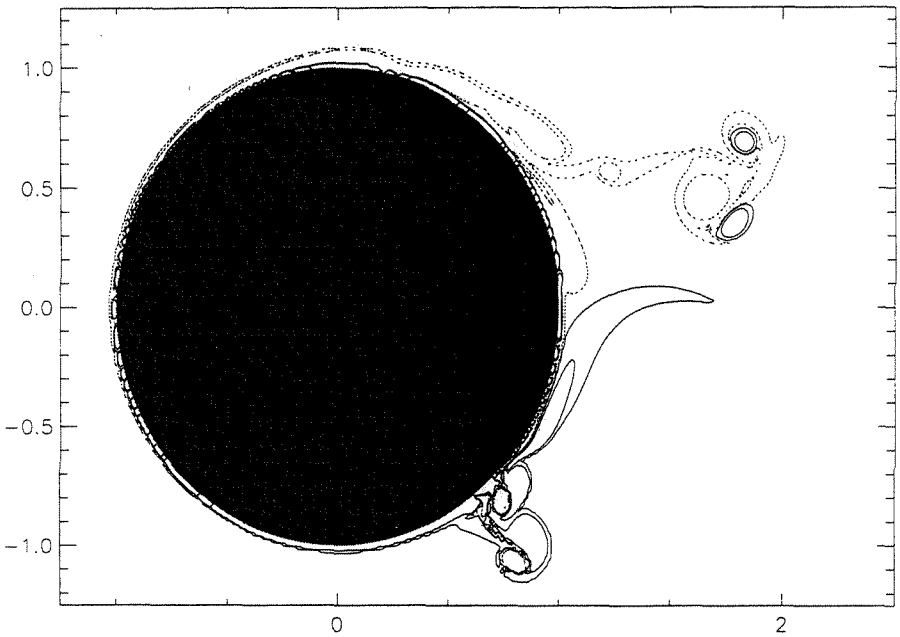


**Figure 84: Vorticity field for Re=15000 flow, Ω=2sin(πt), t=3.15, contours at ω=±1, ±10. Implementation of the O(N) technique.**

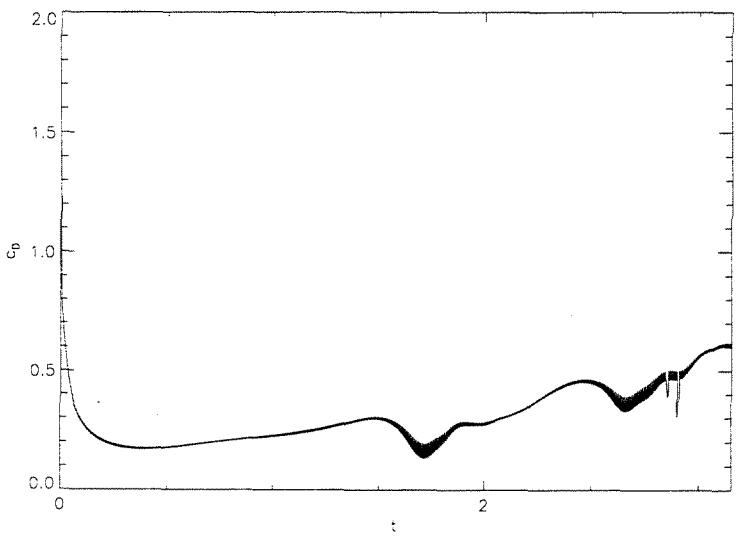


**Figure 85: Drag for Re=15000 simulation, Ω=2sin(πt). Use of the O(N) implementation.**

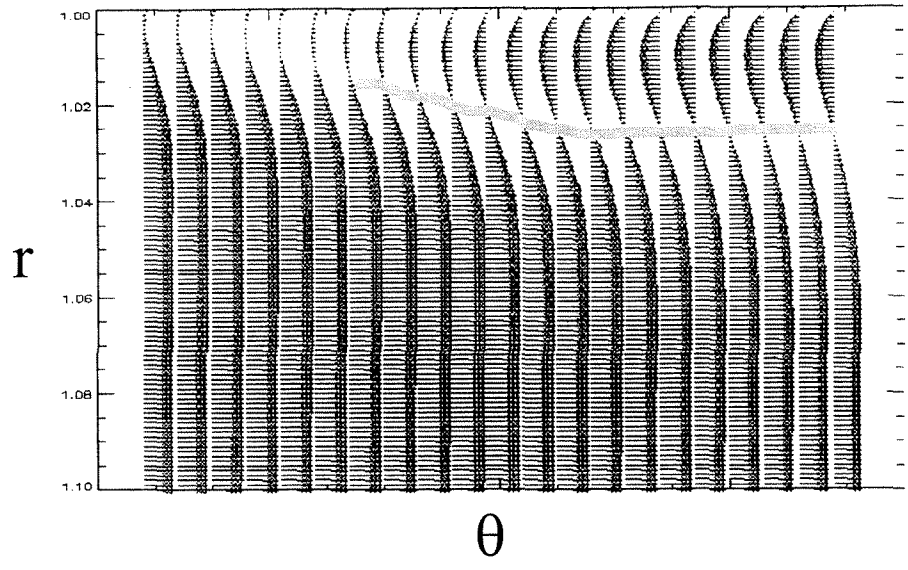


**Figure 86: Velocity vectors in the boundary layer at t=2.05. Plot from r=1.0 at top to r=1.1 at bottom and θ=250° at left to θ=310° at right. The gray line approximates a $\underline{u}$=0 contour.**

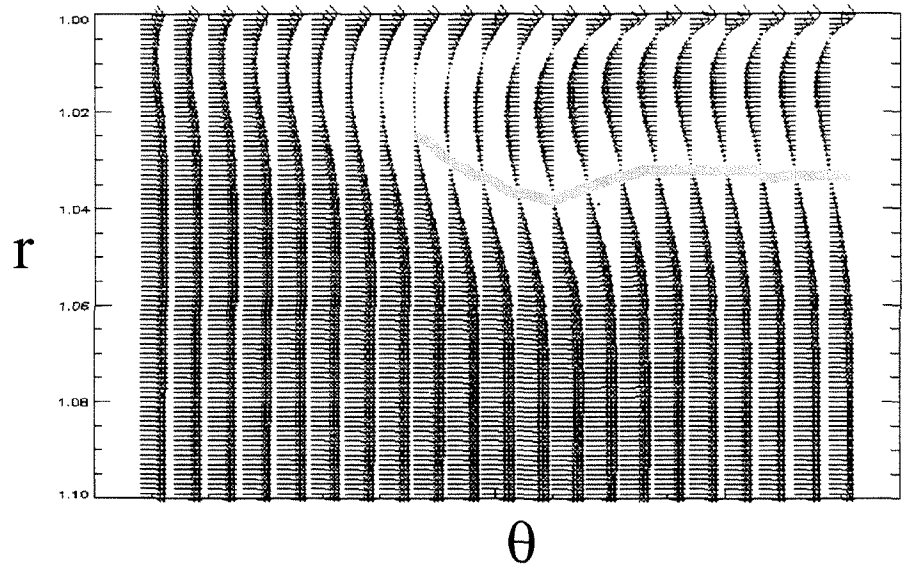


**Figure 87: Velocity vectors in the boundary layer at t=2.15. Plot from r=1.0 at top to r=1.1 at bottom and θ=250° at left to θ=310° at right. The gray line approximates a $\underline{u}$=0 contour.**

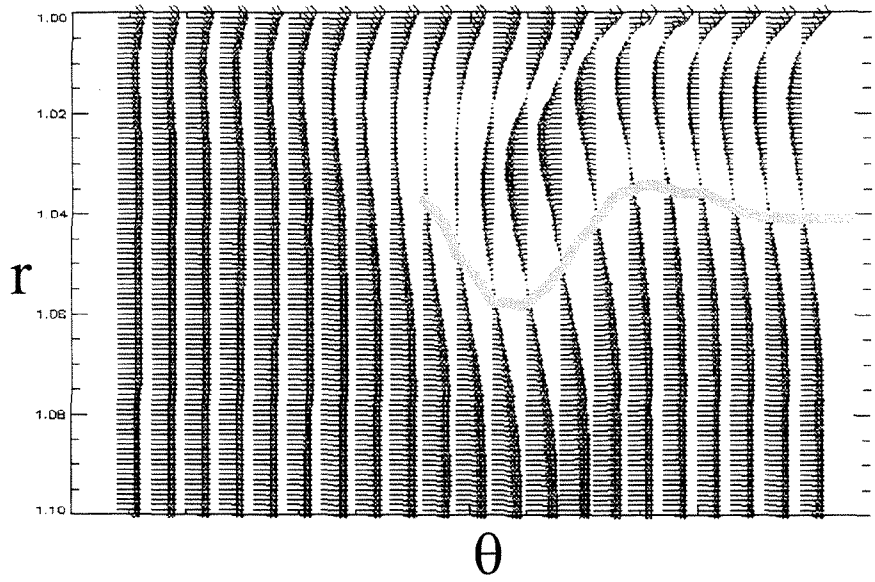


**Figure 88: Velocity vectors in the boundary layer at t=2.3. Plot from r=1.0 at top to r=1.1 at bottom and θ=250° at left to θ=310° at right. The gray line approximates a $\underline{u}$=0 contour.**

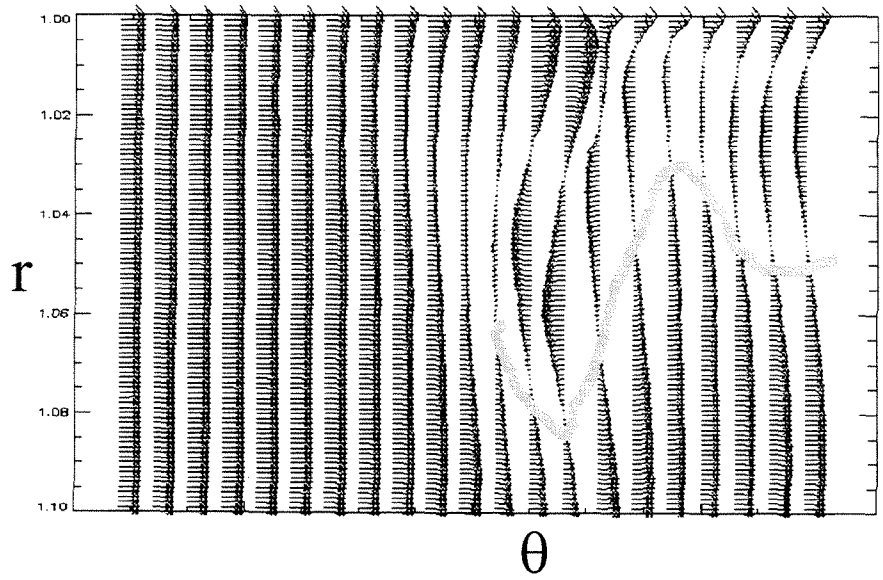


**Figure 89: Velocity vectors in the boundary layer at t=2.6. Plot from r=1.0 at top to r=1.1 at bottom and θ=250° at left to θ=310° at right. The gray line approximates a $\underline{u}$=0 contour.**

### 4.2.4 Analysis

The simulations presented in 4.2.2 and 4.2.3 shed light on an unexpected phenomenon which appears to dominate the dynamics of this reduced-drag flow. The observation of multipole vortex structures which erupt from the boundary layer each half-cycle of forcing on alternating sides of the body agrees with the shedding patterns observed in Tokumaru's work. The existence of both signs of vorticity in each structure and the orientation of the structure induces a local velocity field that draws the structure away from the body in much the same way a vortex dipole propels itself. The structures thus enter the freestream and convect quickly away rather than agglomerating in the cylinder wake and establishing large-scale separation.

Such observations are tempered by the relatively short duration of these computations, but they do agree qualitatively with the experimental results and there is clearly a trend toward periodic behavior, as exhibited in the comparison of Figure 70 and Figure 73, and of Figure 71 and Figure 74. Furthermore, the velocity fields in the boundary layer provide a sensible explanation for the growth of the observed multipole structures. In Figure 86, the boundary layer from the clockwise rotation of t=1-2 can be seen drifting off the surface of the body as the counter-clockwise rotation begins at t=2. The gray line in the figures is used to track the evolution of this boundary layer, which essentially becomes a free shear layer as the counter-clockwise rotation of the t=2-3 cycle frees it from the restrictions of the solid boundary. The shear layer is strong enough to develop an instability, which rapidly grows without the boundary as an impediment. The vortex resulting from this instability can interact with the nearby boundary to generate an opposite-signed vortex. Thus a dipole vortex structure is formed, which then quickly pulls itself outside the boundary layer.

This unexpected instability provides a satisfying explanation of the observations in Tokumaru's experiment. The instability draws a great deal of vorticity far enough from the body to permit it to shed downstream rather than get caught in a recirculation region. By drawing this vorticity out of the boundary layer, apparently sufficient vorticity never remains in the near-wake to establish a large-scale recirculation. Thus separation is delayed, leading to pressure profiles such as in Figure 82. Further evidence that separation is being delayed is provided by the tongues of vorticity near the wake

centerline in Figure 74, representing the shear layers that would normally have separated from the cylinder much earlier.

Another view of how the flow dynamics observed in the above simulations supports drag reduction is given by considering drag as it can be expressed from the vorticity perspective, as shown in Appendix A,

$$\text{Drag} = -\rho \frac{d}{dt}\left( \iint_A y\omega dA \right) \tag{3.21}$$

where the area A represents the entire flowfield. The observed boundary layer instability forces vortex structures which are shed from the body to contain significant components of both signs of vorticity. With comparable vortices of opposing sign in relatively the same location, (3.21) would thus predict a lesser drag than for the unforced case where structures of one sign of vorticity are more prevalent.

As noted above, the simulations this analysis is based on are not fully converged. However, the dominant dynamics of the boundary layer instability leading to ejection of multipole vorticity structures appear to exist on scales that are properly resolved.

## 4.3 Simulation with Core Expansion

### 4.3.1 Convergence

In order to attempt longer-duration simulations of flow at Re=15000, a vortex method with the core expansion technique for diffusion is used. The goal of these computations is to simply capture the dominant behavior observed in the PSE simulation while relaxing the level of resolution to an extent that allows simulation of the flow to a well-developed state. In order to identify appropriate choices for the parameters of the core expansion simulations, test cases are run on the Re=15000, $\Omega=2\sin(\pi t)$ flow. The resultant vorticity fields and drag coefficients are compared to the benchmarks results shown in Figure 84 and Figure 85 respectively.

Three sets of parameters were tested to assess the accuracy of the core expansion method on the flow. The highest-resolution case provides confidence that the method will converge towards the PSE results at the relevant scales. This simulation used

$\Delta t$=0.005, C=4, $K_{res}$=25, $r_{bl}$=5, $N_{fuse}$=5, $(r^2/\sigma^2)_{max}$=0.25 and required 13 hours on a single processor of a Cray J90 (which is approximately equivalent to 26 hours on a 200MHz Pentium Pro for the code used). Comparison between vector and parallel computers can be difficult to quantify, but an hour on a single J90 processor could be considered substantially less 'costly' than an hour of use of 256 processors of a Cray T3D. By the end of the simulation, only 170,000 computational elements were required as compared to the 2 million for the simulation in 4.2.3. The vorticity field in Figure 90 exhibits the familiar growth and ejection of multipole vorticity structures, although the structures are a bit more complex than in the PSE simulations. Considering the aggressive spatial resolution adaptation being applied in this case, the field is in good agreement with the PSE simulations, obtaining similar qualitative behavior. The drag coefficient also exhibits a similar evolution to the PSE results. It exhibits more small-amplitude noise than the PSE results, perhaps due to the awkward nature of particle splitting near boundaries, but avoids the large deviations from the general trend seen in the PSE-derived drag in Figure 81. This may indicate that those large deviations reflected the inaccuracy particle field straining leads to in PSE simulations. The PSE drag in Figure 85 perhaps does not have the same deviations as it is run at a lower timestep and thus there are smaller time intervals between remeshings.

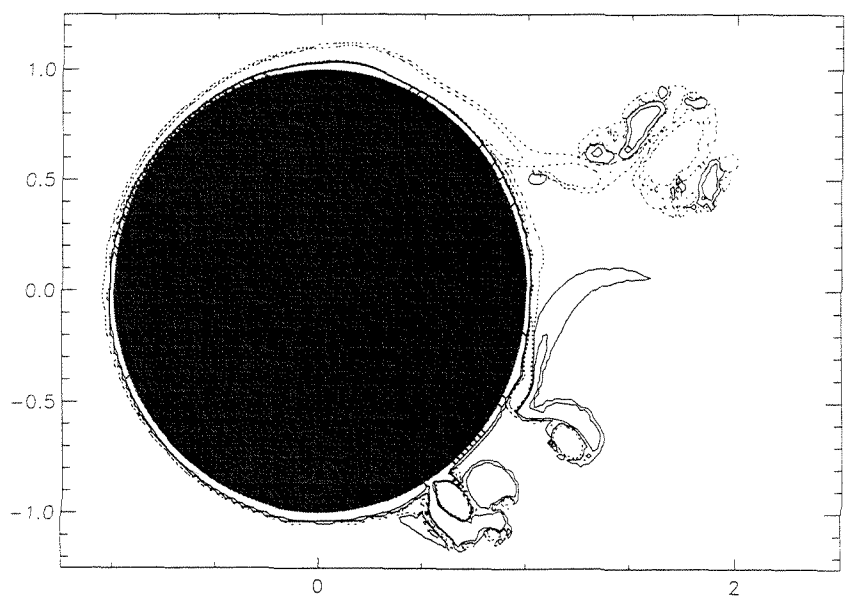


**Figure 90: Vorticity field for Re=15000, $\Omega$=2sin($\pi$t), t=3.15, contours at $\omega$=±1, ±10. Implementation of the core expansion technique with $\Delta t$=0.005 (highest resolution).**

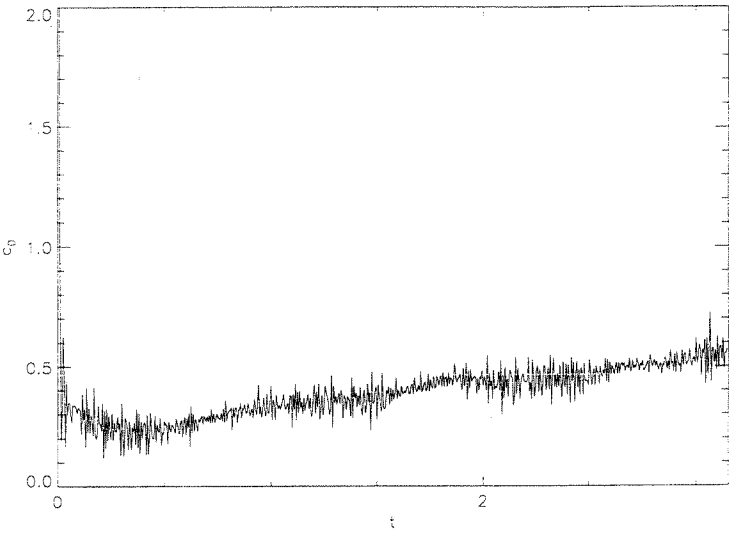


**Figure 91: Drag for Re=15000 flow, $\Omega=2\sin(\pi t)$. Implementation of the core expansion technique with $\Delta t=0.005$ (highest resolution).**

A second simulation at medium resolution preserves the trait of generation of the multipole structures every half-cycle and sheds them in a similar manner to the higher-resolution tests, but loses quite a bit of finer detail accuracy. This computation is set up with $\Delta t=0.01$, $C=4$, $K_{res}=100$, $r_{bl}=5$, $N_{fuse}=10$, $(r^2/\sigma^2)_{max}=0.5$ and required 2 hours on a single processor of a Cray J90 and 20,000 computational elements. Figure 93 indicates that the reduced-drag aspect of the flow is still captured by the medium resolution of the dynamics given by the field in Figure 92.

The lowest resolution simulation is implemented with the parameters $\Delta t=0.02$, $C=4$, $K_{res}=100$, $r_{bl}=5$, $N_{fuse}=10$, $(r^2/\sigma^2)_{max}=0.5$ and required under one hour on a single processor of a Cray J90 and 12,000 computational elements. Here a critical point in the required resolution is apparently exceeded and the basic dynamics of the flow change. The rotation still forces the shedding of a vorticity structure each half cycle, but in Figure 94 it can been seen that the structure is more composed of a single sign of vorticity and does not eject as far from the body. Thus it is possible that it has not actually been shed downstream. The growth of an instability on the lower half of the cylinder is also clearly modified by the lower resolution as again there is less interaction between the opposing signs of vorticity. Figure 95 indicates that the dynamics lost due to the coarse resolution

triggered the previously observed drag reduction as in this simulation the drag is considerably higher.

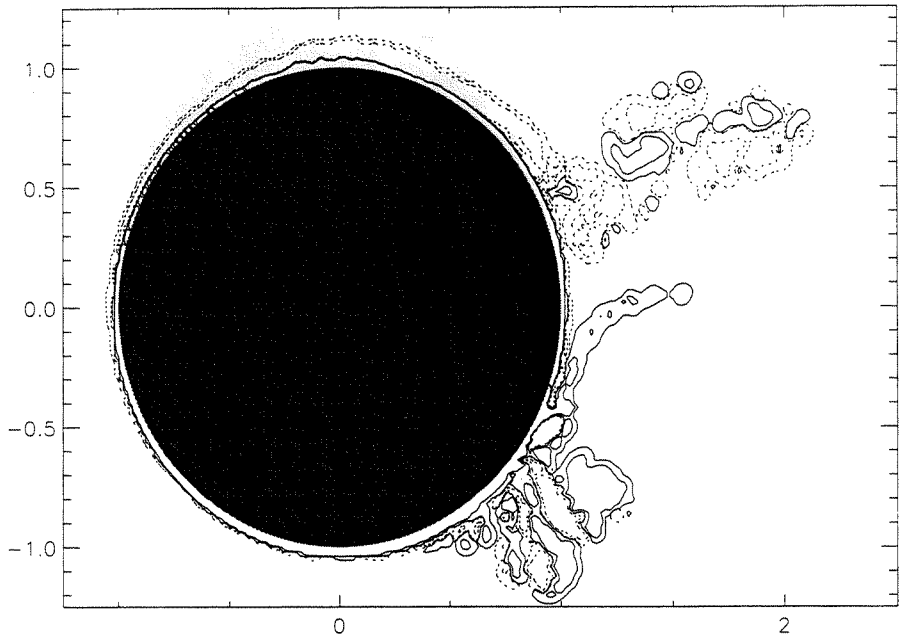


**Figure 92: Vorticity field for Re=15000, Ω=2sin(πt), t=3.15, contours at ω=±1, ±10. Implementation of the core expansion technique with Δt=0.01 (medium resolution).**

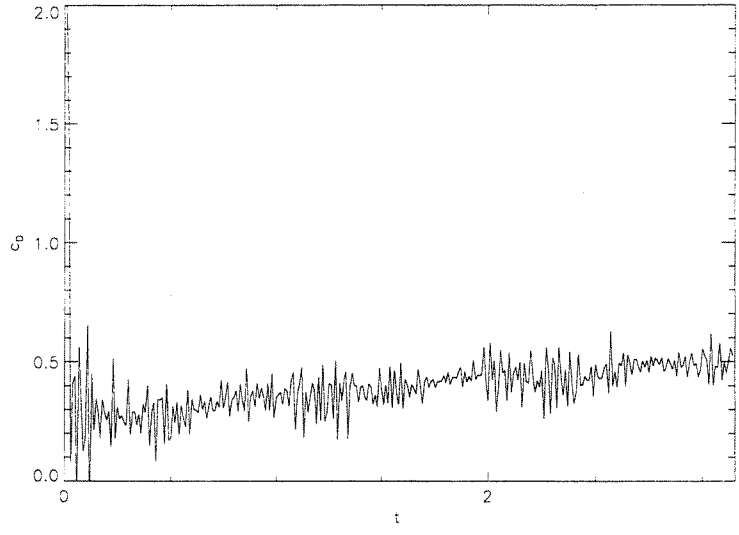


**Figure 93: Drag for Re=15000 flow, Ω=2sin(πt). Implementation of the core expansion technique with Δt=0.01 (medium resolution).**

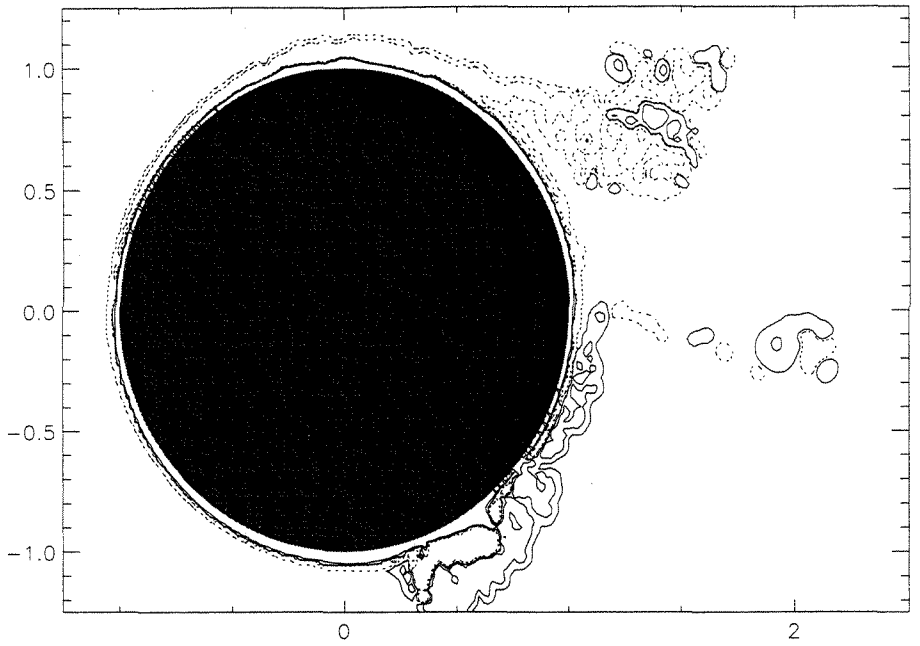


**Figure 94: Vorticity field for Re=15000, Ω=2sin(πt), t=3.15, contours at ω=±1, ±10. Implementation of the core expansion technique with Δt=0.02 (lowest resolution).**

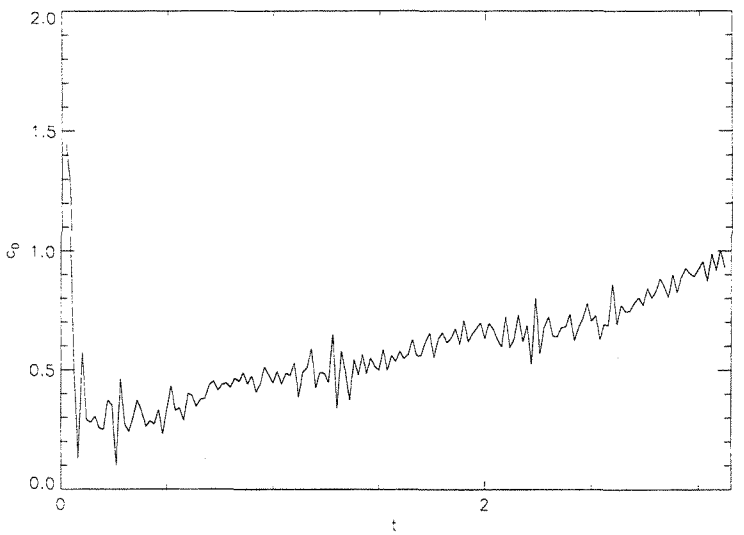


**Figure 95: Drag for Re=15000 flow, Ω=2sin(πt). Implementation of the core expansion technique with Δt=0.02 (lowest resolution).**

Subsequent core expansion simulations in this chapter use the parameters for the Δt=0.01 simulation as it seems to capture the crucial dynamics while gaining much

computational efficiency by sacrificing some finer details captured by higher resolution simulations.

### 4.3.2 Re=15000 Simulations

The core expansion method selected in 4.3.1 is used to simulate Re=15000 flow with $\Omega=2\sin(\pi t)$ forcing to t=50, at which point the system is clearly settled into long-time behavior. The flow is distinguished by the ejection of a multipole vorticity structure every half-cycle as observed in the starting flow simulations above and exhibits a greatly reduced drag. The evolution of the vorticity field over the half cycle t=50-51 exhibits the same general behavior as the first shed structures seen in the simulations above. As presented in Figure 96 through Figure 100, a structure evolves on the lower half of the cylinder where the rotational motion parallels the freestream. The structure from the previous half-cycle on the upper half of the cylinder is ejected into a wake which exhibits no large-scale separation. Note again the parallels between the flow at t=50 in Figure 96 and the flow at t=51 in Figure 100.

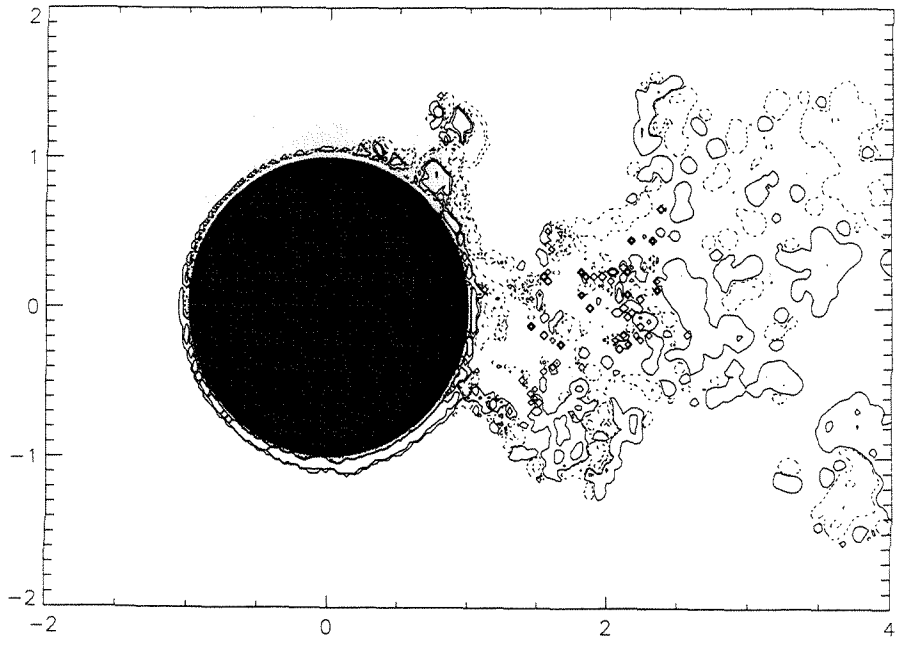


**Figure 96: Vorticity field for Re=15000 flow, $\Omega=2\sin(\pi t)$, t=50, contours at $\omega=\pm1$, $\pm10$.**

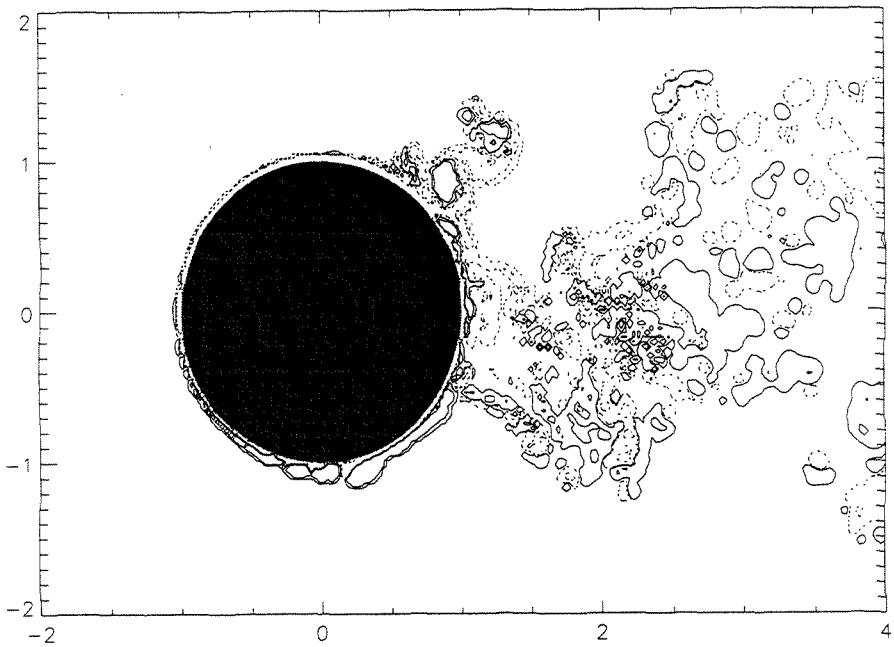


**Figure 97: Vorticity field for Re=15000 flow, Ω=2sin(πt), t=50.25, contours at ω=±1, ±10.**

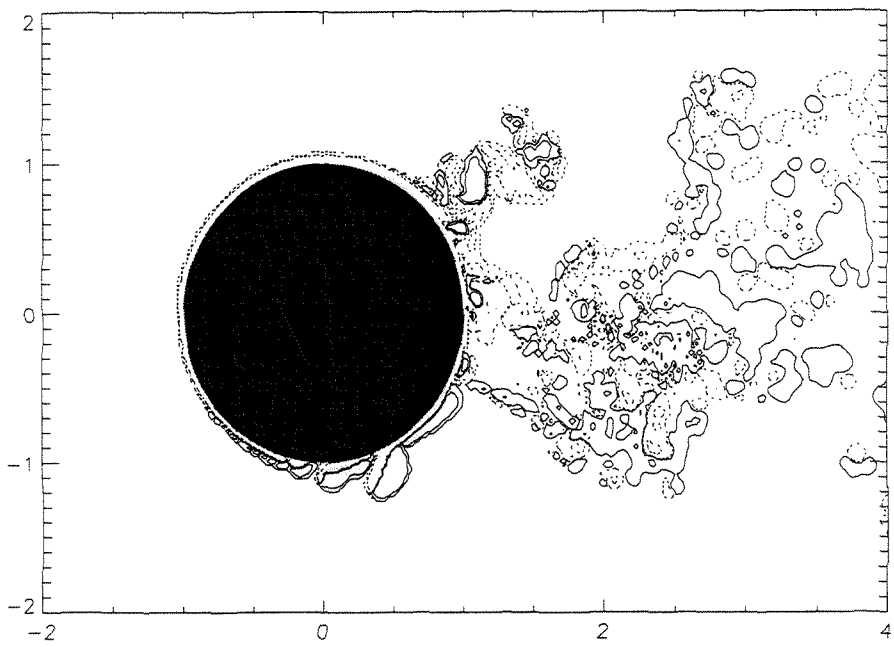


**Figure 98: Vorticity field for Re=15000 flow, Ω=2sin(πt), t=50.5, contours at ω=±1, ±10.**

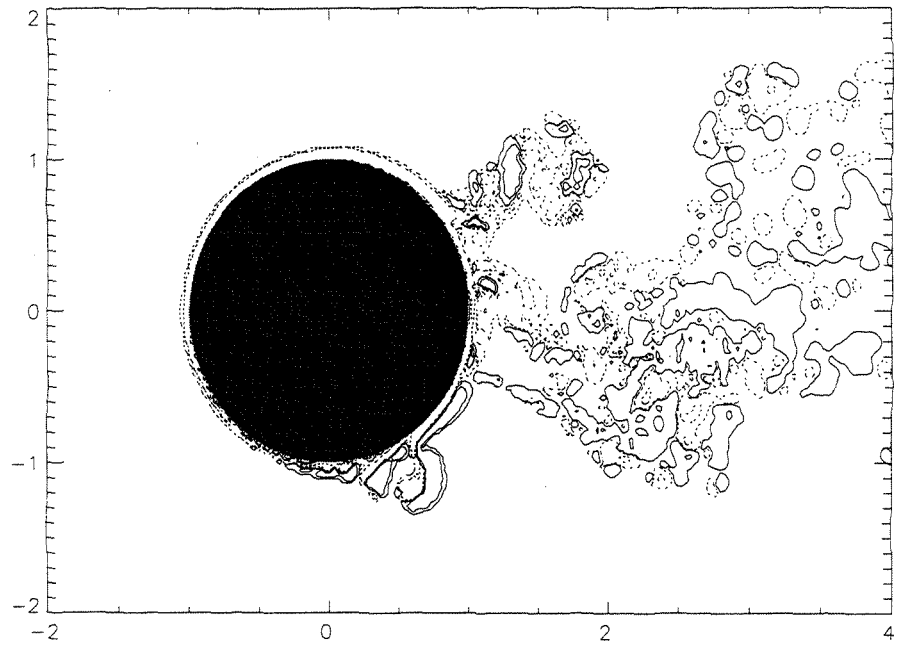


**Figure 99: Vorticity field for Re=15000 flow, Ω=2sin(πt), t=50.75, contours at ω=±1, ±10.**

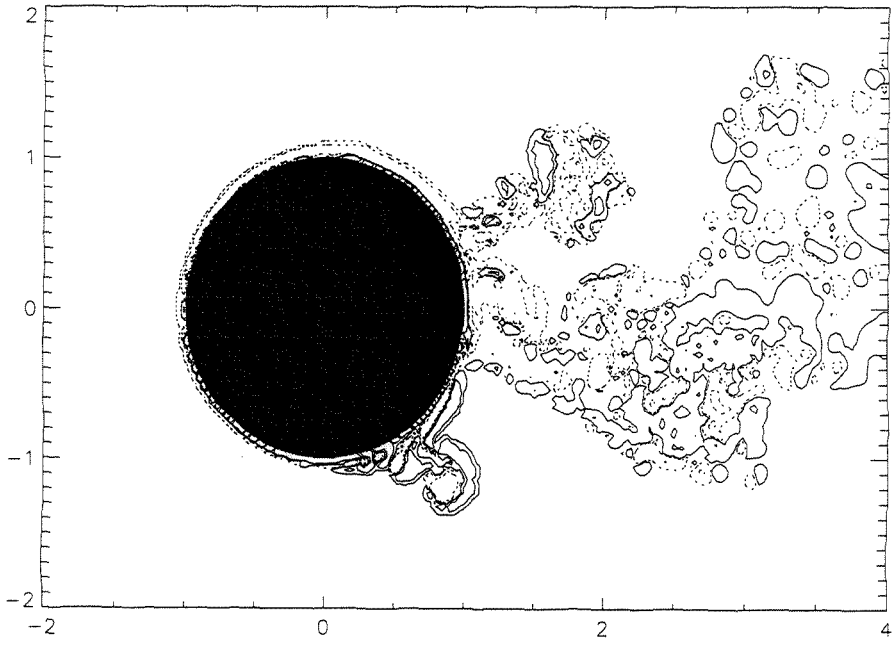


**Figure 100: Vorticity field for Re=15000 flow, Ω=2sin(πt), t=51, contours at ω=±1, ±10.**

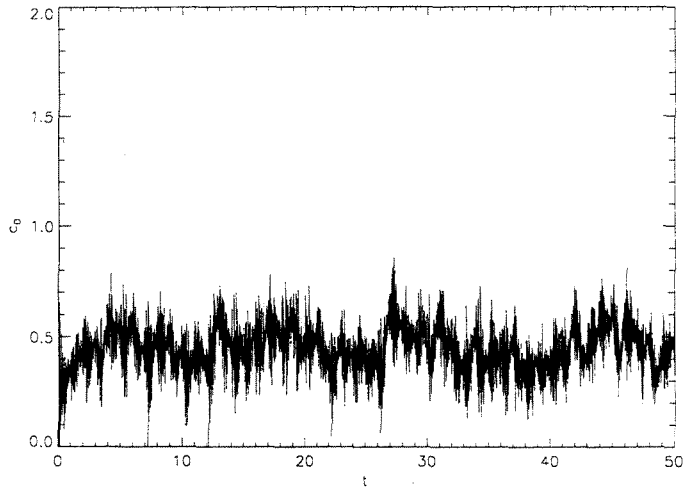


**Figure 101: Drag for Re=15000 flow, $\Omega=2\sin(\pi t)$.**

The drag is significantly reduced from the experimentally determined values for a fixed cylinder as seen in Figure 101. Averaged over five forcing cycles from t=40-50, the average drag coefficient is $c_D=0.43$. Although this is double the Tokumaru measurement, it represents nearly a 70 percent reduction in drag from the fixed cylinder measurements. Those measurements include three-dimensional effects, but the two-dimensional observations from the simulations capture the same qualitative behavior as Tokumaru's experiments and thus seem to reflect the behavior he observed.

Simulations with different forcing parameters were run to aid in assessing the mechanism driving the observed dynamics. If the proposed boundary layer instability is in fact driving the Re=15000, $\Omega=2\sin(\pi t)$ flow, modification to the amplitude and frequency should result in logical effects in the vorticity field.

First the amplitude of the oscillation was diminished to $\Omega=0.5\sin(\pi t)$. In this case the averaged drag coefficient rose to $c_D=1.42$. The vorticity field in Figure 102 reveals that vortex structures shed every step consist primarily of a single sign of vorticity. The wake exhibits a larger-scale vortex structure of positive vorticity immediately behind the body and one of negative vorticity a few diameters downstream in the wake. Thus the altered shedding seems to result in more classical wake development. The fact that the instability which drove the previous forced cases seems diminished here is consistent with its description in 4.2.4 as the smaller forcing amplitude results in a weaker shear layer near the boundary, thus inhibiting its growth.

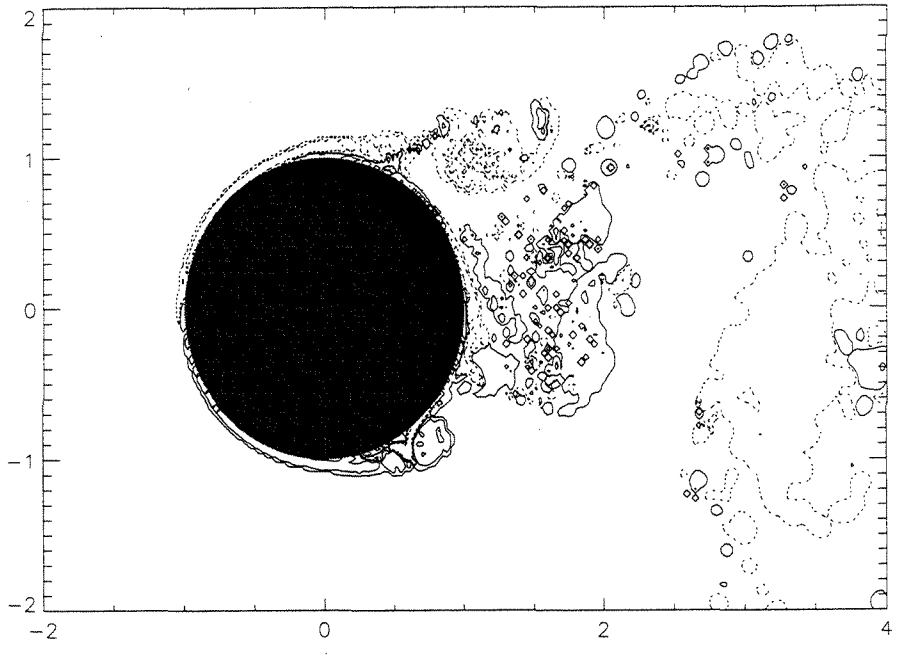


**Figure 102: Vorticity field for Re=15000 flow, Ω=0.5sin(πt), t=49, contours at ω=±1, ±10.**

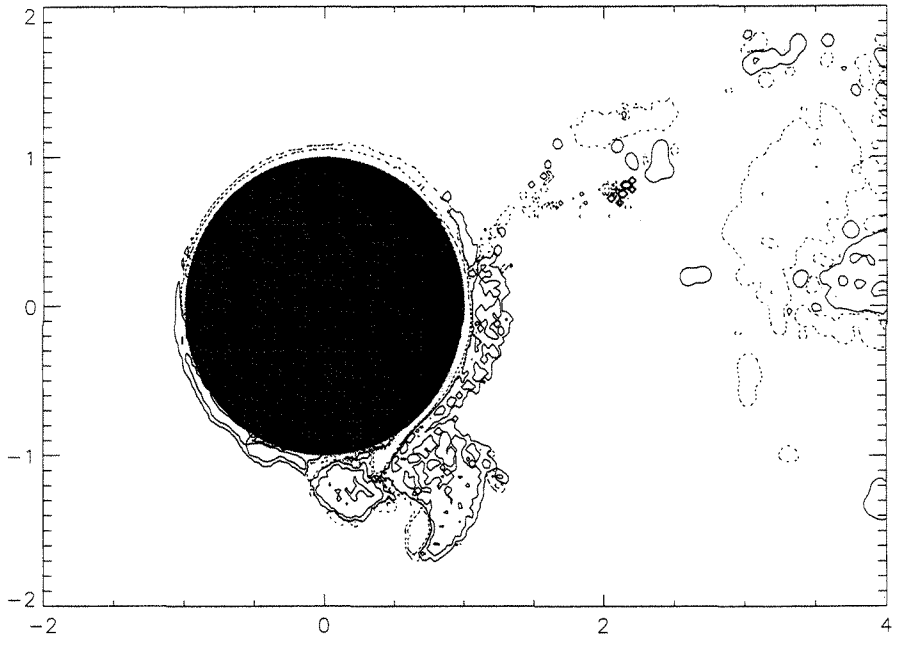


***Figure 103: Vorticity field for Re=15000 flow, Ω=2sin(0.5πt), t=48, contours at ω=±1, ±10.***

A second case lowers the frequency of the forcing to $\Omega=2\sin(0.5\pi t)$, resulting in a drag averaged over a single forcing cycle (t=40-48) of $c_D=1.14$. The plot of the vorticity field for this case in Figure 103 reveals that the instability observed in the other forcing cases no longer exists for this forcing. The large structure seen on the lower half of the cylinder is presumably the result of the clockwise rotation of the body from t=44-48, during which the body on the lower half moves in opposition to the freestream, enhancing separation as expected in classical thinking. In this case, the slower growth of the rotational amplitude could allow diffusion to reduce the shear layer that otherwise went unstable in the other two forcing cases above.

### 4.3.3 Reynolds Number Effects

The influence of Reynolds number effects on the observed drag reduction is assessed with a series of simulations using the forcing $\Omega=2\sin(\pi t)$ and identical simulation parameters to the above core expansion tests. Reynolds numbers in the range 150-15000 are considered, with only the spatial resolution varying as the viscosity adjusts in concert with the Reynolds number (the parameters cylinder radius R=1 and freestream U=1 are held constant as well). The results reveal that both the drag reduction and multipole vortex structures only exist at higher Reynolds numbers, and become more apparent as Reynolds number increases.

In order to reach the quasi-periodic state of these flows, simulations were run to t=50 (25 diameters of downstream motion) and averages were taken over five forcing cycles from t=40-50. The average drag coefficient thus measured in each case is given in Figure 104. At lower Reynolds numbers the forcing is ineffective and the decrease in drag simply parallels the known drop for the fixed cylinder (although for two-dimensional flow, fixed cylinder drag actually increases over the range Re=200-1000; cf - Henderson[1996]). But at the higher Reynolds numbers, clear drag reduction develops between the forced and fixed cases, increasing to the previously noted significant reduction for Re=15000.

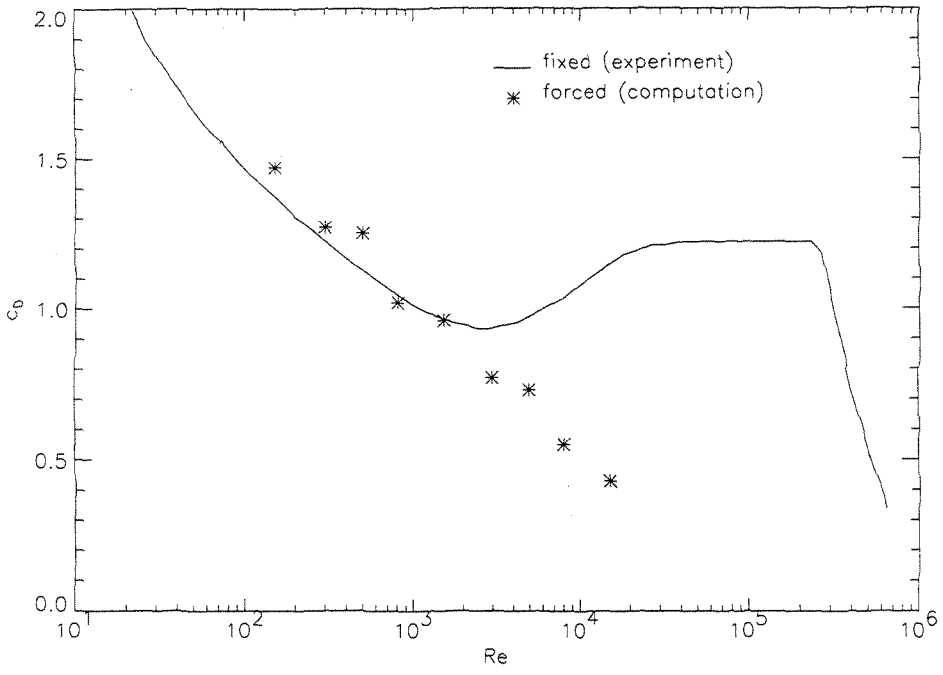


***Figure 104: Drag measured in two-dimensional simulations with $\Omega=2\sin(\pi t)$ (symbols) compared to experimental measurements of drag over a fixed cylinder ($\Omega=0$) (line) (Roshko[1961]).***

Views of the vorticity field at t=50, time-averaged streamlines, and time-averaged pressure give a good perspective on the foundation of the drag behavior. At t=50, a half-cycle of forcing with clockwise rotation has been completed and thus a vorticity structure such as that observed in the Re=15000 case has formed on the upper half of the cylinder. As the Reynolds number drops, the added diffusivity impedes the roll-up of this structure as seen in Figure 105 and prevents it from attaining the multipole nature evident at Re=15000. Between Re=1500 and 5000, the nature of the development of this structure clearly transitions, just as the drag reduction begins becoming significant in this range.

At the lower Reynolds numbers, these structures formed every half-forcing cycle could be characterized as the shedding of a slight dipole dominated by a single sign of vorticity. For Re=5000, the structure becomes clearly more complex. Note how the structure formed on the lower half of the cylinder from t=48-49 is drawn further from the body as Reynolds number increases. And note how at low Reynolds numbers the structures dominated by a single sign of vorticity tend to clump into large scale vortices in the wake, typical of natural vortex shedding. On the other hand, the mixed-sign,

multipole structures at the higher Reynolds numbers lead to a more heterogeneous near-wake dominated by smaller vortex structures. For example, note the large negative vorticity structure for Re=500 centered near x=3 and positive vorticity structure near x=7. On the other hand, alternating positive and negative structures can be discerned for Re=15000 from a positive structure at x=2 to a negative structure at x=8.

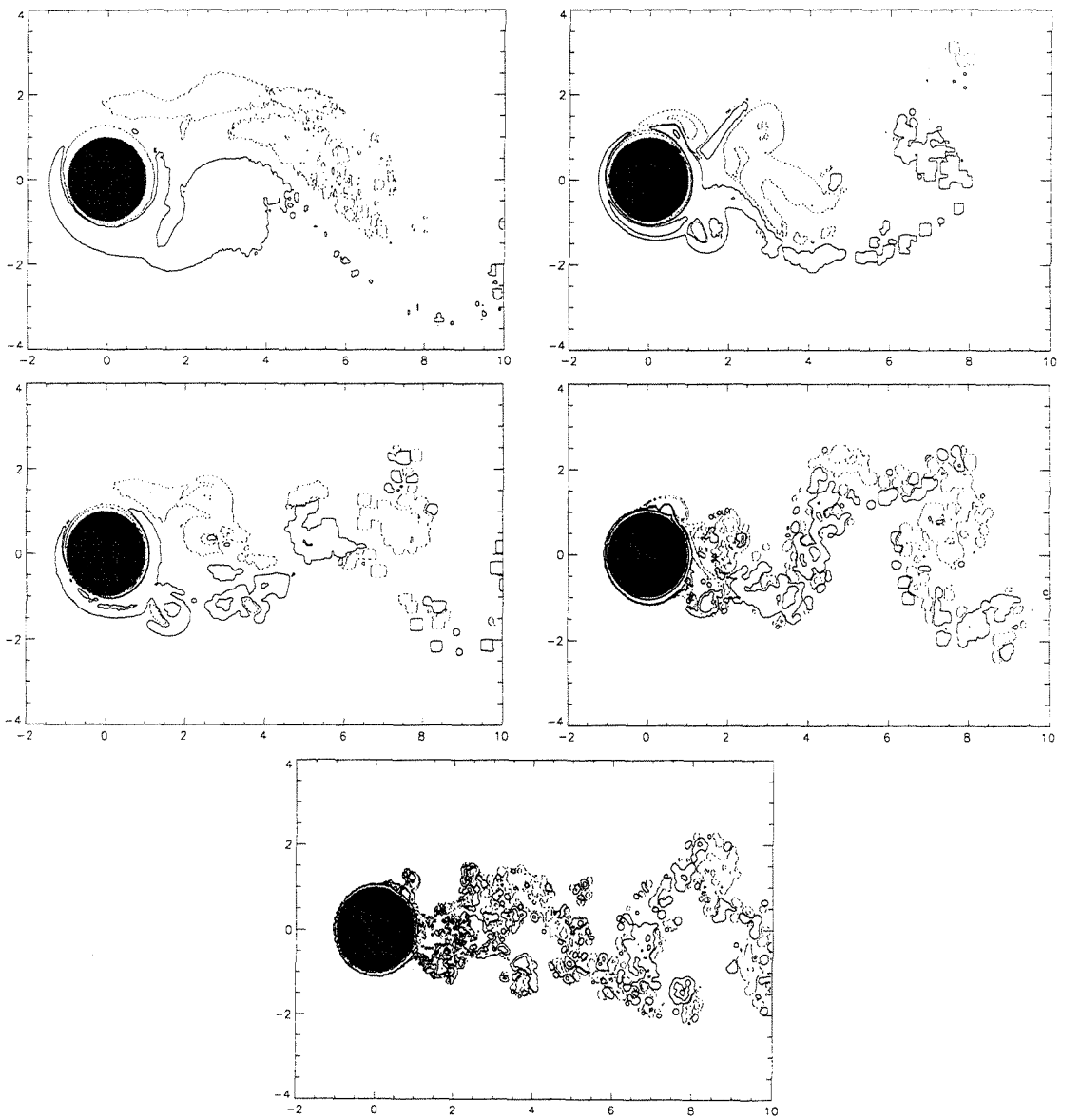

**Figure 105: Vorticity fields at t=50, $\Omega=2\sin(\pi t)$ for Re=150 (top left), 500 (top right), 1500 (middle left), 5000 (middle right), 15000 (bottom). Contours at $\omega=\pm 0.5, \pm 5$ with solid for positive, dashed for negative.**

**Figure 106: Color plots for Re=150 (top), Re=1500 (middle), and Re=15000 (bottom).**

The vortex dynamics can be seen as linked to a general trend of a delay in separation as Reynolds number increases, thus leading to drag reduction. The separation delay occurs in a cycle-averaged sense as obviously the rotation forces small-scale separation frequently. The time average pressure distributions in Figure 108 clearly show a pattern of separation delay as Reynolds number is increased. Time-averaged streamlines in Figure 107 verify that the flowfield does on average exhibit separation delay at the higher Reynolds numbers.

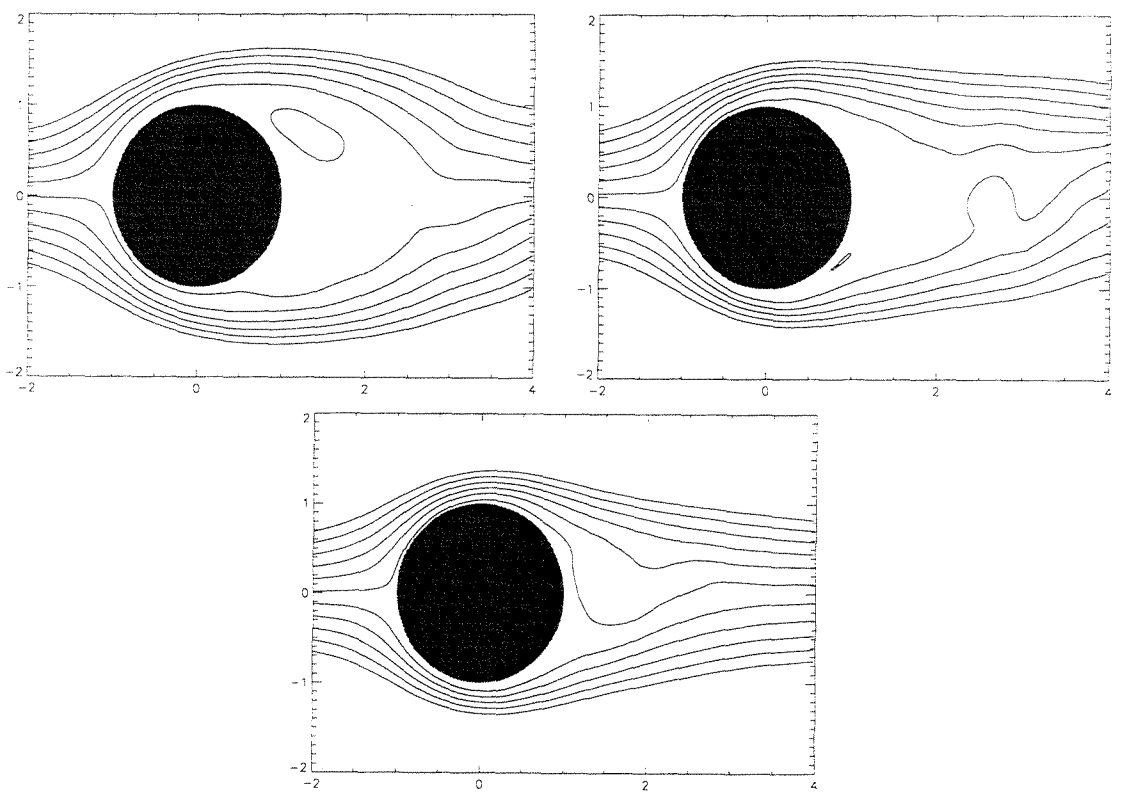

**Figure 107: Time-averaged streamlines, contours at ψ=0,±0.1, ±0.2, ±0.3, ±0.4, ±0.5. Re=500 (top left), 5000 (top right), 15000 (bottom).**

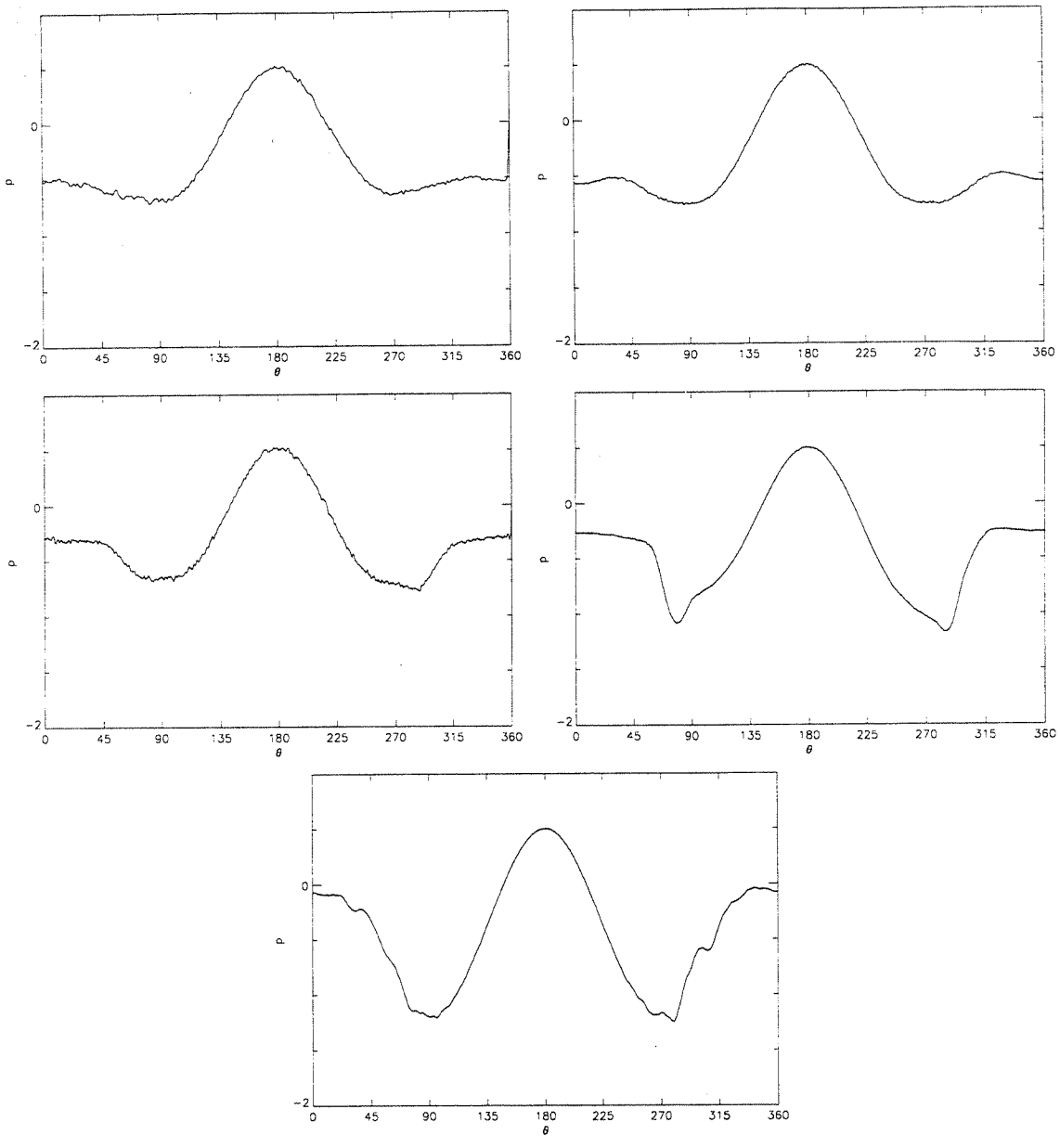


**Figure 108: Time-averaged pressure distributions with reference value $p(\theta=180^{o})=0.5$. Re=150 (top left), 500 (top right), 1500 (middle left), 5000 (middle right), 15000 (bottom).**

Observing the rotational forcing over a range of Reynolds numbers helps to clarify the physics behind measured drag reductions. The instability observed to grow in the boundary layer for the Re=15000 simulations encourages a delay in separation, presumably by a combination of destruction of vorticity through cancellation and convection of vorticity away from stagnation regions. As Reynolds number is decreased

and diffusivity increases, the instability is lessened, thus reducing its effects and leading to less drag reduction. An understanding of the dynamics behind the drag reduction also clearly indicates a laminar-to-turbulent boundary layer transition is not responsible for the lowered drag.

A final issue concerns the practical efficiency of control such as above. Although drag reduction can be obtained, there is a cost associated with rotating the cylinder against skin friction. A comparison is made between the power saved (which must be expended to move the body upstream) by the drag reduction and the power required to rotate the cylinder against skin friction. There is further cost in overcoming the rotational inertia of the body, but this is dependent on material properties and practical implementation and not factored into this analysis. Define the Power Savings Ratio, PSR, as the ratio between the power saved by drag reduction and power expended by the rotation. *The power saved by the drag reduction is given by*

$$\text{Power saved} = \left(\tfrac{1}{2}\rho U_\infty{}^2 D\Delta c_D\right)U_\infty = \tfrac{1}{2}\rho U_\infty{}^3 D\Delta c_D \tag{3.22}$$

The power exerted to rotate against skin friction is given by

$$\text{Power exerted} = \left(\rho U_\infty{}^2 R^2 c_M\right)\dot{\theta} \tag{3.23}$$

where the moment coefficient $c_M = -\frac{1}{Re}\left(\int_0^{2\pi} \omega d\theta - 4\pi\dot{\theta}\right)$ from Appendix A.

*Thus the Power Savings ratio PSR is given by*

$$PSR = \frac{\Delta c_D}{\left|\dot{\theta} c_M\right|} \tag{3.24}$$

where the denominator is time averaged as with the drag coefficient. Figure 109 shows that the process begins to greatly increase in efficiency as the Reynolds number rises to 15000.

In Table 1, a summary of the results from the long-time simulations with the core expansion method are provided.

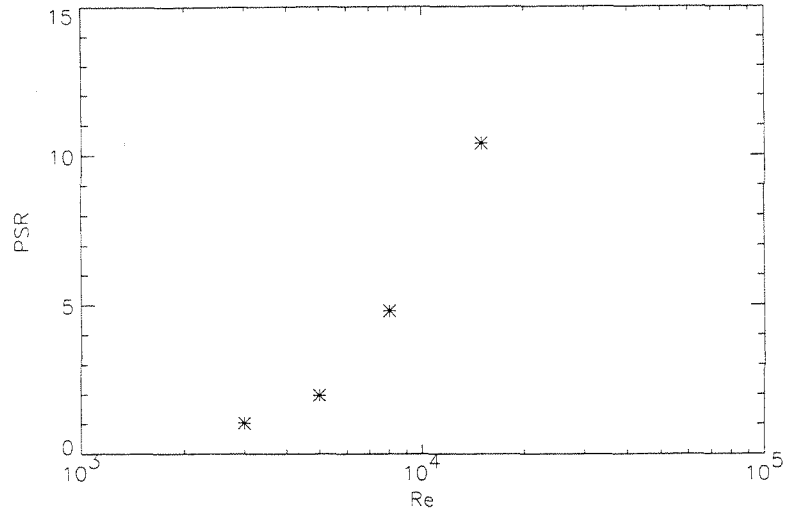


**Figure 109: The Power Saving Ratio (PSR) for cases in which drag was substantially reduced.**

| Re | Ω | $\overline{c_D}$ | $\overline{\dot{\theta}c_M}$ |
|---|---|---|---|
| 150 | 2sin(πt) | 1.47 | 0.84 |
| 300 | 2sin(πt) | 1.27 | 0.56 |
| 500 | 2sin(πt) | 1.25 | 0.42 |
| 800 | 2sin(πt) | 1.02 | 0.32 |
| 1500 | 2sin(πt) | 0.96 | 0.27 |
| 3000 | 2sin(πt) | 0.77 | 0.16 |
| 5000 | 2sin(πt) | 0.73 | 0.13 |
| 8000 | 2sin(πt) | 0.55 | 0.10 |
| 15000 | 2sin(πt) | 0.43 | 0.07 |
| 15000 | 0.5sin(πt) | 1.42 | 0.02 |
| 15000 | 2sin(0.25πt) | 1.14 | 0.03 |

**Table 4: Results for simulations with rotational forcing run to t=50 with the core expansion method.**

# 5 Summary

Extensions to vortex methods and applications to two circular cylinder flows have been presented in this thesis. The challenges posed by the complexity of the flows spurred development of the new vortex method techniques. Likewise, the new techniques made computations possible which illuminated aspects of the physics underpinning the flows. Although some of the flows could have been computed at least as easily with other methods, the high Reynolds number flow in Chapter 4 would be quite a challenge with any approach. In any case, the flow simulations provided a good opportunity to refine concurrently the rather unique and promising approach of vortex methods.

In Chapter 2, a clear delineation was made between the inviscid foundations of vortex methods and viscous modifications, as well as between features formulated for unbounded flow and modifications to account for boundaries. Some attention was focused on an existing particle strength exchange technique used for many of the simulations presented in this document. New extensions to the PSE method to simplify handling of the boundary condition and make long-time simulations possible were presented. More attention was focused on work to extend the core expansion concept into a practical viscous vortex method. The issue of how to implement localized remeshing (i.e., splitting and merging) was analyzed in-depth. One-dimensional analyses revealed the complexity of this issue due to the unpredictable, overlapping nature of the particle field. As a result, an empirical relation was determined for minimization of error in particle splitting. Various parameters were also defined to establish adaptive spatial resolution and techniques for incorporating a boundary with the core expansion approach. Test cases were used to guide selection of these parameters and verify that the resultant method was both accurate and convergent. With the core expansion implementation presented in this document, it appears that stable solutions which execute quite efficiently are possible if a bit of accuracy can be sacrificed. It seems that the core expansion technique can be easily adjusted to provide whatever balance is desired between accuracy and efficiency while remaining a grid-free method.

There are obviously many directions for the future development of vortex methods. Core expansion seems particularly appealing as it offers an efficient solution at a desired level of accuracy with a grid-free method. The study of core expansion in Chapter 2 can serve as a foundation to define issues which clearly have much room for refinement. In addition, it would be interesting to implement the method on a complex, possibly unsteady geometry (e.g.- a row of compressor blades, with flexibility allowed in the blades such as in the elastic cylinder study in Chapter 3) as a demonstration of its utility.

The study of a canonical flow induced vibration problem in Chapter 3 provided a new viewpoint for characterizing the behavior of this complex system. Simulations at limiting parameters helped to show that the lock-in description does not define the full behavior of the system. The computations suggested that the response in undamped systems can be well-defined by a single parameter termed the 'effective elasticity' by interpreting inertial forces as an anti-restoring force. It was shown that this parameter collapses responses in the current study far more effectively than the traditional parameter, the reduced velocity. The new results suggested that significant flow induced vibration requires a synchronization between admissible states of the wake and motions possible under the mechanical constraints. How this viewpoint can be reconciled with results interpreted as lock-in was also discussed. The effects of damping on system response and the 'effective elasticity' scaling were also investigated. Much more study is possible to test the new scaling ideas on other Reynolds numbers, a wider range of mechanical parameters, and with damping. The effects on these findings of allowing vibration inline with the freestream also should be determined.

The second set of simulations, in Chapter 4, dealt with flow over a circular cylinder executing rotary oscillation. Computations verified drag reduction observed experimentally by Tokumaru [1991]. The results show a clear correlation between delay in separation and the drag reduction. Study of the flow evolution revealed that the bursting of multipole vorticity structures from the boundary layer dictated the wake development for low-drag cases. It was shown that this critical phenomenon was linked to the generation of a free shear layer type of instability near the boundary layer, caused by the oscillatory motion of the body. Simulations sweeping over Reynolds numbers

from 150-15,000 indicated that this means of control only becomes effective and efficient at high Reynolds numbers as the instability can be suppressed by diffusivity. Computation up to Re=15,000 was highly challenging. It was shown that the simulations presented capture the behavior accurately enough to be confident that the dominant flow structures are properly resolved, though the accuracy at smaller scales is in doubt. Future work on this problem, as well as attempting to achieve even higher resolution, should address a much wider range of the available control parameters (as was done in the experimental work) to fully characterize the system.

# A Measuring Forces with a Vortex Method

The fluid force on a rigid body is well known to be a combination of pressure and skin friction. Below this relationship is developed, indicating where modifications are required for more exotic situations such as a boundary with suction or blowing. The means by which this relationship can be recast from primitive variables into those available in vortex method simulations is also outlined. Alternatives are presented which have strengths and weaknesses depending on the application.

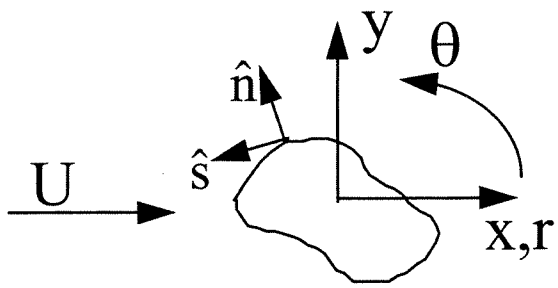


For a general bluff body as diagrammed above, the force $\underline{F}$ can be expressed in terms of stresses on the body as

$$\underline{F} = \oint [\sigma_{nn}\hat{n} + \sigma_{ns}\hat{s}]ds \tag{4.1}$$

The normal stress can be expressed instead in terms of the pressure

$$\sigma_{nn} = -p + 2\mu e_{nn} \qquad \text{where } e_{ij} \text{ is the strain tensor and } \mu = \text{viscosity} \tag{4.2}$$

which for incompressible flow reduces to

$$\sigma_{nn} = -p \qquad (\text{for incompressible flow, } e_{nn} + e_{ss} = 0;\ \text{for a rigid body } e_{ss} = 0) \tag{4.3}$$

The shear stress can also be expressed in terms of the fluid straining

$$\sigma_{ns} = 2\mu e_{ns} \tag{4.4}$$

yielding

$$\underline{F} = \oint [-p\hat{n} + 2\mu e_{ns}\hat{s}]ds \tag{4.5}$$

for the force on a rigid body in incompressible flow.

Non-dimensionalizing with the freestream U and a body length scale L and including the fluid density ρ and viscosity ν gives

$$\frac{\underline{F}}{\frac{1}{2}\rho U^2 L} = c_D\hat{x} + c_L\hat{y} = -2\oint p^*\hat{n}ds^* + \frac{4}{Re}\oint\left(e_{nn}{}^*\hat{n} + e_{ns}{}^*\hat{s}\right)ds^* \tag{4.6}$$

$$\text{where: } p^* = \frac{p}{\rho U^2},\ s^* = \frac{s}{L},\ e_{ns}{}^* = \frac{e_{ns}L}{U},\ Re = \frac{UL}{\nu}$$

Similarly, the moment on the body can be expressed as

$$M = \oint\left[-p\hat{n} + 2\mu e_{ns}\hat{s}\right]\cdot\hat{\theta}rds \tag{4.7}$$

where r is the distance from the point about which the moment is being taken. This relation non-dimensionalizes to

$$\frac{M}{\frac{1}{2}\rho U^2 L^2} = c_M = -2\oint\left[p^* r^*\left(\hat{n}\cdot\hat{\theta}\right)ds^*\right] + \frac{4}{Re}\oint\left[e_{ns}{}^* r^*\left(\hat{s}\cdot\hat{\theta}\right)\right]ds^* \tag{4.8}$$

Specializing to a circular cylinder and using the cylinder radius R for the length scale (L=R),

$$\hat{n} = \cos\theta\hat{x} + \sin\theta\hat{y} \qquad \hat{s} = \hat{\theta} = -\sin\theta\hat{x} + \cos\theta\hat{y} \qquad ds = Rd\theta$$

$$e_{ns}{}^* = \frac{\omega^*}{2} - \frac{u_\theta{}^*}{r^*} + \frac{\partial u_r{}^*}{r^*\partial\theta} \tag{4.9}$$

For a rigid body,

$$u_\theta \neq f(\theta) \text{ and } \frac{\partial}{\partial\theta} = 0$$

Pressure is difficult to obtain based on knowledge of the velocity and vorticity fields and thus in vortex methods one wishes to recast the pressure term. This is done by relating the pressure integral to an integral involving the pressure gradient and then substituting from the incompressible momentum equation as follows

$$\oint\left[p^* R\left(\cos\theta\hat{x} + \sin\theta\hat{y}\right)\right]d\theta = p^* R\left(\sin\theta\hat{x} - \cos\theta\hat{y}\right)_0^{2\pi} - \oint\left[\frac{\partial p^*}{\partial\theta}R\left(\sin\theta\hat{x} - \cos\theta\hat{y}\right)\right]d\theta \tag{4.10}$$

$$\frac{\partial p^*}{\partial\theta} = \frac{1}{Re}\frac{\partial\omega^*}{\partial r^*} + f_\theta{}^* - a_{rel,\theta}{}^* - \frac{\partial u_\theta{}^*}{\partial t^*} - u_r{}^*\frac{\partial u_\theta{}^*}{\partial r^*} - u_\theta{}^*\frac{\partial u_\theta{}^*}{\partial\theta^*} - u_r{}^* u_\theta{}^* \tag{4.11}$$

Using the rigid body simplifications discussed above and another rigid body characteristic, $u_r$=0, with f representing body forces and $a_{rel}$ being the acceleration of the reference frame,

$$c_D = \frac{2}{Re}\oint\left(\frac{\partial\omega^*}{\partial r^*} - \omega^*\right)\sin\theta d\theta \quad + \quad \oint\left(f_\theta{}^* - a_{rel,\theta}{}^*\right)\sin\theta d\theta \tag{4.12}$$

$$c_L = -\frac{2}{Re}\oint\left(\frac{\partial\omega^*}{\partial r^*} - \omega^*\right)\cos\theta d\theta \quad - \quad \oint\left(f_\theta{}^* - a_{rel,\theta}{}^*\right)\cos\theta d\theta \tag{4.13}$$

Similarly applying the moment coefficient to the circular cylinder geometry yields

$$c_M = \frac{1}{Re}\oint\omega^* d\theta \quad - \quad \frac{4\pi\Omega^*}{Re} \tag{4.14}$$

where $\Omega$ gives the rotational motion of the cylinder. For simulations such as discussed in the main text where the cylinder is intended to move through a still fluid but the computation uses a freestream over a fixed cylinder, the reference frame does have a relative acceleration, yielding

$$c_D = \frac{2}{Re}\oint\left(\frac{\partial\omega^*}{\partial r^*} - \omega^*\right)\sin\theta d\theta \quad + \quad \oint f_\theta \sin\theta d\theta - \pi\dot{U}^* \tag{4.15}$$

for drag and a similar expression when the body accelerates transverse to the freestream such as in Chapter 3. Note that this expression assumes a vorticity field was created using the freestream U, thus detecting the vortex sheet which forms on the surface due to acceleration. Some discussion on this issue is given in Chapter 3. The vorticity gradient in these expressions can be obtained through the vortex sheet strength as outlined in Chapter 2. This measurement technique was used for the simulations in Chapters 2-4. For historical reasons, this technique will be referred to as Method B.

Another approach, fully formulated by Noca [1996], expresses the forces only in terms of the vorticity and velocity field and their derivatives and does not require values at the surface of the body. This can be advantageous both for under-resolved computations and modern experimental techniques such as DPIV which currently have difficulty resolving boundary layers. Noca's approach involves doing a momentum balance on a control volume enclosing the body, yielding the forces on the interior boundary (i.e., the body) based on values in the volume and on its outer boundary. Please refer to the various references from Noca [1996] and Noca et al., [1997] [1998] for the variety of expressions possible, including one which requires only knowledge of values on the chosen outer boundary.

A general form of the relations derived by Noca, which shall be referred to as Method C, is

$$\underline{F} = -\frac{d}{dt}\int_{V(t)+V_b(t)} \underline{x}\times\omega\hat{z}dV + \int_{V(t)+V_b(t)} \underline{u}\times\omega\hat{z}dV - \oint_{S(t)}\left[\hat{n}\cdot(\underline{u}-\underline{u}_s)(\underline{x}\times\omega\hat{z})\right]dS$$
$$+ \frac{d}{dt}\int_{V_b(t)} \underline{u}dV + \oint_{S(t)}\left[\hat{x}\times\left(\hat{n}\times\left(\nabla\cdot\underline{\underline{T}}\right)\right)\right]dS + \oint_{S(t)}\left[\hat{n}\cdot\underline{\underline{T}}\right]dS \qquad (4.16)$$

where V is the control volume, S is its outer boundary, $\underline{u}_s$ is the velocity of surface S, $V_b$ is the body, and T is the viscous stress tensor. Although this relation appears complex, all quantities are readily available in vortex methods. Furthermore, it avoids the need to compute the vorticity gradient on the body, which can be problematic if resolution is lacking. Noca also provides many other convenient forms of this expression.

One major simplification is to extend the outer surface S to infinity. Noca showed how this can lead to the expression for forces

$$\underline{F} = -\frac{d}{dt}\int_{V(t)+V_b(t)} \underline{x}\times\omega\hat{z}dV + \frac{d}{dt}\int_{V_b(t)} \underline{u}dV \qquad (4.17)$$

Again for historical reasons this approach will be termed Method A. This method has been widely utilized in past vortex method studies. The terms involved are readily available and it does not involve the vorticity gradient, which can be difficult to resolve. The fact that it requires summation over the entire vorticity field is acceptable since vortex methods require the entire field in any case. However, Method A proves inaccurate when the far wake is resolved coarsely and thus is not compatible with attempts to reduce the computational cost of vortex methods. For a translating body which is computed in a body fixed frame with a freestream, the drag can be simply expressed with Method A as

$$c_D = -\frac{d}{dt^*}\iint y^*\omega^* d\underline{x}^* - \pi\dot{U}^* \qquad (4.18)$$

In order to test the accuracy of Methods A, B, and C, the drag and lift measured from a simulation of Re=392 flow over a circular cylinder that also oscillates transverse to the freestream according to $Y^*(t^*)=2\sin(2\pi t^*/13)$ are shown in Figure 110. The three methods clearly exhibit good agreement. The 'gridded' results also given are for measurement with Method C, but on a fixed grid rather than by following the particle

grid as is done for the dashed line case. This primarily impacts calculation of the time derivatives. Fixed grid calculation is tested as that is the approach with DPIV data. The resolution of this grid was dx=0.016 radii in a computation with dt=0.015.

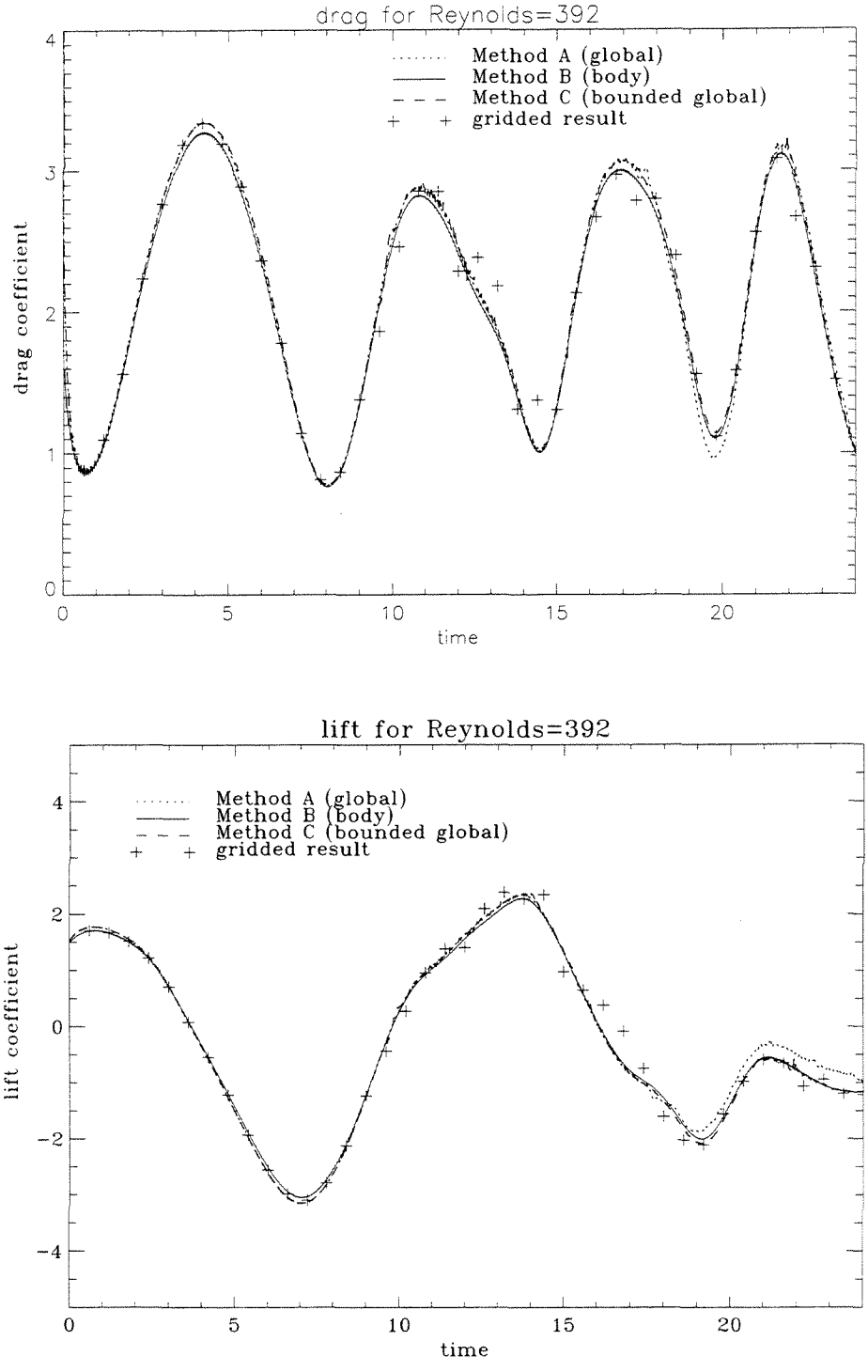


**Figure 110: Drag (top) and lift (bottom) for Re=392 flow with transverse oscillation.**

The control volume used for the application of Method C to Re=392 flow is given along with the vorticity field at $t^*$=24 in Figure 111.

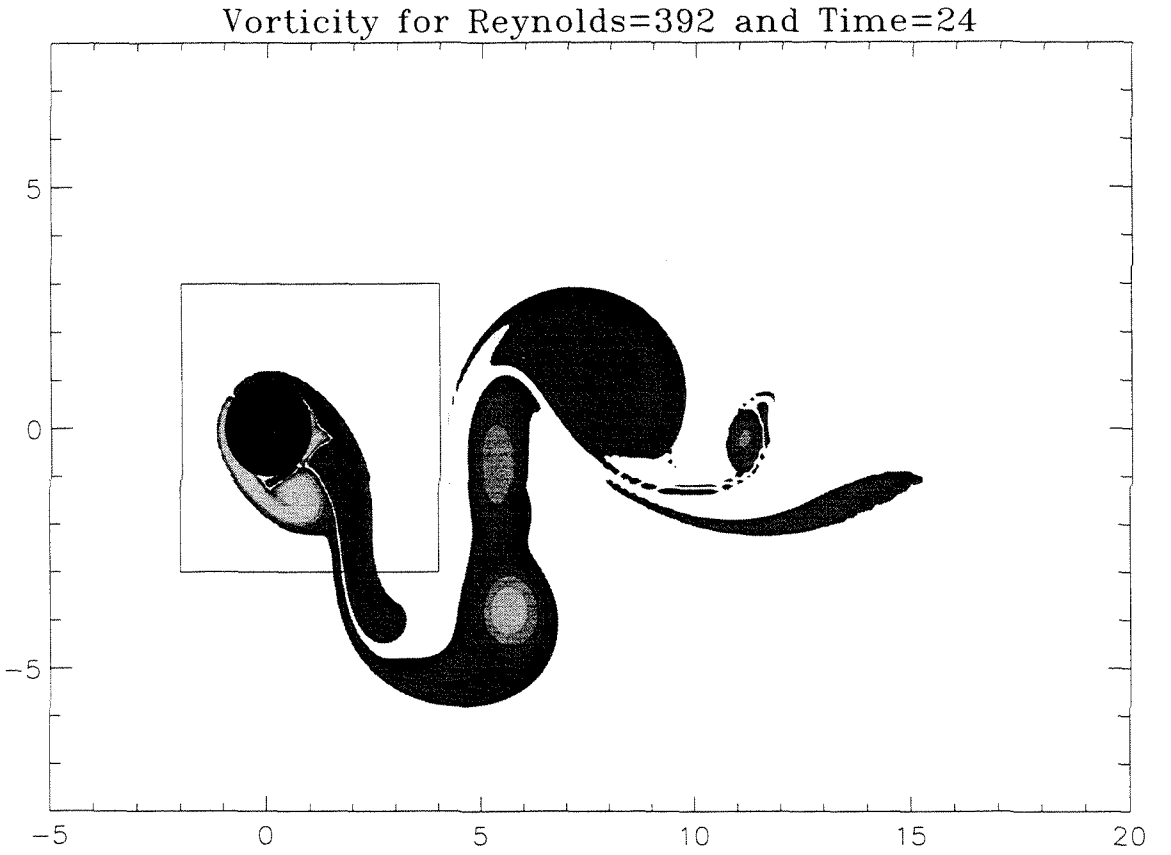


**Figure 111: Vorticity field for Re=392 flow over transversely oscillating cylinder at $t^*$=24. The box defines the surface S used in the Method C computation of forces.**

# B Flat Plate Simulations

Flow over an infinitesimally-thin flat plate is a special case in which the vortex sheet used to satisfy the boundary condition can be determined directly, rather than requiring a panel method, as discussed in Chapter 2. For details on this issue, see Koumoutsakos et al., [1996]. This problem has been structured to allow time dependent motion of the body in both translational directions and with rotation.

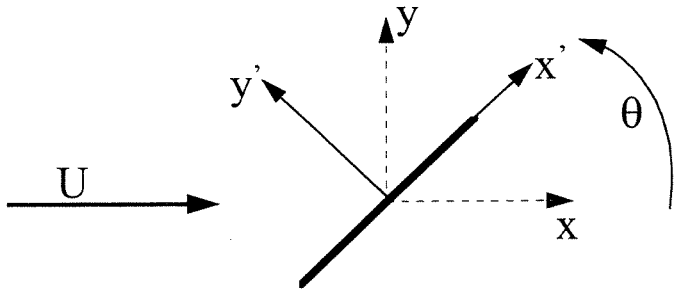


**Figure 112: Layout for flow over an infinitely thin flat plate. The length scale L=plate length.**

The forces on the plate can be obtained with the methods in Appendix A, though various terms differ due to the body geometry. The pressure is again related to the tangential derivative of pressure, which in this case is a cartesian component for an incompressible flow

$$\frac{\partial p^*}{\partial x'^*} = -\frac{1}{Re}\frac{\partial \omega^*}{\partial y'^*} + f_{x'}^* - a_{rel,x'}^* - \frac{\partial u_{x'}^*}{\partial t} - u_{x'}^* \frac{\partial u_{x'}^*}{\partial x'^*} - u_{y'}^* \frac{\partial u_{x'}^*}{\partial y'^*} \tag{5.1}$$

where non-dimensionalization uses the freestream U and the plate length L. Assumption of a solid body requires

$$u_{x'}^* = 0 \qquad u_{y'}^* = x'^* \Omega^* \qquad \frac{\partial u_{x'}^*}{\partial y'} = \Omega^* - \omega^* \qquad \frac{\partial u_{x'}^*}{\partial t^*} = -x'^* \Omega^{*2} \qquad e_{y'x'} = \Omega - \frac{\omega^*}{2}$$

where $\Omega$ is the rotation rate. The pressure gradient on the body thus becomes

$$\frac{\partial p^*}{\partial x'^*} = -\frac{1}{Re}\frac{\partial \omega^*}{\partial y'^*} + f_{x'}^* - a_{rel,x'}^* + x'^* \omega^* \Omega^* \tag{5.2}$$

Now define the convention that (+) refers to the side of the body y'>0 and (-) refers to y'<0. The force decomposed as

$$\frac{\underline{F}}{\frac{1}{2}\rho U^2 L} = c_f \hat{x}' + c_p \hat{y}' \tag{5.3}$$

thus becomes

$$c_P = 2\int_{-\frac{1}{2}}^{\frac{1}{2}} \left[ \frac{1}{Re}\left( \frac{\partial \omega^*}{\partial y'^*}(-) - \frac{\partial \omega^*}{\partial y'^*}(+) \right) + x'^* \Omega^* \left( \omega^*(+) - \omega^*(-) \right) \right] x'^* dx'^* \tag{5.4}$$

$$c_f = \frac{2}{Re}\int_{-\frac{1}{2}}^{\frac{1}{2}} \left( \omega^*(-) - \omega^*(+) \right) dx'^* \tag{5.5}$$

Similarly, the coefficient for moment about the center of the plate can be expressed as

$$c_M = 2\int_{-\frac{1}{2}}^{\frac{1}{2}} \left[ \frac{1}{Re}\left( \frac{\partial \omega^*}{\partial y'^*}(-) - \frac{\partial \omega^*}{\partial y'^*}(+) \right) + x'^* \Omega^* \left( \omega^*(+) - \omega^*(-) \right) \right] x'^{*2} dx'^* \tag{5.6}$$

Note that for the flat plate the moment derives from the pressure force whereas for the cylinder it derives from the skin friction. The vorticity gradients can be related to the sheet strength based on the same relation used for the cylinder. Forces from the Method B and C perspectives are independent of the body geometry and thus the relations used in Appendix A are valid except for the terms accounting for the acceleration of the reference frame (fluid forces on an infinitely thin plate are not effected by reference frame acceleration).

Various test cases have been run with the PSE method in order to compare with theoretical and experimental results on this problem. A flat plate at zero angle-of-attack (i.e., aligned with the freestream) is a fundamental problem as it provides the development of a simple boundary layer. Triple deck theory predicts the steady drag coefficient for this configuration (Messiter [1970], Stewartson [1974]) to be

$$c_D = \frac{2.656}{Re^{\frac{1}{2}}} + \frac{5.336}{Re^{\frac{7}{8}}} \tag{5.7}$$

The results with the vortex method for Re=500 flow over a plate with $\theta$=0 are given in Figure 113 and seen in good agreement with the triple deck prediction.

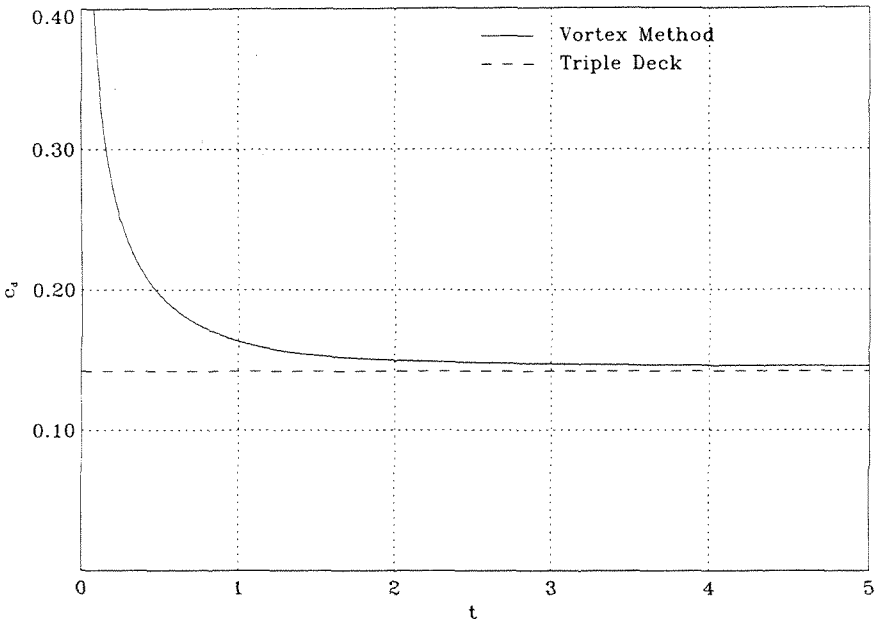


**Figure 113: Comparison of vortex method simulation and triple deck prediction for the drag at Re=500, θ=0.**

Flow visualization of starting flow over flat plates at relatively low Reynolds numbers can also be used to validate the flat plate code. Some validations are provided in Chapter 2 and more are given in the figures below. In Figure 115, the discrepancy between the experimental and computational results may be attributable to blockage becoming a factor as the flow develops in the experiment. As noted in Chpater 2, the experiments measure pathlines rather than streamlines, but over the time of exposure these flows apparently are not significantly unsteady.

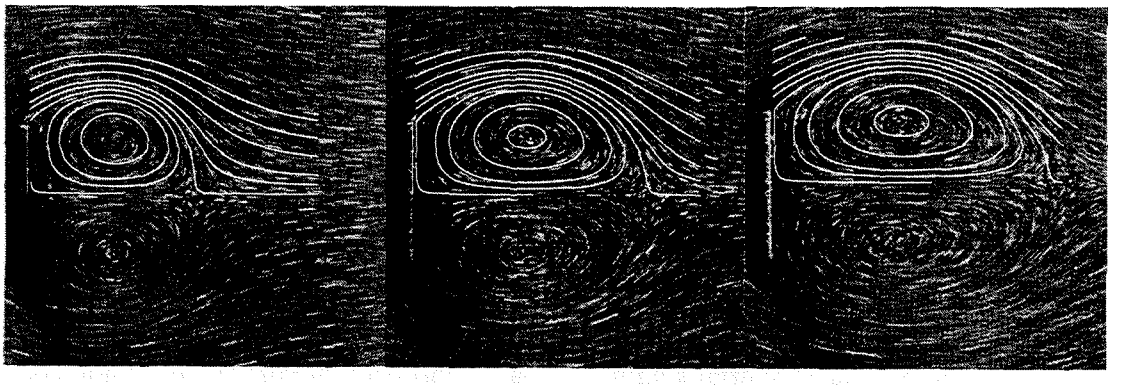

**Figure 114: Flow visualization of Re=126 flow with θ=90° from Taneda et al., [1971] with streamlines from the vortex method computation overplotted on the upper half. The times plotted are t=1.45 (left), t=2.56 (middle), and t=3.37 (right).**

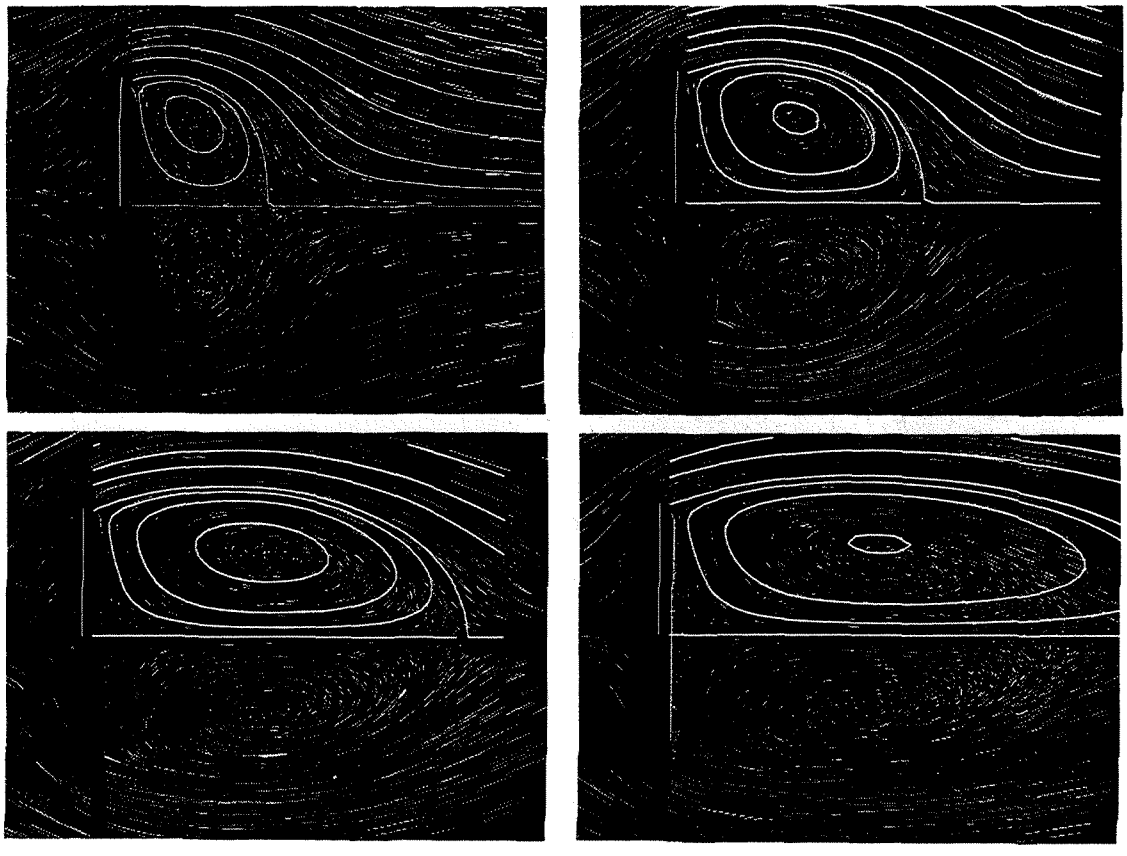

**Figure 115: Flow visualization of Re=20 flow with θ=90° from Dennis et al., [1993] with streamlines from the vortex method computation overplotted on the upper half. The times plotted are t=0.5 (upper left), t=1.0 (upper right), t=2.0 (lower left) and t=4.0 (lower right).**

An interesting problem is an unconstrained flat plate in a field of uniform acceleration (e.g., in a gravitational field). Depending on the Reynolds number and plate characteristics, such a free-falling flat plate will experience a rocking motion due to the unsteady forces and can begin rotating if the rocking develops a large enough amplitude. This phenomenon is called 'autorotation'. This topic and efforts to model it have been reviewed by Lugt [1983].

Using the coordinate system above, taking the gravitational field to act in opposition to the freestream direction U, and defining a term to relate the fluid parameters to the body mass $m_p$

$$\alpha = \frac{\rho L}{m_p} \tag{5.8}$$

The equations of motion for the plate, non-dimensionalized by plate length L and a term related to the terminal velocity $U_{tv}$, become

$$\ddot{x}^* = \alpha\left(\tfrac{1}{2}c_D - 1\right) \tag{5.9}$$

$$\ddot{y}^* = \tfrac{\alpha}{2}c_L \tag{5.10}$$

$$\ddot{\theta}^* = 6\alpha c_M \tag{5.11}$$

where

$$U_{tv} = \sqrt{\frac{m_p g}{\rho}} \tag{5.12}$$

Thus the system is governed by the choice for $\alpha$ and the terminal velocity term (which plays the role of a non-dimensionalized gravitational field). In study of flow over a free-falling disk, Willmarth et al., [1964] found that their observations on freely falling disks were well scaled by a term similar to $\alpha$ which they introduced as a dimensionless moment of inertia and a Reynolds number defined by the terminal velocity. The above analysis shows the roots of their observations as these terms govern the dimensionless equations of motion.

In order to compute a free-falling flat plate, one needs to use the apparent mass as in Chapter 3 to properly update the accelerations of the body. For the flat plate, the apparent mass $m_A=\pi/2$ for non-dimensionalization by plate length. The apparent mass is used for linear acceleration. The apparent inertia that could likewise be associated with rotational acceleration $I_A$ is given by $I_A=\pi/64$. Reliable means have not been found to obtain the moment coefficient with Methods B and C from Appendix A and thus Method A must be used as given above.

A simulation of a free-falling plate using the particle strength exchange (PSE) method is demonstrated in Figure 116. Initially the plate falls without significant rotation as the wake grows symmetrically. Eventually asymmetry develops and the plate begins rocking, which builds to the end of this simulation. The plate was given a small additional rotation at t=10 to trigger development. Another case without this triggering also developed to this state, but more slowly.

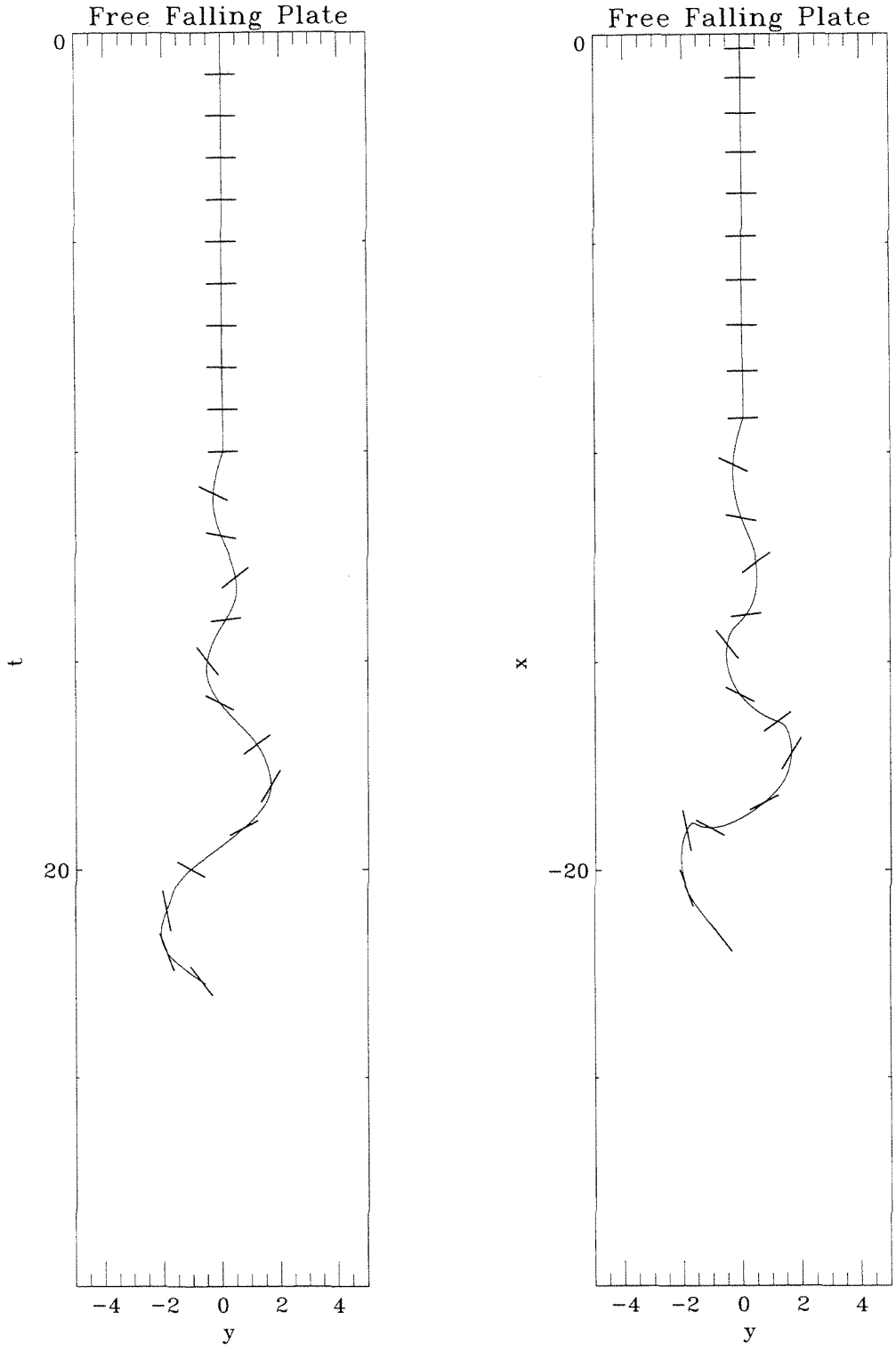


**Figure 116: Trajectory history of a free falling flat plate for Re=100 (based on $U_{tv}$=1) and $I^*$=0.033. Trajectory in y-t space at left and y-x space at right (the gravitational field points in -x).**

# C Computational Details

High-resolution simulation taxes available computational resources. Thus efficiency in implementation was an important issue for the methods described in Chapter 2. Simulations in this thesis were primarily run on Cray vector supercomputers (C90, YMP, J90). For this reason, the code is written in FORTRAN as the C compilers are not know to be as efficient on the Crays. The code used for simulations was extended from the code used in Koumoutsakos [1993]. Many adjustments were made to improve the maintainability of the code (such as moving from implicit to explicit variable declaration) and Cray-specific routines were removed so that the code uses only standard FORTRAN77 functions and thus is easily portable to a wide range of platforms. A parallel version of the particle strength exchange (PSE) code was developed with Dr. Alan Stagg of Cray Research for use on the Cray T3D platform. The CRAFT programming model was used for the parallel implementation.

The general structure for the code is outlined by the flow chart in Figure 117. The work defined in box B of the flowchart dominates the computational cost for simulations with many particles N. As discussed in Chapter 2, direct discretization for this step implies an $O(N^2)$ cost for the method. However, options exist to reduce the cost to $O(N\log_2 N)$ or $O(N)$ by using approximations in this step. The bulk of the code and greatest algorithmic complexities come from implementation of these 'fast' techniques.

The $O(N^2)$ technique involves a simple, nested loop.

```
loop i over all particles
   loop j over all particles (j≠ i)
      compute velocity induced by j at i
      if PSE, compute exchange from j to I
   endloop
endloop
```

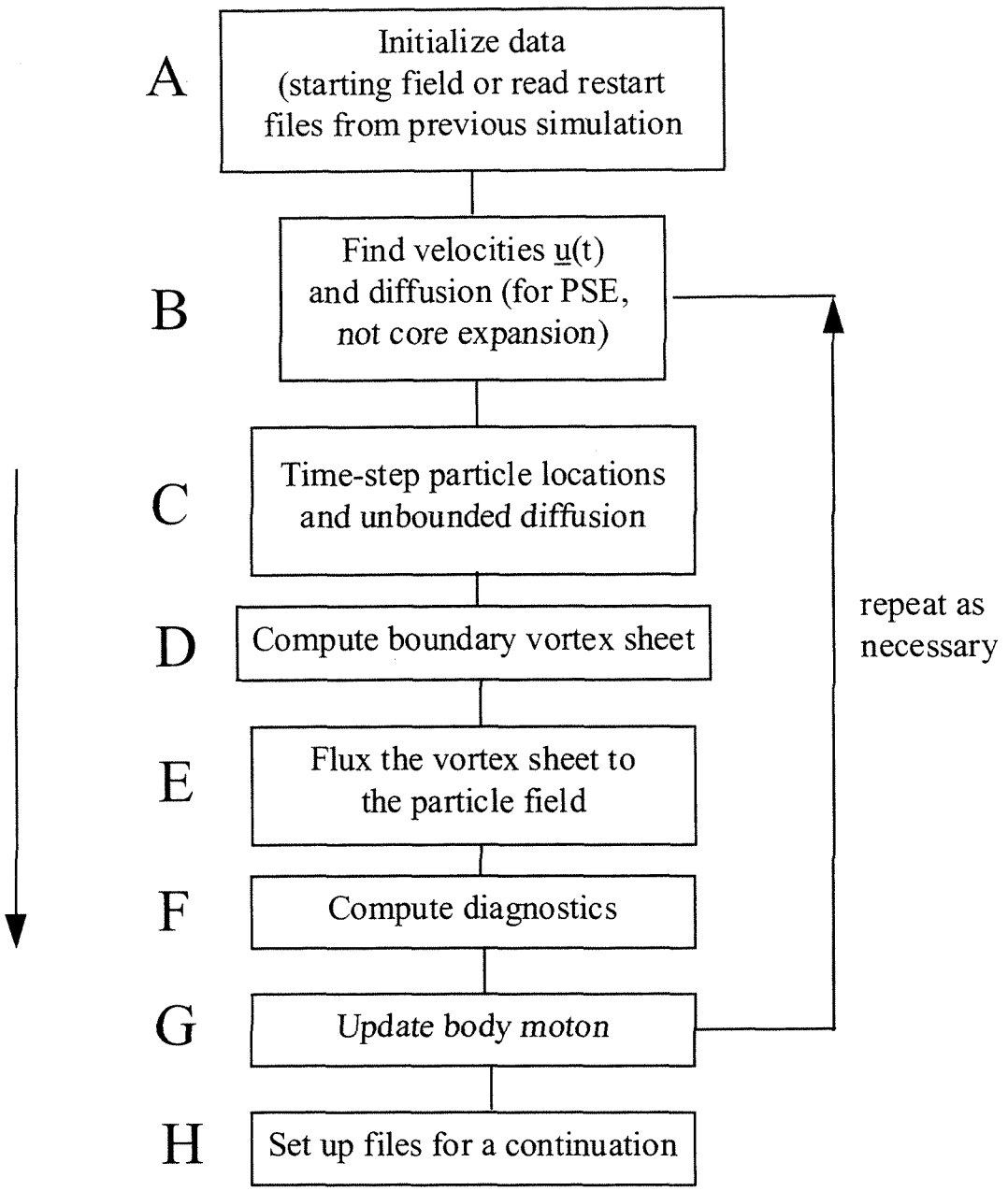


**Figure 117: Flowchart of vortex method code.**

In the $O(N\log_2 N)$ technique, particles that are 'distant' from the location at which data is desired can be pre-grouped and sums over such particles can be reduced to summation over the groups. The size of the group depends on just how 'distant' the particles are. The cost for summation over the field can be thus reduced from O(N) to $O(\log_2 N)$, with the overall cost based on the need to do N such summations. In order for the method to be efficient, these groupings need to be pre-defined once for a given set of

data and re-used for all N summations. A convenient method is to build a quad-tree for the data, in which groups govern a square region of space and parent groups get subdivided into four child groups. This subdivision is done recursively and criteria need to be defined to determine the finest level of subdivision. This issue is discussed further below. The $O(N\log_2 N)$ method thus involves building the tree and then determining in the inner loop of the summation at what level of the tree to interact.

```
loop i over all particles to set coarsest tree levels
recursively loop tree levels down to finest levels
loop i over all particles
   loop over tree at coarsest level
      recursively descend tree until appropriate
                level reached and interact at that level
       if finest level is too 'close', loop over all its particles j and
                interact with them
   endloop
endloop
```

The O(N) technique achieves further savings through a more complex adjustment where the summation count is reduced below N by allowing distant group influence to be determined once in a region at a point P and subsequently distributed to particles 'near' P. Essentially, it reduces the cost of the outer loop of the $O(N^2)$ method just as the $O(N\log_2 N)$ technique reduced the cost of the inner loop while keeping the inner loop savings. The O(N) technique thus allows box-box interactions as well as the particle-box interactions introduced with the $O(N\log_2 N)$ approach and the particle-particle interactions which characterize $O(N^2)$.

```
loop i over all particles to set coarsest tree levels
recursively loop tree levels down to finest levels
loop i box levels from coarsest to finest
        loop j over boxes at this level i
                step (*): find appropriate boxes and interact
                        either box-box or particle-particle
        endloop
endloop
loop all boxes to transfer interactions from boxes to particles
```

The implementation of step(*) is somewhat complex. For a box M with children, interaction should only be considered with the children of neighbors of box M's parent. Neighbors are the boxes (up to 8) adjoining (including diagonally) a box. Once a childless level is reached, if a box-box interaction is not possible, then particle-particle must be used. This technique assures that all interactions are properly accounted for.

One method of generating the quad-tree is to define a single parent of square geometry at the coarsest level and thus make subdivision at each level identical. Refer to this as the 'square-top' approach. Memory can be assigned for all possible boxes (irregardless of particle distribution) to permit some algorithmic simplifications. However, the memory requirements of such a method can become excessive. A limit needs to be set on the maximum number of levels allowed as memory increases by a factor of 4 for each finer level added. For example, consider the memory cost of such a tree code, given in Table 5. Furthermore, the square geometry at the coarsest level does not adapt well to the vorticity fields typical of wake flows.

| Number of levels in tree | Memory requirement |
|---|---|
| 7 | 8 MB |
| 8 | 20 MB |
| 9 | 80 MB |
| 10 | 320 MB |

**Table 5: Memory usage for 'square-top' tree implementation.**

An alternate technique has been developed using a rectangle of integer aspect ratio at the coarsest level, so that subdivision differs at the coarsest level from all other levels. Call this the 'rectangular-top' approach. An example of the advantage is seen in Figure 118, where the finest level contains boxes which cover much less area, and have fewer particles, because the boxes on the coarsest level cover much less area. This alternative technique was also implemented such that memory is only assigned for a fixed number of boxes on each level, which can be chosen as far less than the maximum possible total. Dynamic memory allocation is avoided because it is not standard FORTRAN77 and thus would hinder code portability. This combination of a more

adaptive coarsest level and user-controlled allocation of maximum boxes on a level removes memory constraints as an issue since the simulation speed becomes the clear bottleneck.

The tree subdivision is constrained by requiring a parent box to have a minimum number of particles $N_{par,min}$. In other words, a box is not allowed to subdivide into four children if it does not contain a minimum number of particles. The effects of this parameter can be seen in Figure 119. Rigorous study has not been undertaken on this parameter, but ad hoc testing suggests $N_{par,min}=60$ is a robust choice to balance memory usage and execution efficiency for the 'square-top'. On the other hand, $N_{par,min}=10$ strikes a good balance for the 'rectangular-top' method, as the memory requirements are lessened with this approach to the quad-tree.

The accuracy constraints listed in Chpater 2 concerning how coarse a level can be utilized for interaction are further effected by the fact that box dimensions at the finest level must remain distinctly larger than the core extents of particles in the box. Figure 120 reveals the effects on quad-tree decomposition of differing uniform core size. This becomes especially important with the core expansion method due to the relative unpredictability of core sizes.

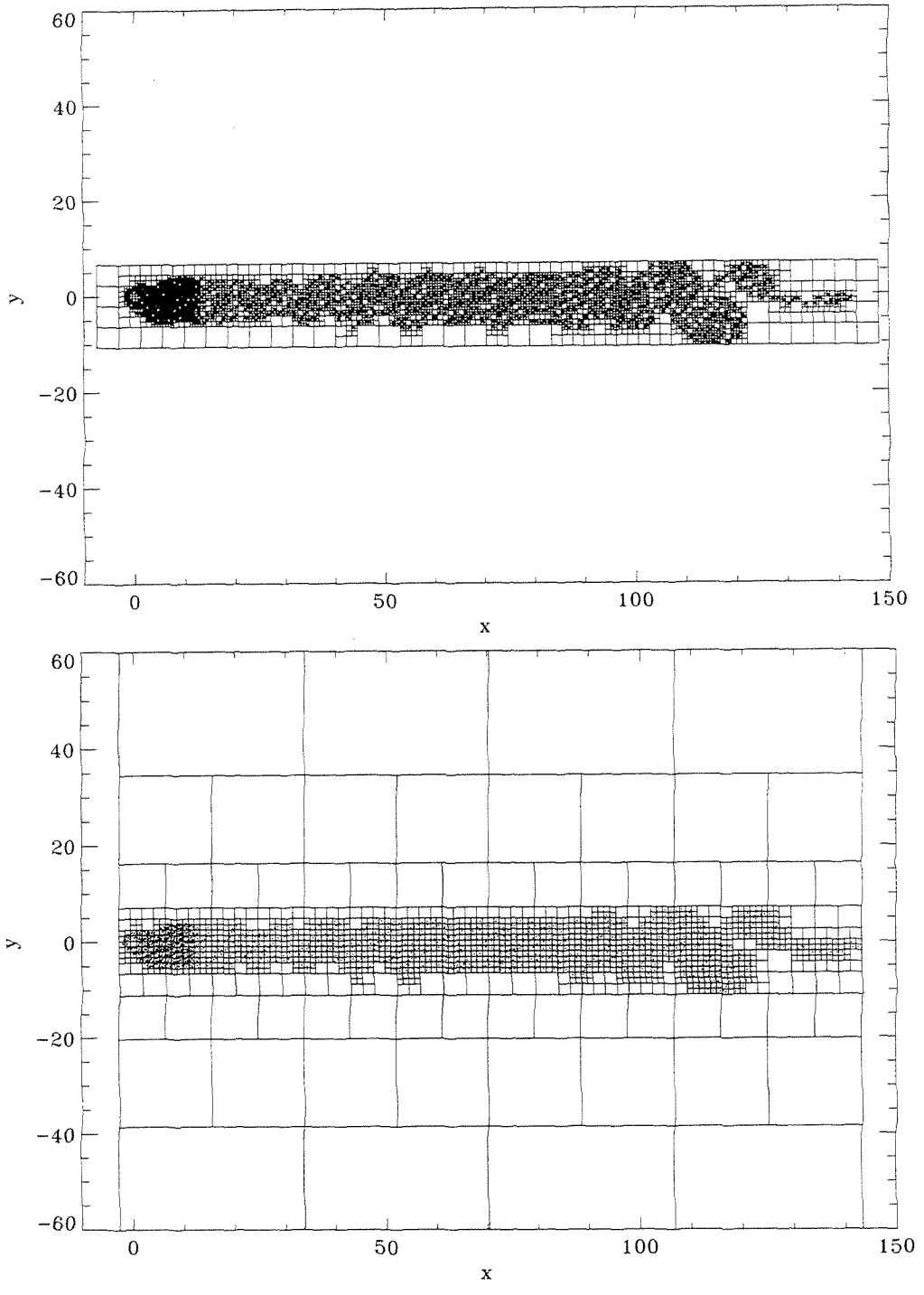


**Figure 118: Tree subdivisions of the vorticity field for flow over a cylinder. At top the 'rectangular-top' method is applied to 7 levels and at bottom the 'square-top' approach is applied to 7 levels.**

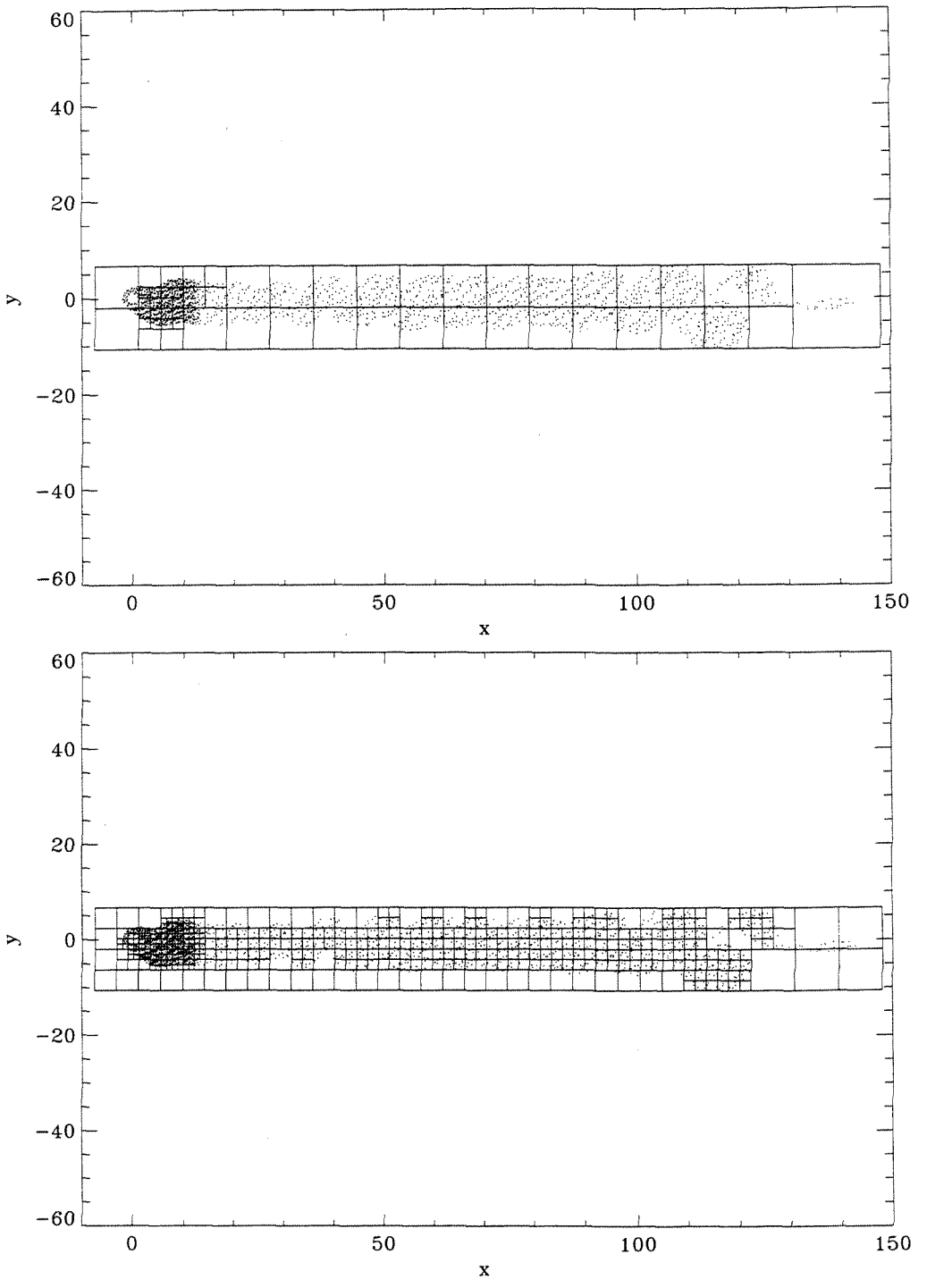


**Figure 119: Tree subdivision of particle field with $N_{par,lim}$=100 (top) and $N_{par,lim}$=10 (bottom).**

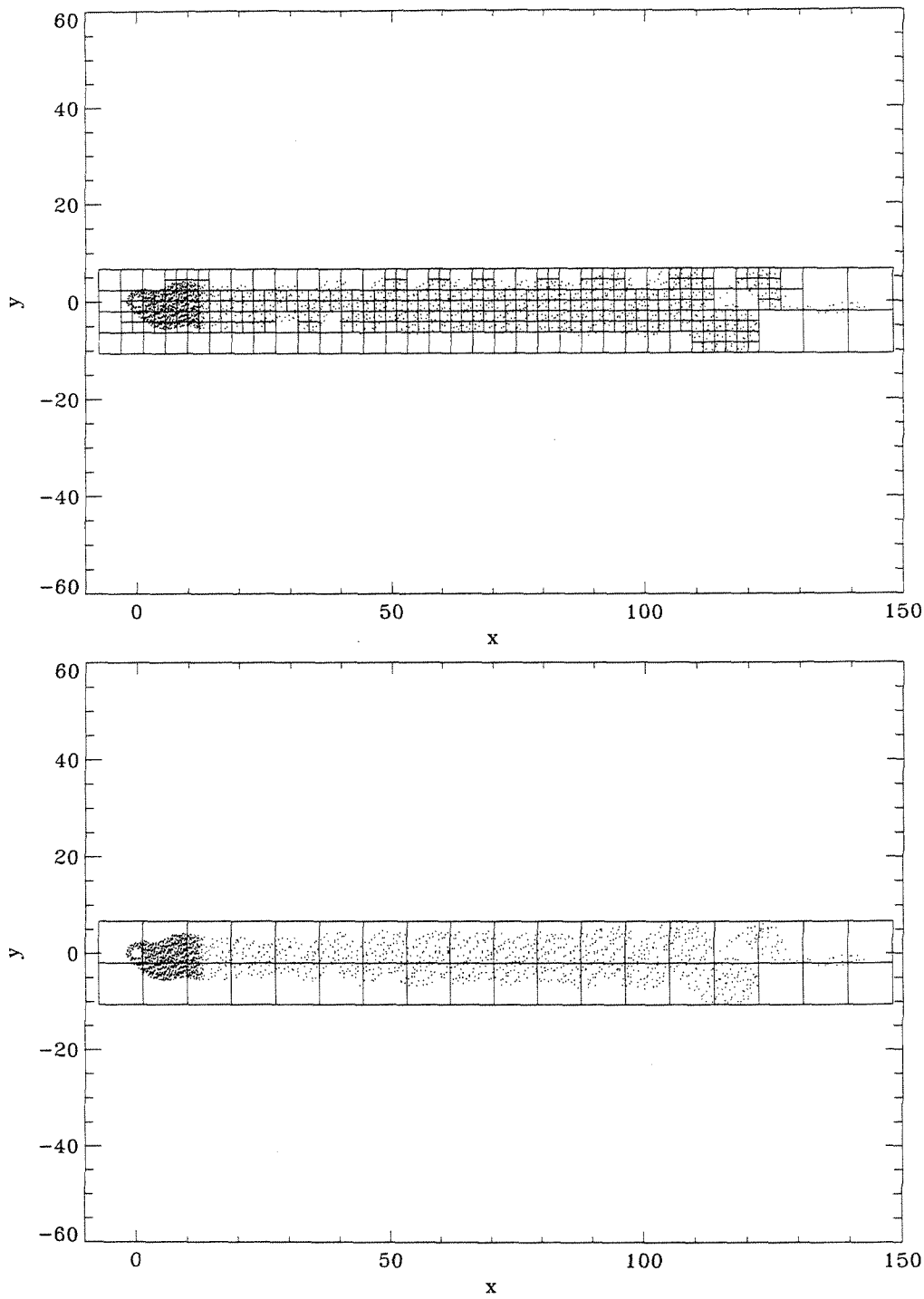


**Figure 120: Tree subdivision of particle field with smaller σ(top) and larger σ(bottom).**

As the particle count grows to levels typical of high-resolution computation, the O(N) technique becomes clearly preferable. Table 6 shows that as particle count increases, the O(N) method is distinctly more efficient. Note that the $O(N^2)$ method is the most efficient in terms of MFlops (Millions of Floating Point Operations Per Second), but not simulation speed. This is because the MFlops measure of efficiency is degraded in the O(N) case by quad-tree construction. Similarly the $O(N\log_2 N)$ approach performs the most MIPS (Millions of Instructions Per Second) because it must recursively descend the quad-tree far more often than with the O(N) scheme. On the other hand, in the PSE simulations using the 'square-top' tree, the O(N) method requires 140 MB, whereas the $O(N\log_2 N)$ requires 60 MB and the $O(N^2)$ requires 20 MB.

| Particles | Method | CPU time | MFlops | MIPS |
|---|---|---|---|---|
| 7000 | $N^2$ | 167 | 200 | 16 |
| 7000 | $N\log_2 N$ | 91 | 91 | 33 |
| 7000 | N | 56 | 102 | 24 |
| 10000 | $N^2$ | 269 | 209 | 15 |
| 10000 | $N\log_2 N$ | 134 | 96 | 33 |
| 10000 | N | 78 | 119 | 22 |
| 15000 | $N^2$ | 1106 | 215 | 15 |
| 15000 | $N\log_2 N$ | 378 | 82 | 38 |
| 15000 | N | 163 | 112 | 25 |
| 22500 | $N^2$ | 2306 | 219 | 15 |
| 22500 | $N\log_2 N$ | 619 | 87 | 38 |
| 22500 | N | 260 | 132 | 22 |
| 45000 | $N\log_2 N$ | 9348 | 108 | 36 |
| 45000 | N | 1733 | 135 | 23 |

**Table 6: Characteristics of simulations using different summation techniques.**

The code has been implemented on various platforms, with typical simulations on a Cray J90 executing 60 MFlops and on a CrayYMP executing 120 Mflops for the O(N) PSE code. A relative scaling of computational speed is given in Table 7.

| Platform | Speed Factor (lowest=fastest) |
|---|---|
| Cray C90 | 1 |
| Cray YMP | 1.75 |
| Cray J90 | 3.5 |
| Pentium Pro 200 MHz | 7 |
| SGI R8000 | 7 |
| SGI R4000 | 15 |
| SPARC5 | 25 |

**Table 7: Relative code speed on assorted platforms.**

To make some assessment of the parallel code efficiency, one time step of the Re=15000 case simulated in Chapter 4 with the $O(N\log_2 N)$ method is run at $t=5$, at which point there are 1.7 million particles involved, yielding the results in Table 8. Although the simulations run faster when many T3D processors are available, the scalability degrades as the number of processors increases.

| Situation | CPU speed (sec.) |
|---|---|
| $O(N\log_2 N)$ on the T3D (256 processors) | 340 |
| O(N) on the T3D (256 processors) | 170 |
| O(N) on the T3D (128 processors) | 200 |
| O(N) on the T3D (64 processors) | 310 |
| O(N) on the T3D (32 processors) | 527 |
| O(N) on the C90 | 860 |

**Table 8: Performance of the parallel code.**

A final note concerns the importance of properly conserving circulation in the flowfield. For the PSE method, circulation conservation is not insured by the method of fluxing the vortex sheet to the existing particle field. Various types of corrections can be attempted. One correction measures the net circulation error $\Delta\Gamma$ and cancels it by distributing equal fractional amounts of $-\Delta\Gamma$ to particles near the body. Call this approach 'global correction'. Another approach is to correct for each panel's flux error by making weighted corrections to nearby particles based on the fraction of the panel's strength each particle was supposed to receive. Call this approach 'weighted correction'. A final technique is to make equal corrections to each vortex sheet panel to cancel any observed error in net circulation. Term this method 'sheet correction'. As seen in Figure 121, it is important to correct for net circulation error. The 'weighted correction' attacks the true root of error and its similarity to the related 'sheet correction' suggest these techniques are accurate. Note, though, that the 'global correction' can be significantly in error.

The issues discussed in this section could all be examined in a more thorough manner in future work to achieve optimum efficiency, though perhaps more immediate benefit would result from refinement of the core expansion method. Unlike the PSE method, where the cost is dominated by computation of particle-particle interactions, the core expansion method requires virtually equal time for these interactions, the particle merging step, and building of the quad-tree. The subroutine for merging might be a particularly ripe candidate for improvement.

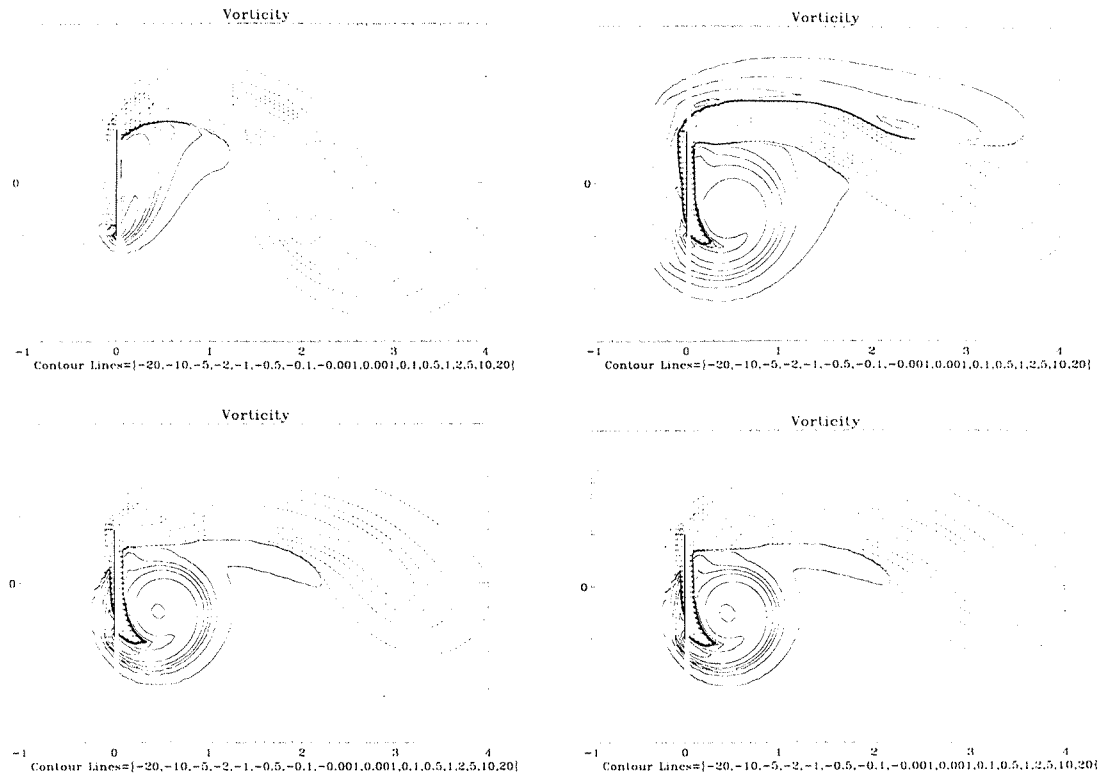


**Figure 121: Vorticity field for flow over a rotating flat plate (Re=200, t=3.14, Ω=0.5). The plate is parallel to the freestream at t=0. Methods used to correct for error in conservation of net circulation are: none (upper left), 'global correction' (upper right), 'weighted correction' (lower left), 'sheet correction' (lower right).**

# 6 References

Anderson, C., and Greengard, C., [1985]. On Vortex Methods. *SIAM J. Numer. Anal.*, **22**, 413.

Beale, J., and Majda, A., [1985]. High Order Accurate Vortex Methods with Explicit Velocity Kernels. *J. Comput. Phys.* **58**, 188.

Bender, C., and Orszag, S., [1978]. *Advanced Mathematical Methods for Scientists and Engineers*, McGraw-Hill.

Blackbrun, H., and Henderson, R., [1996]. Lock-in Behavior in Simulated Vortex-Induced Vibrations. *Exp. Therm. And Fluid Sci.*, **12,** 184.

Chang, C., and Chern, R., [1991]. A Numerical Study of Flow Around an Impulsively Started Circular Cylinder by a Deterministic Vortex Method. *J. Fluid Mech.*, **233**, 243.

Chorin, A.J., [1973]. Numerical Study of Slightly Viscous Flow. *J. Fluid Mech.* **57**, 785.

Degond, P., and Mas-Gallic, S., [1989]. The Weighted Particle Method for Convection-Diffusion Equations. Part 1: The Case of an Isotropic Viscosity. *Math. Comput.* **188**, 485.

Dennis, S.C.R., Qiang, W., Coutanceau, M., and Launay, J-L., [1993]. Viscous Flow Normal to a Flat Plate at Moderate Reynolds Numbers. *J. Fluid Mech.* **248**, 605.

Feng, C., [1968]. *The Measurement of Vortex-Induced Effects in Flow Past Stationary and Oscillating Circular and D-Section Cylinders*, M.A.Sc. thesis, University of British Columbia.

Fishelov, D., [1990]. A New Vortex Scheme for Viscous Flows. *J. Comput. Phys.* **86**, 211.

Gad-el-Hak, M., and Bushnell, D., [1991]. Separation Control: Review. *J. Fluids Eng.*, **113**, 5.

Gharib, M., Shiels, D., Gharib, M., Leonard, A., and Roshko, A., [1997]. Exploration of Flow-Induced Vibration at Low Mass and Damping, *ASME Fourth International Symposium on Fluid-Structure Interaction, Aeroelasticity, Flow-Induced Vibration, and Noise, Dallas, TX, Nov.16-21.*

Goodman, J., Hou, T., and Lowengrub, J., [1990]. Convergence of the Point Vortex Method for the 2-D Euler Equations. *Comm. Pure Appl. Math.*, **43**, 415.

Greengard, C., [1985]. The Core Spreading Vortex Method Approximates the Wrong Equation. *J. Comput. Phys.*, **61**, 345.

Hammache, M., and Gharib, M., [1991]. An Experimental Study of the Parallel and Oblique Vortex Shedding From Circular Cylinders. *J. Fluid Mech.*, **232**, 567.

Henderson, R., [1995]. Details of the Drag Curve Near the Onset of Vortex Shedding. *Phys. Fluids*, **7**, 2102.

Hou, T., and Lowengrub, J., [1990]. Convergence of the Point Vortex Method for the 3-D Euler Equations. *Comm. Pure Appl. Math.*, **43**, 965.

Khalak, A., and Williamson, C., [1996]. Dynamics of a Hydroelastic Cylinder with Very Low Mass and Damping. *J. Fluids Struct.*, **10**, 455.

Koopmann, G., [1967]. The Vortex Wakes of Vibrating Cylinders at Low Reynolds Numbers, *J. Fluid Mech.*, **28**, 501.

Koumoutsakos, P., [1993]. *Direct Numerical Simulations of Unsteady Separated Flows Using Vortex Methods*, Ph.D. thesis, Caltech.

Koumoutsakos, P., and Leonard, A., [1995]. High-Resolution Simulations of the Flow Around an Impulsively Started Cylinder Using Vortex Methods. *J. Fluid Mech.*, **296**, 1.

Koumoutsakos, P., Leonard, A., and Pepin, F., [1994]. Boundary Conditions for Viscous Vortex Methods. *J. Comput. Phys.* **113**, 52.

Koumoutsakos, P., and Shiels, D., [1996]. Simulations of the Viscous Flow Normal to an Impulsively Started and Uniformly Accelerated Flat Plate. *J. Fluid Mech.* **328**, 177.

Leonard, A., [1980]. Vortex Methods for Flow Simulation. *J. Comput. Phys.* **37**, 289.

Leonard, A., [1985]. Computing Three-Dimensional Incompressible Flows with Vortex Elements. *Ann. Rev. Fluid Mech.*, **17**, 523.

Leonard, A., [1997]. Large-eddy Simulation of Chaotic Convection and Beyond. *AIAA Paper 97-0204.*

Leonard, A., Koummoutsakos, P., and Winckelmans, G., [1994]. Vortex Methods for Three-Dimensional Separated Flows. *Proceedings of the Fourteenth International Conference on Numerical Methods in Fluid Dynamics, Bangalore, India.*

Lugt, H., [1980]. Autorotation. *Ann. Rev. Fluid Mech.*, **15**, 123.

Maheo, P., Gharib, M., and Henderson, R., [1995]. Start-up Flow Past a Circular Cylinder: A Comparison Between DPIV and DNS. *Proceedings of the Seventh International Symposium on Flow Visualization, Seattle, WA, Sept.*

Marshall, J.S., and Grant, J.R., [1995]. A Lagrangian Collocation Method for Vorticity Transport in Viscous Fluid Flows. *Proceedings of the Forum on Vortex Methods for Engineering Applications, Albuquerque, NM, Feb. 22-24.*

Messiter, A., [1970]. Boundary Layer Flow Near the Trailing Edge of a Flat Plate. *SIAM J. Appl. Math.*, **18**, 241.

Milinazzo, F., and Saffman, P.G., [1977]. The Calculation of Large Reynolds Number Two-Dimensional Flow Using Discrete Vortices with Random Walk. *J. Comput. Phys.* **23**, 380.

Noca, F., [1996]. *On the Evaluation of Instantaneous Fluid-Dynamic Forces on a Bluff Body*, GALCIT Report FM96-5.

Noca, F., Shiels, D., and Jeon, D., [1997]. Measuring Instantaneous Fluid Dynamic Forces on Bodies, Using Only Velocity Fields and their Derivatives, *J. Fluids Struct.*, **11**, 345.

Noca, F., Shiels, D., and Jeon, D., [1998]. Measuring Instantaneous Fluid Dynamic Forces on Bodies, Using Only Velocity Fields and their Derivatives, *J. Fluids Struct.*, submitted.

Parkinson, G., [1989]. Phenomena and Modeling of Flow-Induced Vibrations of Bluff Bodies, *Prog. Aerospace Sci.*, **26**, 169.

Pepin, F., [1990]. *Simulation of the Flow Past an Impulsively Started Cylinder Using a Discrete Vortex Method*, Ph.D. thesis, Caltech.

Roshko, A., [1954]. On the Drag and Shedding Frequency of Two-Dimensional Bluff Bodies. *NACA TN 3169.*

Roshko, A., [1961]. Experiments on the Flow Past a Cylinder at Very High Reynolds Number. *J. Fluid Mech.*, **10**, 345.

Rossi, L., [1996]. Resurrecting Core Spreading Vortex Methods: A New Scheme That is Both Deterministic and Convergent. *SIAM J. Sci. Comp.*, **17**, 370.

Rossi, L., [1997]. Merging Computational Elements in Vortex Simulations. *SIAM J. Sci. Comput.*, **18**, 1014.

Sarpkaya, T., [1989]. Computational Methods With Vortices - The 1998 Freeman Scholar Lecture. *J. Fluids Eng.* **111**, 5.

Schmall, R., and Kinney, R., [1974]. Numerical Study of Unsteady Viscous Flow Past a Lifting Plate. *AIAA Journal* **12**, 1566.

Spalart, P., [1982]. *Numerical Simulation of Separated Flows*. Stanford Ph.D. thesis.

Spalart, P., [1988]. Vortex Methods for Separated Flows. *NASA TM 100068.*

Stewartson, K., [1974]. Multistructured Boundary Layers on Flat Plates and Related Bodies. *Adv. Appl. Mech.*, **14**, 146.

Strickland, J.H., [1993]. Modeling Wake Evolution Behind a Submarine: Two Dimensional Maneuvers. *Sandia Report SAND93-0040.*

Strickland, J.H., Kempka, S.N., and Wolfe, W.P., [1995]. Viscous Diffusion of Vorticity in Unsteady Wall Layers Using the Diffusion Velocity Concept. *Proceedings of the Forum on Vortex Methods for Engineering Applications, Albuquerque, NM, Feb. 22-24.*

Subramaniam, S., [1996]. *A New Mesh-Free Vortex Method*, Ph.D. thesis, Florida State.

Taneda, S., and Honji, H., [1971]. Unsteady Flow Past a Flat Plate Normal to the Direction of Motion. *J. Phys. Soc. Japan*, **30**, 262.

Tokumaru, P., [1991]. *Active Control of the Flow Past a Cylinder Executing Rotary Motions*, Ph.D. thesis, Caltech.

Tokumaru, P., and Dimotakis, P., [1991]. Rotary Oscillation Control of a Cylinder Wake. *J. Fluid Mech.*, **224**, 77.

Willmarth, W., Hawk, N., and Harvey, R., [1964]. Steady and Unsteady Motions and Wakes of Freely Falling Disks. *Phys. Fluids*, **7**, 197.

Winckelmans, G., [1989]. *Topics in Vortex Methods for the Computation of Three- and Two- Dimensional Incompressible Unsteady Flows*. Ph.D. thesis, Caltech.

Winckelmans, G., and Leonard, A., [1993]. Contributions to Vortex Particle Methods for the Computation of Three-Dimensional Incompressible Unsteady Flows. *J. Comput. Phys.* **109**, 247.

Zdravkovich, M., [1981]. Review and Classification of Various Aerodynamic and Hydrodynamic Means for Supressing Vortex Shedding. *J. Wind Eng. and Industr. Aero.*, 7, 145.